U-RQR/67-1

Copy No. 145

Quarterly Report

RESEARCH and DEVELOPMENT PROGRAMS

JANUARY—MARCH 1967

THE JOHNS HOPKINS UNIVERSITY ▪ APPLIED PHYSICS LABORATORY

U-RQR767-1

Quarterly Report,

RESEARCH and DEVELOPMENT PROGRAMS

JANUARY—MARCH 1967

THE JOHNS HOPKINS UNIVERSITY • APPLIED PHYSICS LABORATORY
8621 Georgia Avenue, Silver Spring, Maryland 20910

7

FOREWORD

The Applied Physics Laboratory issues this Quarterly Report series to provide a useful record of its activities for the defense establishment. This series of reports is organized in six volumes, by major Laboratory program and security classification, as follows:

Programs	Unclassified No.	Classified No.
Weapons Systems		
Surface Missile Systems		WQR/67-1A
Polaris Support		WQR/67-1B
Research and Development	U-RQR/67-1	C-RQR/67-1
Space Programs	U-SQR/67-1	C-SQR/67-1

This number system for the six basic volumes uses the following nomenclature. The designator for Quarterly Report, "QR," is preceded by a letter indicating the scope of the report (i.e., "W" for Weapon Systems, "R" for Research and Development, and "S" for Space Program). The scope designator is preceded by "C" or "U" to indicate "classified" or "unclassified," respectively, when both a classified and an unclassified volume are issued. Following the QR designator is the year indicator (e.g., "67") and then a number from 1 to 4 to designate the appropriate quarter of the calendar year. When a volume must be further subdivided to facilitate appropriate distribution, the quarter-designating number is followed by an arbitrary letter (A, B, C, ...) to distinguish between different subtitles.

The Quarterly Reports use the format originated for the APL/JHU Aeronautics Division Quarterly Review in which each topic is presented on a single sheet of paper and each is keyed to its proper program, technical instruction, Laboratory group, and supporting agency. Using the pages printed for the basic QRs, the Laboratory is able to prepare Division quarterlies and other special-purpose reports as required. Each such special-purpose report has its own scope indicator letter preceding the QR but uses a classification indicator only if it is divided into classified and unclassified volumes.

THE JOHNS HOPKINS UNIVERSITY • APPLIED PHYSICS LABORATORY

UNCLASSIFIED

WQR/67-1A   U-RQR/67-1
WQR/67-1B   C-SQR/67-1
C-RQR/67-1   U-SQR/67-1

TABLE OF CONTENTS

V. FUNDAMENTAL RESEARCH

X. DOD RESEARCH PROJECTS

Section III
EXPLORATORY DEVELOPMENT

Microelectronics

In thin-film technology, thin-film interconnect patterns have been developed for three hydrid satellite circuit applications. These circuits are the source sink driver, the gated driver, and the diode array. Alumina has proved to be a useful substrate for the deposition of chromium resistors (III/1).

In microelectronic packaging major effort has been directed toward perfection of hybrid assembly processes (III/2).

In semiconductor diffusion technology, activities have been directed toward developing a capability for producing monolithic and hybrid circuits (III/3).

Maser Research

Major effort was divided between continued preparation of maser materials and microwave bench measurements relevant to the zero-field traveling-wave maser (III/4).

Propagation Studies

In theoretical investigations of the radar cross section of the sea, it is important to have a realistic identification of the surface for all sea conditions. Stereo ocean profiles of height versus distance for rough sea conditions were obtained from Oceanics, Inc. The energy wave spectrum obtained for the high frequencies for the stereo profile is compared with a theoretical spectrum obtained from the Phillips asymptote in the frequency domain. First results are encouraging (III/5).

Applied Aerodynamics Research

At the University of Michigan two simulators have been built to facilitate experimental studies of the two-dimensional interaction of a jet with a supersonic free stream. Preliminary tests have been made in a jet-turning simulator that uses an inclined plate to take the place of the deflected free stream and that part of the separated flow upstream of a dividing streamline (III/6a). A study was conducted to determine the practicability of designing a volume-limited missile configuration that would have good maneuverability at high altitude and moderate supersonic Mach numbers. The pitch-yaw-roll coupling difficulty was avoided by using a planar-type configuration. A second objective was to contribute to a continuing study of those interference phenomena in supersonic flow that adversely affect missile performance, especially those phenomena involved in pitch-yaw-roll coupling (III/6b).

Airframe Structures

During hypersonic flight large thermal stresses are generated by aerodynamic heating in the radomes of interceptor missiles. Extensive numerical results were obtained from the computer program, devised to obtain solutions for the stresses and thermoelastic deformations in the radome (III/7).

Structural Elastic Studies

A computer program has been developed that applies estimation procedures and calculates upper and lower bounds to nonzero bending frequencies of missiles. For input data, the program requires the missile bending stiffness and mass per unit length, both of which are taken to be piecewise constant (III/8).

Thermal Studies

Since gas transpiration cooling offers a means of protecting critical areas on high-speed flight vehicles, theoretical methods of coupling external transpiration cooling calculations to flight body temperature calculations are being developed. Tests of flow and heat transfer in transpiring ducts are being conducted as adjuncts to the computer program development (III/9).

Tests of the creep strength of T-222 alloy (87.5% tantalum, 10% tungsten, 2.5% hafnium) were conducted at 2400° to 3000°F. Specimens were coated with tantalum disilicide for oxidation resistance. Results were compared with those obtained for molybdenum-0.5% titanium and one of the stronger columbium alloys (III/10).

Limitations of Current Radomes

In support of the radome limitations program, tests were run on three fused silica and four alumina specimens to determine the room-temperature modulus of elasticity and modulus of rupture. Measurements of the thermal expansion of these materials were made by General Electric, Baltimore (III/11a).

Use of sandwich-constructed ceramic shells is being investigated as part of the radome limitations study. Experimental results of thermal stress tests on an alumina sandwich cone were used to develop theoretical values of the internal temperature distribution and thermal stress (III/11b).

Thermal Protection Systems

The need for sharp leading edges to operate at high temperatures is one of the more critical problems in development of hypersonic vehicles. Environmental factors of aerodynamic heating are listed in order of importance from the point of view of material capabilities. A family of wedge models was tested in the arc heater in a sonic-orifice free jet, and the results are reported (III/12).

Boundary Layer Phenomena

The University of Texas is investigating, in the high-speed wind tunnel, several facets of separation phenomena and ways to combat the deterioration in aerodynamic performance resulting from such unwanted flow attachment. Initial tests were carried out on vane-type mixing devices to determine their drag (III/13).

Advanced Warhead Research

Focusing of the blast was achieved in a test of a 2-inch diameter spherical charge of Composition C-4, initiated at twelve points by lengths of Detacord cut to produce the proper delays (III/14b).

An effort is underway to develop and apply an algorithm that can be used to obtain approximate solutions to thermal explosion problems. The generalized thermal explosion criterion was used to find the critical half-widths of slab hot spots; a solution for critical slab hot-spot size has now been shown to be applicable throughout the range of practical interest. By making suitable approximations to this solution, an approximate

explicit equation for critical size is derived (III/14c).

In the experimental program to investigate the explosive projection of metal, effort was continued to develop a system of precise projection. Two tests were performed at the Naval Ordnance Laboratory, White Oak facility at Stump Neck, Maryland. High precision of projection was obtained. Confinement provided in the second test was sufficient to approximate a complete cylindrical warhead (III/14d).

Adaptive Computing

The Adaptive Stabilization Computer program is directed toward development of a computer for predicting ship motion. Ship-motion data from David Taylor Model Basin, according to a preliminary analysis made in this quarter, shows that the autocorrelation function of both the roll and the pitch motion can be represented by an exponential cosine. These data are currently being fitted to an exponential cosine autocorrelation function (III/20).

Advanced Radar Antenna

A 96-element phased-array antenna has been constructed and evaluated; it has demonstrated wideband beam steering from 4 to 12 kMc/s. Distortion of the radiation pattern at some frequencies, believed caused by impedance mismatch, was investigated. Assembled phase shifters were tested, using material with a lower magnetic saturation. The impedance of a simulated infinite array of triangularly spaced elements was measured for the boresight condition over the entire frequency band (III/21).

Theoretical Studies

A study has been made in order to determine the state of a randomly excited dynamical system from noisy measurements having finite duration. This study has resulted in an optimal filter being derived by an entirely different method (III/23a). The steepest-ascent method is being applied to trajectory optimization problems. It is desirable to optimize the fuel-flow rate so that, using a fixed amount of fuel, a missile will attain a given altitude, either in minimum time or with maximum velocity (III/23b).

Research on Supersonic Combustion

The objective of this research is to determine some of the design criteria and the expected performance of the combustor and nozzle for hypersonic ramjets with supersonic combustion of hydrogen in the flight Mach number range from 5 to at least 10. The work includes studies of fuel jet penetration, mixing, ignition, and combustion, using various two-dimensional and axisymmetric test models, and special analyses related to combustor design.

Analytical techniques are being developed to determine the expected performance of a supersonic combustion ramjet and to assist in the general understanding of the supersonic process. Both a one-stream and a two-stream combustion-shock model have been developed in studies on using the combustion process to assist in engine compression. Both methods are shown to partially relieve the geometric constraints of a fixed-geometry engine required to operate at different flight Mach numbers (III/24b).

A generalized study of free turbulent mixing is under way to determine a suitable model for the eddy viscosity and to develop accurate approximate methods of solution for the differential equations of motion so that simple, reliable predictions of mixing processes in combustors can be obtained. This approach should facilitate analyses for determining the required length and optimum shape of the combustor. A new analytical treatment of free mixing problems is proposed and developed. This analysis does not assume similarity of flow. Prediction is compared with some experimental data for two options in the theory. Compared to classical similarity theory, the new approach is more accurate (III/24c).

Combustor designs using downstream fuel injection adjacent to the combustor wall are of interest because the momentum of the fuel will contribute to net engine thrust if mixing and combustion can be accomplished. In addition, a fuel layer next to the wall would alleviate cooling requirements. Experimental and theoretical studies of the two-dimensional turbulent mixing process are under way to deduce scaling laws pertaining to mixing, heat transfer to the wall, and skin friction. An analytical model, based on the work of Clauser, has been devised. Flow is represented by two layers; an outer wake-like layer is matched in velocity, normal velocity gradient, and shear stress to a "law-of-the-wall" inner layer. A technique has been devised for stream-wise integration of the boundary layer equations starting with arbitrary, nonuniform, initial velocity distributions (III/24d).

RESEARCH AND EXPLORATORY DEVELOPMENT III/1
Thin-Film Microelectronics A11CME
Support: ORD-0625
C. S. Morris
January-March 1967

THIN-FILM TECHNOLOGY DEVELOPMENT

Thin film technology provides a convenient method for producing resistor, capacitor, and interconnection patterns in a hybrid package. Developing these techniques is essential, since thin-film hybrid circuits are finding application in satellite and missile systems.

SUMMARY

Thin-film interconnect patterns have been developed for three hybrid satellite circuit applications. These circuits are the source sink driver, the gated driver, and the diode array. These circuits include resistors, diodes, and transistors. The resistors are fabricated by thin-film techniques; the transistors and diodes are discrete components.

Alumina has proved to be a very useful substrate for the deposition of chromium resistors. Resistance values that can be obtained from evaporated chrome vary from 1 to 900 ohms/square. In particular, some 27,000 ohm resistors have been fabricated to an accuracy of ±2.5%.

Work is continuing on the development of the anodized aluminum thin-film capacitors.

FUTURE PLANS

Further study is anticipated in the use of alumina as a substrate in lieu of glass because of its higher thermal conductivity.

The fabrication of thin-film passive circuits for use in micro-power logic circuitry will be investigated.

In the area of large-scale integration, thick-film will be investigated for interconnecting patterns over thin-film resistors passivated by silicon oxide.

DISCUSSION

Thin-film resistors used in the source sink driver have been produced within a tolerance of ±10%. These resistors are 500 and 1000 ohms in value. The resistors in the gated driver are 5000 ohms; their value will also be within the ±10% tolerance. The diode array is a series of eight common anode and eight common cathode diodes contained in a 1/4- by 1/4-inch flatpack. These diodes are arranged in four quads on a glass substrate using thin-film interconnections.

Alumina is superior to glass as a substrate in some applications. Particularly, the heat dissipation is about seven times as great and the resistance values obtainable, for a given evaporation time, are about three times as great. Unglazed alumina is a very rough surface, about 8 microns, and it is quite hard.

Previous attempts to produce anodized aluminum capacitors with a practical breakdown voltage were hampered somewhat by problems in the photoresist. To alleviate this problem while the photoresist is being developed, mechanical masks are being used in forming the aluminum oxide and the vacuum-deposited aluminum counter electrodes. One difficulty in the anodization process is that the oxide tends to be porous. With a porous oxide, the dielectric constant will be small compared to a nonporous oxide. The maximum thickness of a nonporous oxide is about 300 Å. This thickness necessarily determines the breakdown voltage, but high-capacity values can be obtained. An anodization process is being developed that will produce a very dense dielectric and consequently capacity values of approximately 2 $\mu f/cm^2$.

MICROELECTRONIC PACKAGING

The devices fabricated in the thin-film and semi-conductor laboratories must be packaged in a form suitable for use in missiles and space vehicles. The processes and equipment necessary to carry out this function are complex. It is essential that the packaging processes not degrade the device characteristics.

SUMMARY

The major effort during this quarter has been directed toward perfection of hybrid assembly processes. These processes, while appearing simple, require extensive training of personnel. Processes, as developed, are being documented in a handbook so that a quick reaction capability will be available.

FUTURE PLANS

Improved in-process testing appears to be the key to high yields. A better understanding of the effect each step of the assembly process has on the device characteristics makes it possible to rearrange test sequences and the processes themselves to improve device yields.

Plans are being formulated to explore a marriage of thick-film and thin-film techniques to achieve a hybrid that incorporates the best features of each.

The trend in the microelectronic field is toward large-scale integration, defined as the assembly of many integrated circuits on a common substrate. The large-scale integration problem will be studied with an eye to how hybrid techniques can be exploited to this end.

DISCUSSION

The hybrid circuit for use in one of the Laboratory's space vehicles, which was noted in the last Quarterly Report, is progressing nicely. All processes, including complete flight acceptance tests, have been established. A quantity sufficient to assemble one satellite has been fabricated, and tests are currently in progress. The yields achieved at various stages of the processing show clearly that carefully selected tests performed at the critical points in the assembly would save much man-power and material. In particular, the semiconductor characteristics are influenced in unexpected ways by the bonding and cleaning processes; by establishing this pattern with sample lots and then initiating monitoring tests, it is possible to improve the efficiency of the operation significantly.

The quick-reaction capability of the laboratory was recently proved by a request to design and build a hybrid circuit slightly more complex than the one noted above. Two satisfactory units were delivered one week after the request.

A longer-term study to develop a packaging scheme for a radar subsystem is under way for the APL Radar Group. During the next two quarters we expect that a hybrid packaging technique will be evolved that will satisfy this need and, furthermore, represent an advance in the large-scale integration capability at the Laboratory.

RESEARCH AND EXPLORATORY DEVELOPMENT   III/3
Semiconductor Microelectronics A12CME
Support: AIR-5202, Task X/NOw 62-0604-c
C. S. Morris
January–March 1967

SEMICONDUCTOR DIFFUSION TECHNOLOGY

The fabrication of semiconductor microelectronic circuits consists of diffusing impurities into a semiconductor wafer. Typically, four separate diffusions occur, and for these precise control must be maintained over diffusion depths, impurity concentrations, and surface geometry. These controls are being established so that microelectronic circuits may be fabricated for missile and space applications.

SUMMARY AND CONCLUSIONS

Activities during this period have been directed toward developing a capability for producing specific monolithic and hybrid circuits. This capability is dependent upon solving a number of processing problems as follows:

1. Oxide and photoresist defects, called pinholes, may cause device failure. A study indicates that these failures may be calculated before device fabrication from the circuit layout geometry.
2. Metal-oxide-silicon (MOS) capacitors have been produced. These capacitors have a value of approximately 50 pf and are 17 mils square in size.
3. Newer photoresists are being studied, and attempts are being made to develop an in-house capability to make a photoresist with characteristics more compatible with our needs. Photoresist characteristics are extremely important in fabricating small devices where the required mask line widths may be as small as 0.1 mil.
4. A standard test mask has been designed that incorporates transistor and resistor patterns. This mask may be used to develop a wide range of diffusion capabilities, and it will provide a convenient way to periodically evaluate the process.

FUTURE PLANS

A transistor will be developed for use in a low power ($< 100 \mu w$) flip-flop and associated gating circuitry.

Research in photolithographic techniques will continue.

BACKGROUND

Present day technologies indicate that both semiconductor and thin-film techniques must be used in a hybrid approach to producing integrated circuits. Semiconductor technology is being used to fabricate active devices, but these devices must cover a broad spectrum of electrical characteristics. The present technology is being used to make useful devices, and changes will be made to fulfill future needs.

DISCUSSION

An essential part of the diffusion technology concerns the silicon oxide that is grown on the surface of the wafer. Holes are etched in the oxide to allow diffusion to take place at these sites; the remainder of the oxide serves as a mask to prevent diffusion. Undesirable holes or cracks (pinholes) can be caused by mechanical imperfections in the oxide. Some pinholes are caused by thermal stresses set up when the wafer is withdrawn from the oxidation furnace. A slow withdrawal (20 minutes) results in reduced stress, and the oxide integrity is enhanced. Pinholes allow spurious diffusions, and depending on their location, these diffusions reduce device yield. A formula has been devised that will allow the calculation of the approximate decrease in circuit yield because of oxide defects. The formula is based on experimentally determined defect density and the circuit layout geometry; therefore, the yield may be calculated before device fabrication (Ref. 1).

The fabrication of capacitors of reasonable value, geometrical size, and voltage breakdown is one of the stumbling blocks in integrated circuit technology. One development in this area is the MOS capacitor. A number of capacitors of approximately 50 pf with a breakdown voltage ranging from 120 to 140 volts were fabricated. A common electrode of aluminum was evaporated on one side of a silicon wafer of 1 ohm-cm resistivity. Silicon oxide about 1800 Å thick was grown on the opposite side of the wafer to form the dielectric. Aluminum pads 17 mils square, on 20-mil centers, were then deposited on the oxide. The 3-mil separation between these pads provided plenty of room for scribing and dicing the wafer. The resulting capacitors were then approximately the size of a transistor die. Capacitors up to 100 pf can be fabricated using this technique.

In the area of photoresist research, centrifuging and filtering techniques available produce photoresist sufficiently pure for reproducing ma___   widths in the neighborhood of approximately 1/10 mil. The difficulty is that commercially procured photoresist has a limited shelf life because the sensitizing agent permits polymerization to occur at a slow rate even during storage. One solution that is being pursued is the development of a photoresist and a sensitizer that are mixed just prior to use. If this development succeeds, centrifuging and filtering processing can be greatly reduced.

To maintain control over semiconductor processing, some form of test mask is desirable. A mask recently designed includes three transistors of different geometrical size and a number of resistor patterns. The resistor patterns range from   1/10 to 2 mils in width. This test mask will be used to perfect and evaluate the semiconductor process and will provide us with the means for developing a wide range of active and passive semiconductor devices.

REFERENCE

1. R. F. Plachy, "Microelectronic Device Loss in Processing Due to Faulty Silicon Dioxide Mask," APL/JHU CME-2-67004, 6 April 1967

RESEARCH AND EXPLORATORY DEVELOPMENT III/4
Maser Research A13CLO
Support: ORD-034
A. W. Nagy
January-March 1967

MASER RESEARCH PROGRAM

Advanced developments in maser techniques have applications in general communications systems, radar and radio astronomy, and in advanced missile systems where very low-noise microwave amplification contributes to improvements in detection sensitivity and system performance. Although initial experimental efforts have been made and are continuing at X-band, an objective of this program is to extend any promising results in both zero field and magnetic field techniques to masers operating in the millimeter wavelength ranges. Important applications to missile radiometry would be possible in this part of the spectrum.

SUMMARY AND CONCLUSIONS

The major effort during the past quarter was divided between continued preparation of maser materials and microwave bench measurements relevant to the zero-field traveling wave (TW) maser. Two fluxed-melt runs were completed with 0.08% iron concentration containing additionally 0.25% and 0.50% lanthanum oxide for modifying crystal growth habit, as discussed in the previous Quarterly Report. The first of these runs, programmed to a cooling rate of about 2°C/hr from the maximum soaking temperature of 1300° down to below 900°C, was unsuccessful owing to an accidental opening of the crucibles, probably early in the run. The mixtures in the crucibles, for the first time in this series of runs, had been wet ball-milled with the expectation that a more homogeneous starting mixture would result and, in turn, a possibly improved crystal quality. Although the material was thoroughly baked following the milling, sufficient water was probably retained to force the lids off. The second of the fluxed runs with the charges dry mixed was successful. This crystal run confirmed the deleterious effect of too high a percentage of lanthanum oxide for the slower cooling rates. Crystal quality, moreover, appeared to be no better than for the usual 4°C/hr rates, but there were fewer flux inclusions between the crystal planes.

Iron doped alumina rods of 0.06 and 0.1% iron concentration have been prepared and are ready for testing. Similar rods with 0.04 and 0.05% iron are ready for the 1800°C treatment. Samples of these four concentrations will be used to determine the optimum iron concentration for the TW maser structure. The concentration in the present slow wave structure is 0.03%.

Initial dielectric measurements on thin discs of the TW 0.03% rod, using a cavity resonance technique, establishes a dielectric constant for this material of around 9.2. This would be an acceptable figure even for the boule sapphires. For the rods it indicates that the 1800°C heat treatment is producing a density probably as high as can be expected via high-temperature soaking.

The first helium run on the zero-field TW maser was accomplished following extended bench adjustments in order to secure reasonably good input and output impedance matches to the helix. The TW maser head in its present form does not allow adjustments to the circuit, which are generally required when the operation is in liquid helium. Strong oscillations were observed in zero field following the application of pump power at 31.325 Gc/s. The preferred frequency of oscillation was around 12.02 Gc/s, a frequency slightly lower than that usually observed with the powder cavities. This was a first experiment on an essentially non-adjustable system, but there is now a reasonable asurance that a wave is propagating through the slow-wave helical structure. Some constructional details of the system will be given in the next Quarterly Progress Report.

FUTURE PLANS

The optimal iron concentration for the alumina TW rods should be decided during the next quarter. A new slow-wave helix structure (now that most of the mechanical problems have been solved) may then be fabricated for the final TW maser design. An attempt will be made both to incorporate some reverse attenuation into the slow-wave structure and to provide some external control on the circuit adjustments while in liquid helium.

BACKGROUND AND DISCUSSION

The first phase of the maser program was initiated with the following objectives: (a) to optimize the gain-bandwidth product of a reflection cavity ruby maser in single- and multiple-cavity configurations, and (b) to examine the suitability of iron sapphire as a zero-field maser material with possible adaptation of the multiple cavity broadband techniques developed in (a). As indicated in previous Quarterly Reports and the published Refs. 1, 2, and 3, this phase of the maser program has to all intents been accomplished. The present phase of the program is concerned mainly with preparation at APL of a suitably doped Fe^{3+} corundum powder that could be used as a paramagnetic operating either in a cavity or TW maser structure. In the zero-field mode, a powder paramagnetic would allow novel geometries in slow-wave structures and would have some advantages over magnetic field maser operation (Ref. 4). The results of a large number of experimental runs indicate the feasibility of a zero-field maser using an iron-doped sapphire powder. Thus far iron concentrations of the calcined powders in the range 0.01% to 0.25% appear to maser best. Pending improvements in the technique for fabricating an optimum-concentration pressed-powder rod for use as a TW zero-field maser, a crystal growing facility for growing iron-doped sapphire crystals via a molten flux method was set up. This process

should prove desirable subsequently for growing maser crystals suitable to the millimeter wavelength range.

REFERENCES

1. A. W. Nagy and G. E. Friedman, "Zero-Field Maser," APL Technical Digest, July-August 1964, pp. 2-12.

2. A. W. Nagy and G. E. Friedman, "Reflection Cavity Maser with Large Gain Bandwidth," Proc. IRE, Vol. 60, December 1962, pp. 2504-2505.

3. G. E. Friedman and A. W. Nagy, "Iron Sapphire Maser with No Magnetic Field," Proc. IEEE, Vol. 51, February 1963, pp. 361-362.

4. A. W. Nagy and G. E. Friedman, "A No-Field Power Maser," Proc. IEEE, Vol. 51, July 1963, p. 1037.

RESEARCH AND EXPLORATORY DEVELOPMENT   III/5
Propagation Studies A14BPD
Support: AIR-310
G. R. Valenzuela and E. B. Dobson
January-March 1967

RADAR SCATTERING FROM THE SEA

Theoretical and experimental study programs are being carried out by APL on the radar cross section of the sea. The purpose of this report is to present the results of this research to date.

SUMMARY AND CONCLUSIONS

In theoretical investigations of the radar cross section of the sea, it is important to have a realistic identification of the surface for all sea conditions.

At the Laboratory we have used simple point measurement of height versus time and have also performed stereo measurements of the sea. Here we present first results on stereo ocean profiles of height versus distance for rough sea conditions. The energy wave spectrum obtained for the high frequencies for the stereo profile is compared with a theoretical spectrum obtained from the Phillips asymptote in the frequency domain. This first result is quite encouraging; now we await further processing of stereo ocean profiles in order to give more conclusive results on the stereo measurements.

FUTURE PLANS

The knowledge of the quantities representing the sea for all sea conditions is still incomplete. Therefore, we must increase our knowledge of the sea surface and then determine which theories are more applicable to calculate radar cross sections.

DISCUSSION

In theoretical investigations of "sea clutter" two main areas of study can be clearly distinguished: the identification of the sea under different conditions, and the electromagnetic boundary value problem of the air-sea interface.

In the first area we have been making measurements of the sea surface (Refs. 1 and 2). The stereo waves measurement program that was started under contract from the Office of Naval Research to Oceanics, Inc., with supervision by APL, is bearing its first fruits. We have ocean-profiles from Oceanics, Inc., and are in the process of analyzing them.

The spectrum for the high frequencies was obtained for one profile of 596 height points spaced 0.315 inch apart for rough sea conditions. Using a Fourier series fit, we removed up to the fifth harmonic in the length of the profile. The modified profile, without the low frequencies, was used to obtain the high-frequency spectrum. Figure 1 shows the spectrum obtained. In the same figure we have plotted for comparison a theoretical spectrum obtained from the Phillips asymptote (Ref. 3) for the

STEREO PROFILE
PHOTO NO. 22 (DEC. 9, 1964)
RMS OF SEA: 1.077–1.263 FEET
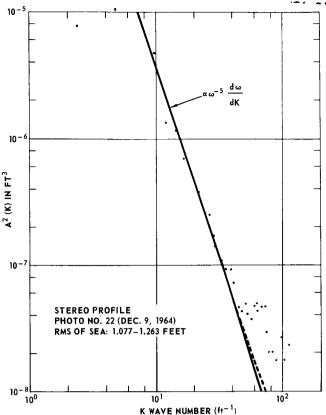
Fig. 1   Wave Number Spectrum of Stereo Profile. (596 Points at 0.315-Inch Spacing.) (90689)

STEREO PROFILE
PHOTO NO. 22 (DEC. 9, 1964)
RMS OF SEA: 1.077–1.263 FEET
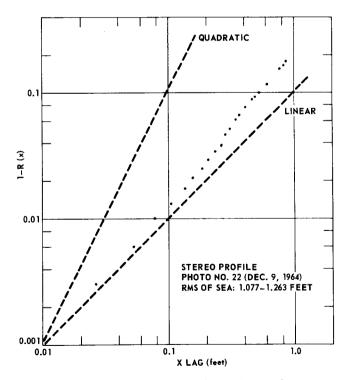
Fig. 2   Behavior of the Autocorrelation Function from Stereo-Photo versus Lag Distance. (90690)

THE JOHNS HOPKINS UNIVERSITY • APPLIED PHYSICS LABORATORY

frequency spectrum of the form

$$A^2(\omega) = \alpha\,\omega^{-5}\,,\qquad(1)$$

where $\alpha = 7 \times 10^3\ cm^2 sec^{-4}$, and ω is the radian frequency.

The wavenumber spectrum $A^2(K)$ was obtained from the expression

$$A^2(K) = A^2(\omega)\,\frac{d\omega}{dK}\,,\qquad(2)$$

and we also used the relationship between radian frequency and wavenumber K

$$\omega^2 = gK + SK^3\,,$$

where g is the acceleration of gravity and S is the surface-tension-to-water-density ratio ($\sim$74 $cm^3 sec^{-2}$). The spectrum obtained from the stereo profile agrees closely with the theoretical spectrum for wavenumbers up to 40 $(feet)^{-1}$. As the high-frequency spectra for other profiles are obtained, we might have more conclusive results on the capabilities of the stereo method.

In calculating radar cross sections of the sea, the surface is characterized in a statistical manner; the height of the surface is taken to be a random process with a gaussian probability density, with zero mean value and variance σ^2. In the slightly rough case (irregularities of small height compared with the wavelength λ of the electromagnetic radiation), the energy spectrum of the surface determines the shape of the radar cross section as a function of angle of incidence (Ref. 4). For a rough surface in which the radius of curvature of the irregularities is large compared to the wavelength of radiation, the Kirchhoff method, with the tangent plane approximation for the field on the surface, is applicable to calculate cross sections.

In general, however, in the sea we have a mixture of all kinds of irregularities, thus neither method is always applicable. When the Kirchhoff method is applied to a very rough surface (the height of the irregularities is large compared to the wavelength of radiation), the behavior of the autocorrelation function $R(x)$ near the origin determines the functional dependence of the normalized cross sections with angle of incidence (Ref. 5). For example, if we use a gaussian autocorrelation function for the sea surface

$$R(x) = \exp(-x^2/L^2),$$

the normalized cross-section σ_o is of the form

$$\sigma_o(\theta) \propto \cos^{-4}\theta\,\exp\left\{-\left(Ltan\theta/2\sigma\right)^2\right\},\qquad(3)$$

which has the proper behavior for small angles of in-

cidence θ, but decreases too fast for larger angles compared with measured cross sections.

On the other hand, if we use an exponential autocorrelation function

$$R(x) = \exp\left\{-|x|/L\right\},$$

the normalized cross-section comes out to be

$$\sigma_o(\theta) \propto \left[\cos^4\theta + \left(\frac{\lambda L}{4\pi\sigma^2}\right)^2 \sin^2\theta\right]^{-3/2}.\qquad(4)$$

This last equation, when plotted, has the characteristic shape of measured cross sections, although the values of the parameters L and σ may not agree with those measured for the sea. Recently Semyonov (Ref. 6) obtained the characteristic shape of σ_o as a function of θ in an approximate manner, using the Kirchhoff method with a gaussian correlation function plus adding contributions from little ripples riding the big waves.

Thus, it is important to know the correct behavior of the autocorrelation function for the surface near the origin in order to separate the effects of autocorrelation function shape and small ripple contributions in calculating σ_o.

In Fig. 2 we have plotted the behavior of the autocorrelation function from the stereo profile for which the spectrum in Fig. 1 was obtained. The autocorrelation of this profile seems to behave closer to exponential, although in the profile we have only a small portion of the surface.

REFERENCES

1. M. T. Miyasaki, "Spar Buoy Wave Gage," APL/ JHU BPD65U-4, 31 March 1965.
2. I. Katz, "Ocean Wave Measurements," APL Technical Digest, September-October 1964, pp. 2-6.
3. O. M. Phillips, "The Equilibrium Range in the Spectrum of Wind-Generated Waves," J. Fluid Mech., Vol. 4, 1958, pp. 426-434.
4. W. H. Peake, "Theory of Radar Return From Terrain," IRE National Convention Record (Part I), 1959, pp. 27-41.
5. P. Beckmann, "Scattering by Composite Rough Surfaces," Proc. of the IEEE, Vol. 53, No. 8, 1965, pp. 1012-1015.
6. B. I. Semyonov, "Approximate Computation of Scattering of Electromagnetic Waves by Rough Surface Contours," (translation), Radio Eng. and Electronic Phys., Vol. 11, No. 8, 1966, pp. 1179-1187.

UNCLASSIFIED

SIMULATION EXPERIMENTS FOR JET INTERACTION

The flow field produced by a jet issuing from a flat plate aligned with a supersonic stream is complicated, even in the two-dimensional case. In order to reduce the degree of complexity, simulation experiments have been devised in which the flow on one side of a dividing streamline is replaced by a solid surface. By this means it is planned to study independently the flow phenomena in the main stream and in the jet, in hopes of obtaining new information that will aid in understanding the complete interaction.

SUMMARY AND CONCLUSIONS

Two simulators have been built to facilitate experimental studies of the two-dimensional interaction of a jet with a supersonic free stream (see Fig. 1). A semi-cylindrical-step simulator (Fig. 2) will be used for experiments on the flow processes in the external stream, with the jet and a portion of the separated flow downstream of a dividing streamline simulated by the semi-cylindrical step.

Preliminary tests have been made in a jet-turning simulator. This simulator uses an inclined plate to take the place of the deflected free stream and that part of the separated flow upstream of a dividing stream-line. A schlieren photograph taken in this simulator (Fig. 3) shows qualitative agreement with typical flow patterns of complete interaction (Ref. 1). Pressure measurements along the inclined plate (Fig. 4) show a sharp pressure peak that is taken to be a stagnation point, corresponding to the effective step height of the jet. Values of this effective step height (Fig. 5) are in qualitative agreement with the circular-arc jet theory of Ref. 2, although it is indicated that the fully-expanded jet would probably have a somewhat greater step height, and therefore greater interaction force, than does the sonic, highly under-expanded, jet that was tested.

FUTURE PLANS

Extensive testing of both simulators is planned. The semi-cylindrical-step simulator will be tested in the 8- by 13-inch supersonic wind tunnel at Mach 4.0. Further tests of the jet-turning simulator will be made with the simulator connected directly to a vacuum line.
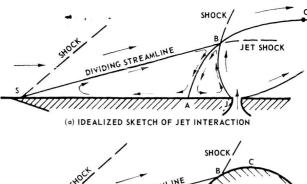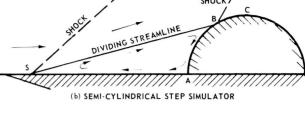
BACKGROUND AND DISCUSSION

An idealized sketch of two-dimensional jet inter-action is shown in Fig. 1a. The separated flow region is visualized as consisting of two counterrotating cells of fluid. The clockwise-turning cell is driven by mixing with the main stream, while mixing with the jet produces a cell with counter-clockwise rotation.

In a semi-cylindrical-step simulator the dividing streamline (ABC in Fig. 1) between the jet and the main stream and their respective vortical cells is represented

THE JOHNS HOPKINS UNIVERSITY ■ APPLIED PHYSICS LABORATORY

UNCLASSIFIED

(a) IDEALIZED SKETCH OF JET INTERACTION

(b) SEMI-CYLINDRICAL STEP SIMULATOR
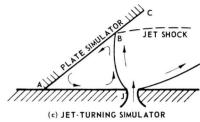
(c) JET-TURNING SIMULATOR

Fig. 1 Structure of Flow Caused by Two-Dimensional Jet Interaction, and Suggested Simulators. (90693)
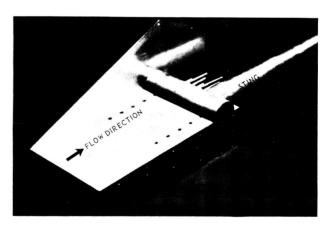
Fig. 2 Semi-Cylindrical-Step Simulator with One End Plate Removed (Brace across Top of Two End Plates also Not Shown). (90694)

by the surface ABC of the semi-cylinder. A photograph of the semi-cylindrical-step simulator with one end plate removed is shown in Fig. 2. Pressure holes on the plate and semi-cylinder are intended to aid in locating the points of separation and reattachment. Several sets of mounting holes on the plate permit the semi-cylinder to be mounted at various distances from the leading edge. This simulator has not been tested.

To simulate the other half of the interaction flow, a jet-turning simulator, as shown in Fig. 1c, has been built. In this simulator, the dividing streamline ABC is again represented by a solid surface; this time the inclined plate (ABC in Fig. 1c) represents the dividing streamline, and the flow on the jet side is studied.

The jet-turning simulator, as built, consists chiefly of a horizontal bottom plate containing the sonic jet slot, and an inclined top plate on which the jet impinges. Both plates are 1-inch wide and are clamped between parallel glass side plates, to form a two-dimensional channel.

Fig. 3 Spark Schlieren Photograph of Flow in Jet-Turning Simulator, $\theta = 24.3°$, L = 3.96 inches, w = 0.029 inch, $p_{o_j}/p_2 = 41$, $p_b/p_2 = 0.1$. (90695)
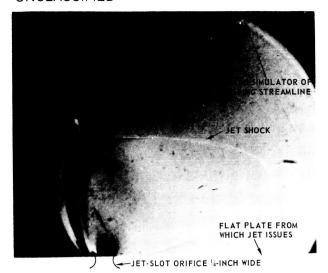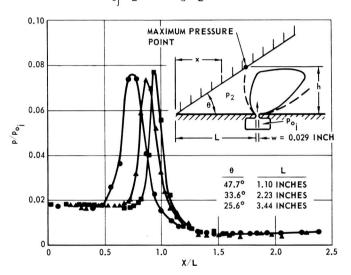

Fig. 5 Equivalent Spoiler Height Given by Jet-Turning Simulator and by Circular-Arc Jet Theory, $p_{o_j}/p_2 = 60$, $p_b/p_2 = 0.3$. (90697)

Fig. 4 Pressure Distributions along Inclined Plate of Jet Turning Simulator. (90696)

θ	L
47.7°	1.10 INCHES
33.6°	2.23 INCHES
25.6°	3.44 INCHES

A photograph of the flow in the jet-turning simulator is shown in Fig. 3. This is a spark schlieren, taken in the case when the jet stagnation pressure was 64.2 psia. Note that disturbances from the jet reach the inclined plate, where they appear to be centered somewhat upstream of the jet exit. The explicit flow conditions are recorded in the figure captions. The definitions of pressures and angles may be most easily obtained by referring to Fig. 4.

Pressure measurements on the inclined plate are presented in Fig. 4 for three different plate angles. A distinctive feature of these pressure distributions is the sharp peak that occurs somewhat upstream of the jet exit. Similar sharp peaks were noted by Sterrett and Barber (Ref. 1). Their flow configuration was similar to that of the present tests, with the important difference that the cavity upstream of the jet was not closed, so that the jet was not forced to turn.

The sharp pressure peaks of Fig. 4 are assumed to correspond to the common stagnation point between the jet and the main stream, labeled B in Fig. 1. The distance from the flat plate to the stagnation point B is
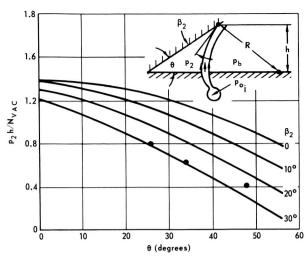
the effective step height h. Values of h corresponding to the peaks in Fig. 4 are plotted in Fig. 5 in terms of the nondimensional parameter $p_2 h/N_{vac}$, in which N_{vac} is the normal force of the jet in a vacuum, per unit span. This parameter comes from the idealized circular-arc jet theory of Ref. 2, results of which are shown as the solid lines in Fig. 5, and is closely related to the normal force amplification factor K, which is given by the circular-arc jet theory (which assumes no shocks are present in the jet) as

$$K - 1 \overset{\sim}{=} p_2 h/(N_{vac} \tan \alpha),$$

where α is the boundary layer separation angle (BSA in Fig. 1).

Comparison of the theoretical and experimental results of Fig. 5 shows that the actual (having internal shocks) jet values from the jet-turning simulator correspond to circular-arc jets having β_2 values between 25° and 30°. Since β_2 would be expected to be less than 25°, this plot indicates better amplification of the jet force for the circular-arc jet than for the actual jet, which issues from a simply convergent (sonic) mouth.

Similar results for the jet-turning simulator presented in an earlier progress report (Ref. 3) were found to be in error because of the use of gage pressure values of p_{o_j} in place of absolute pressures. Also, the nominal slot width was used instead of the effective value determined from mass flow measurements.

REFERENCES

1. J. R. Sterrett and J. B. Barber, A Theoretical and Experimental Investigation of Secondary Jets in a Mach 6 Free Stream with Emphasis on the Structure of the Jet and Separation ahead of the Jet, NASA TMX 57139, May 1966

2. J. L. Amick, Circular-Arc Jet Flaps at Supersonic Speeds - Two-Dimensional Theory, The University of Michigan, Department of Aerospace Engineering Report, APL/JHU CR-24, July 1966.

3. R. H. Cramer, "Simulation Experiments for Side Jet Interference," Section III/2, Research and Development Programs Quarterly Report, July-September 1966, APL/JHU U-RQR/66-3 (also in AQR/66-3).

N67-33368

RESEARCH AND EXPLORATORY DEVELOPMENT III/6b
Applied Aerodynamics Research A31BBA
Support: ORD-035
H. H. Hart
January-March 1967

PLANAR CONFIGURATION STUDY

This empirical study was intended to determine the practicability of designing a volume-limited missile configuration that would have good maneuverability at high altitudes and moderate supersonic Mach numbers. Attainment of this objective meant avoiding the pitch-yaw-roll coupling difficulty, a requirement that was met by using a planar-type configuration. A second objective, which was also realized, was to contribute to a continuing study of those interference phenomena in supersonic flow that adversely affect missile performance, especially those phenomena involved in pitch-yaw-roll coupling.

SUMMARY

Use of a tail-controlled planar configuration requires that the control system operate by the bank-to-maneuver or so-called "twist and steer" method. Such a configuration must have near neutral stability in pitch and roll, combined with high directional stability at all angles of attack.

The study was carried on by a repeated sequence of wind-tunnel testing, evaluation, and semi-empirical correlation of test results. The three types of configuration for which studies were made are, in chronological order: dorsal-finned configurations (Fig. 1), delta-winged configurations (Fig. 2), and dart-winged configurations (Fig. 3). Optimization studies, culminating in the design of the dart-winged configuration, were made at Mach 2.5. Additional wind-tunnel data were collected at Mach 3.5 in order to show that results at the lower Mach numbers remained valid over this Mach number range. The aerodynamic stability and control characteristics of all planar configurations examined in this study are documented and compared in Ref. 1.

The aerodynamic interference phenomena that influence the behavior of these configurations are exhibited and studied in Ref. 2. Indeed it is seen that the lateral and directional characteristics of these configurations are dominated both qualitatively and quantitatively by interference effects.

FUTURE PLANS

Work on this study will be completed with publication of the final reports, Refs. 1 and 2.

BACKGROUND

Supersonic missiles, especially those having cruciform configurations, when attempting to operate at high angles of attack, generally encounter the difficulty known as pitch-yaw-roll coupling. A missile encountering this condition will go out of control unless there is adequate compensation built into the autopilot. This

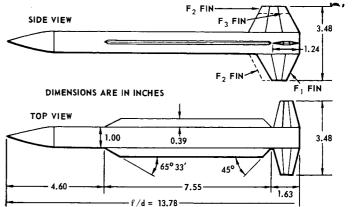THE JOHNS HOPKINS UNIVERSITY • APPLIED PHYSICS LABORATORY
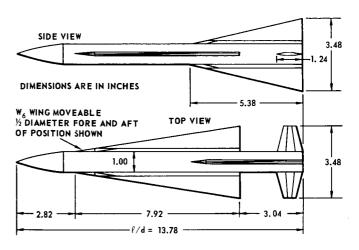
Fig. 1   Typical Dorsal-Finned Configuration. (90622)

Fig. 2   Typical Delta-Winged Configuration. (90623)

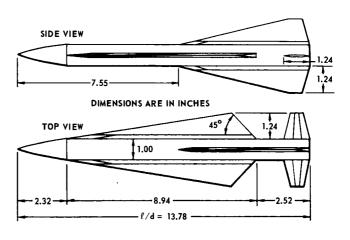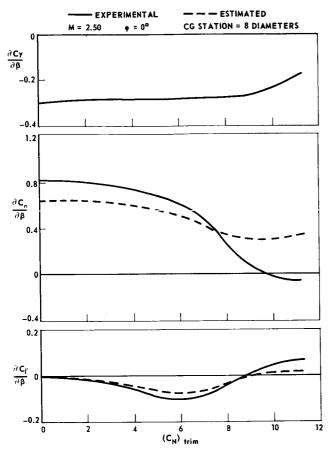Fig. 3   Dart-Winged Configuration. (90624)

——— EXPERIMENTAL   — — — ESTIMATED

M = 2.50 $\varphi = 0°$ CG STATION = 8 DIAMETERS

Fig. 4   Lateral and Directional Stability of Delta-Winged
Configuration. (90625)

——— EXPERIMENTAL   — — — ESTIMATED

M = 2.50 $\varphi = 0°$ CG STATION = 8 DIAMETERS

Fig. 5   Lateral and Directional Stability of Dart-Winged
Configuration. (90626)

effectively limits missile angle of attack, hence man-
euverability at high altitudes. A continuing study at
APL has been directed toward further understanding
of this phenomenon and determining means of avoiding
it. The planar configuration study was a part of this
overall program.

DISCUSSION

The need for good directional stability came from
the desire to avoid the use of the vertical control sur-
faces that are a major factor in producing pitch-yaw-
roll control coupling. All control was to be accom-
plished by the combined aileron and elevator effect of
the horizontal control surfaces.

Some difficulty in attaining directional stability
was anticipated because of previous difficulties with
vertical control surfaces arising from the large dif-
ferences in dynamic pressure between the windward
and leeward sides of the body when at high angles of
attack. It was thought that the large vertical fin to
leeward would lose its effectiveness, but that if the fins
were sufficiently large, the windward fin would compen-

sate for this. As it turned out, the vortices shed from
the dorsal fins of the first configurations tested (Fig. 1)
created a reverse flow over the leeside fin, which made
the directional stability much worse than anticipated.

For the second attempt the delta-wing configuration
was chosen, with the intention that large delta wings
would cause the vortices to be carried well outboard so
as to pass clear of the vertical fin. This expectation
was realized, but it was found that there was still a
loss of directional stability, i.e., of $\partial C_n/\partial\beta$, at large

values of angle of attack or normal force coefficient,
$(C_N)_{trim}$, as shown in Fig. 4.

The new difficulty was found to result from an in-
terference effect between the wing trailing edge and the
leeside fin. An empirical study of the data showed the
possibility of alleviating this condition by changing the
shapes of the trailing edges to give the dart-wing con-
figuration shown in Fig. 3. Tests of this configuration
indicated good agreement between experimental and pre-
dicted results, as shown in Fig. 5. Since the design
objective had been attained, testing was discontinued.
The remainder of the study was devoted to the corre-
lation and presentation of the results obtained (see
Refs. 1 and 2).

REFERENCES

1. H. H. Hart, Supersonic Stability and Control Char-
    acteristics of Low-Aspect-Ratio Planar Configura-
    tions Designed for Large Maneuvers (to be pub-
    lished).
2. H. H. Hart, Supersonic Interference Effects in Low-
    Aspect-Ratio Planar Configurations at Large Angles
    of Attack (to be published).

UNCLASSIFIED

RESEARCH AND EXPLORATORY DEVELOPMENT   III/7
Airframe Structures A33BBE
Support: ORD-035
M. B. Tate
January-March 1967

RADOME THERMAL STRESS INVESTIGATION

Large thermal stresses and deformations are generated in the radomes of interceptor missiles by aerodynamic heating during hypersonic flight. Investigation of their magnitudes became necessary owing to critical demands on the radome material in the tip and forward part of the radome where high temperatures and steep gradients lead to severe stressing and distortion of the structure. Meaningful solutions for the stresses and thermoelastic deformations in the radome are needed for the successful design of high-speed vehicles.

SUMMARY

Extensive numerical results, obtained from the computer program mentioned in the last progress report, were reported in Refs. 1 through 5. In Ref. 6 theoretical expressions were developed for the orthogonal components of thermoelastic displacement. Exterior and interior boundary conditions were established in Ref. 7 for numerical evaluation of arbitrary constants that occur in the solution because of integration of a fourth-order differential equation.

A number of computerized exploratory numerical studies (Ref. 1) led to determinations of convergent series and continuous functions in the main-body thermal-stress solution. Computer-program numerical data were given for wall-slope and total-shear general integrals in Ref. 2 and for particular integrals in Ref. 4. The computer-program data on thermoelastic displacements were presented in Ref. 5 for general functions and in Ref. 6 for particular solutions.

Examples of the computer-program numerical results are shown in Tables I and II for which the series are identified in Eqs. (1) to (15), inclusive of the subsequent discussion.

FUTURE PLANS

Based on the methods and formulas described in Ref. 7, a computer program was set up to calculate the integration constants numerically. This work is now underway toward evaluation of 12 constants in total-shear and wall-slope analytical functions, plus three such constants in displacement expressions. We plan to report these results as soon as possible.

Another computer program is being written for complete thermal-stress and deformation surveys throughout the radome. Results of these surveys must necessarily follow the ones referred to in the preceding paragraph, since they are contingent on numerical values of the integration constants as determined from exterior and interior boundary conditions.

BACKGROUND

Brittle ceramic materials that are used in radome construction provide little or no stress relief by plastic deformation. In consequence their thermal behavior requires careful structural design and strength determinations for reliable missile operation. Further background information on the problem is given in previous quarterly progress reports.

DISCUSSION

The series, whose sums are listed in Tables I and II, are applicable in the main body of the radome and identified according to their coefficients; i.e.,

$$s_a = \sum_{n=0}^{\infty} a_n \left(\frac{\sin \Psi - K}{\Delta K} \right)^n, \ldots,$$

$$s_p = \sum_{n=0}^{\infty} p_n \left(\frac{\sin \Psi - K}{\Delta K} \right)^n, \qquad (1)$$

where $K = \sin \Psi_c = 0.897,571$ and $\Delta K = \sin \Psi_2 - K = 0.062,429$. Functions in which the infinite series occur are the total shear Q and the wall slope V. For example, in the interval $\Psi_1 \leq \Psi \leq \Psi_2$ along the main body, the applicable expressions are shown below.

Table I

General Series Sums for Main-Body Shear and Slope

Ψ (deg-min-sec)	s_a	s_b	s_c	s_d
$\Psi_1 = $ 64-19-23	-1.252,165	-5.335,718	-1.254,514	-5.333,369
65-06-39	+0.373,323	+5.503,105 x 10_2	+0.404,769	+5.499,961 x 10_2
65-55-04	-2.309,045 x 10^2	-3.145,906 x 10_2	-2.309,526 x 10^2	-3.145,425 x 10_2
66-45-43	+2.281,686 x 10^3	-1.250,619 x 10^2	+2.280,300 x 10^3	-1.236,790 x 10^2
67-37-49	-3.733,620 x 10^3	+1.132,628 x 10^4	-3.724,956 x 10^4	+1.131,761 x 10^4
68-31-57	-4.894,666 x 10^4	-3.103,346 x 10^4	-4.893,638 x 10^4	-3.104,378 x 10^4
69-28-18	+1.805,414 x 10^5	-2.008,237 x 10^5	+1.803,220 x 10^5	-2.006,045 x 10^5
70-28-15	+8.117,134 x 10^5	+9.288,429 x 10^5	+8.117,817 x 10^5	+9.287,733 x 10^5
71-29-13	-4.582,932 x 10^6	+3.267,485 x 10^6	-4.579,413 x 10^6	+3.262,961 x 10^6
72-34-41	-1.296,720 x 10^7	-2.268,865 x 10^7	-1.297,276 x 10^7	-2.268,308 x 10^7
$\Psi_2 = $ 73-44-23	+1.160,963 x 10^8	-4.848,632 x 10^7	+1.160,017 x 10^7	-4.839,158 x 10^7

THE JOHNS HOPKINS UNIVERSITY ▪ APPLIED PHYSICS LABORATORY

UNCLASSIFIED

Table II

Particular Series Sums for Main–Body Shear and Slope

Ψ (deg-min-sec)	s_j	s_k	s_ℓ	s_p
$\Psi_1 = $ 64-19-23	$+2.352,479 \times 10^{-4}$	$-1.532,725 \times 10^{-5}$	$-3.974,900 \times 10^{-3}$	$+8.993,765 \times 10^{-6}$
65-06-39	$+6.110,815 \times 10^{-4}$	$-1.410,465 \times 10^{-5}$	$-3.935,838 \times 10^{-3}$	$+2.204,359 \times 10^{-5}$
65-55-23	$+9.853,959 \times 10^{-4}$	$-2.001,312 \times 10^{-5}$	$-4.271,001 \times 10^{-3}$	$-4.500,298 \times 10^{-5}$
66-45-43	$+1.306,398 \times 10^{-3}$	$+3.728,650 \times 10^{-5}$	$-1.183,445 \times 10^{-3}$	$-3.008,844 \times 10^{-3}$
67-37-50	$+2.303,177 \times 10^{-3}$	$+2.740,731 \times 10^{-4}$	$+1.215,572 \times 10^{-2}$	$+3.196,060 \times 10^{-2}$
68-31-56	$+3.111,189 \times 10^{-3}$	$-4.454,226 \times 10^{-3}$	$-2.646,953 \times 10^{-1}$	$+5.788,690 \times 10^{-2}$
69-28-18	$-2.690,406 \times 10^{-2}$	$-1.590,721 \times 10^{-3}$	$-9.596,586 \times 10^{-2}$	$-1.799,892$
70-27-15	$+1.471,417 \times 10^{-2}$	$+1.776,990 \times 10^{-1}$	$+1.139,876 \times 10$	$+7.900,537 \times 10^{-1}$
71-29-12	$+1.028,925$	$-1.713,493 \times 10^{-1}$	$-1.176,929 \times 10$	$+6.932,553 \times 10_2$
72-34-40	$-1.574,224$	$-5.800,904$	$-4.156,928 \times 10_2$	$-1.142,234 \times 10_2$
$\Psi_2 = $ 73-44-23	$-3.262,710 \times 10$	$+1.338,168 \times 10$	$+1.032,594 \times 10_3$	$-2.499,510 \times 10_3$

$$\frac{Q}{Eh} = \sin \Psi \, (K_0 + K_1 s_a + K_2 s_b + K_3 s_c + K_4 s_d)$$

$$- \frac{K_5 R_c \sin \Psi}{r_c} + \frac{R_c^2 \sin \Psi}{r_c^2} \, (K_6 s_j + K_7 s_p \cos \Psi), \tag{2}$$

$$V = \frac{r_c}{R_c}(-K_v + K_1' s_a + K_2' s_b + K_3' s_c + K_4' s_d)$$

$$+ \frac{R_c}{r_c}[K_6(\nu s_j + \beta^2 s_k) + K_7(\beta^2 s_\ell + \nu s_p) \cos \Psi]. \tag{3}$$

The K_i are constants of integration, constants K_i' are calculable in terms of the K_i, and

$$R_c = 64.679 \text{ inches}; \quad r_c = R_c(\sin \Psi - K); \tag{4}$$

$$\nu = 0.244; \quad \beta^2 = 869.130,482; \quad h = 0.250 \text{ inches}, \tag{5}$$

where h is the radome-wall thickness and β is the wall-bending parameter computed with Eq. (6):

$$\beta^4 + \nu^2 = 12(1-\nu^2) \, (R_c/h)^2 , \tag{6}$$

The symbols Q and V in the foregoing equations represent the shearing-stress resultant and thermoelastic wall slope, respectively, and Ψ denotes the coordinate angle. Numerical values of the s_i (i = a, b, ..., p) are listed in Tables I and II.

The series were summed with the first two-hundred terms in each case, and coefficients were calculated from programmed recurrence formulas as exemplified by the following relations.

$$a_0 = b_0 = c_0 = d_0 = +1 \tag{7}$$

$$(a_n)_{n \geq 1} = (\gamma_n a_{n-1} a_{n-2}) - (\delta_n b_{n-1} + \omega_n b_{n-2}); \tag{8}$$

$$(b_n)_{n \geq 1} = (\gamma_n b_{n-1} + \lambda_n b_{n-2}) + (\delta_n a_{n-1} + \omega_n a_{n-2}); \tag{9}$$

$$(c_n)_{n \geq 1} = (\gamma_n c_{n-1} + \lambda_n c_{n-2}) - (\delta_n d_{n-1} + \omega_n d_{n-2})$$

$$+ (\mu_n a_{n-1} + \rho_n a_{n-2}); \tag{10}$$

$$(d_n)_{n \leq 1} = (\gamma_n d_{n-1} + \lambda_n d_{n-2}) + (\delta_n c_{n-1} + \omega_n c_{n-2})$$

$$- (\mu_n b_{n-1} + \rho_n b_{n-2}) . \tag{11}$$

The Greek-letter multipliers were computed with

$$\mu_n = \frac{K(\Delta K) \sec^2 \Psi_c}{n(n+2)} , \quad \rho_n = \frac{(\Delta K)\mu_n}{K} ,$$

$$\gamma_n = (2n^2 + n - 2)\mu_n , \tag{12}$$

$$\lambda_n + (n^2 - n - 1)\rho_n , \quad \delta_n = \beta^2 \mu_n , \quad \omega_n = \beta^2 \rho_n , \tag{13}$$

and each series in the general solution satisfies the following fourth-order differential equation:

$$(L^4 + \beta^4) \, (r_c s_i) = 0 , \tag{14}$$

$$L^2(s_i) = \frac{r_c \csc \Psi}{R_c} \frac{d^2 s_i}{d\Psi^2} + \cot \Psi \frac{ds_i}{d\Psi} - \frac{R_c s_i \cos \Psi}{r_c \tan \Psi} , \tag{15}$$

where the operator (L^2) is defined by the final equation.

REFERENCES

1. M. B. Tate, "Computer-Program Preliminary Results for Thermal-Stress Analysis of the Main Body of an Ogival Radome," APL/BBE EM-4085, 1967.
2. M. B. Tate, "Computer-Program Numerical General Integrals for Thermoelastic Slope and Shear in the Main Body of an Ogival Radome," APL/BBE EM-4087, 1967.
3. M. B. Tate, "Computer-Program Numerical Particular Functions for Thermoelastic Displacements in the Main Body of an Ogival Radome," APL/BBE EM-4091, 1967.
4. M. B. Tate, "Thermoelastic Displacements in the Main Body of an Ogival Radome," APL/BBE EM-4088, 1967.
5. M. B. Tate, "Computer-Program Numerical Particular Integrals for Thermoelastic Slope and Shear in the Main Body of an Ogival Radome," APL/BBE EM-4089, 1967.
6. M. B. Tate, "Computer-Program Numerical General Functions for Thermoelastic Displacements in the Main Body of an Ogival Radome," APL/BBE EM-4090, 1967.
7. M. B. Tate, "Thermoelastic Boundary Conditions for a Bicentric-Ogive Radome," APL/BBE EM-4093, 1967.

RESEARCH AND EXPLORATORY DEVELOPMENT   III/8
Structural Elastic Studies A33BBE
Support: AIR-320
N. Rubinstein
January–March 1967

VIBRATION STUDIES

In guided missile development it is important to know precisely the frequencies of free vibration of elastic structures and structural elements. For the missile as a whole the frequencies and mode shapes in bending and torsion have a strong influence on performance of the control system. The frequencies and mode shapes of such other structural components as wings, fins, and panels are crucial in their aeroelastic (flutter) behavior in flight.

The free vibration of only the most elementary structural elements can be analyzed "exactly;" therefore, approximation methods must be used to estimate the vibration characteristics of all others. The object of our vibration studies is to develop suitable rigorous approximation techniques and to apply them to problems of elastic structural vibration.

SUMMARY

In the past period, while working on the torsional vibration problem (Ref. 1), the companion bending problem has also been extensively examined.

This research has developed a computer program that applies estimation procedures and calculates upper and lower bounds to nonzero bending frequencies of missiles. As input data the program requires the missile bending stiffness and mass per unit length, both of which are taken to be piecewise constant.

The upper bounds are calculated by means of the Rayleigh-Ritz procedure, while the more difficult process of obtaining lower bounds is accomplished with the method of special choice developed by Bazley and Fox (Ref. 2, Sec. IIIA.2).

The program was used to compute bounds to bending frequencies of a "missile" whose stiffness variation is piecewise constant and is approximately the cubic $(1 + \frac{x}{185})^3$ where the x's denote stiffness stations (see Fig. 1, solid line). The mass per unit length was assumed to approximate the linear function $(1 + \frac{x}{185})$, where the x's here denote the mass stations (see Fig. 2, solid line).

The dashed lines in Figs. 1 and 2 represent the piecewise constant stiffness and mass per unit length respectively.

Table I exhibits the first ten upper and lower bounds to frequencies (cps) of the structure that resulted from 15th order matrix calculations.

In addition to giving upper and lower bounds for a particular stiffness and mass distribution, the program can also be used in early stages of missile development to show the sensitivity of changes in stiffness and mass upon frequencies.

Fig. 1   Bending Rigidity and Approximation. (90658)
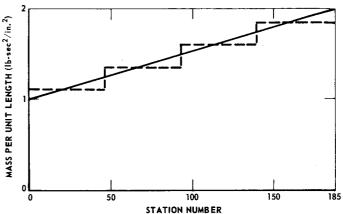
Fig. 2   Mass and Approximation. (90659)

Table I
Bounds to Nonzero Bending Frequencies (cps) of a Missile

ν	Lower Bounds, 15th Order	Upper Bounds, 15th Order
1	1.4544313	1.5115942
2	4.1137181	4.1408318
3	8.0768301	8.1153963
4	13.426615	13.453415
5	20.253893	20.409375
6	27.826209	27.986376
7	37.800765	37.964849
8	48.085409	48.381118
9	59.685344	60.246433
10	73.344190	73.711460

FUTURE PLANS

Applications of upper and lower bound procedures to problems of missile frequency estimations will continue. A program that will accept not only piecewise constant but also piecewise linear input data for missile torsional and bending frequencies will be developed.

Moreover, the final programs for missile torsional and bending frequencies will be optimized to run in a minimum of time, and provisions for accepting data in engineering units will be made.

Theoretical studies will continue, with the aim of developing and extending procedures for estimating eigenvalues (frequencies), eigenfunctions (mode shapes), and related quantities for problems in structural vibration.

BACKGROUND

Experience and knowledge gained in applying the techniques for eigenvalue estimation to problems of torsional vibration (Refs. 2 and 3) proved very useful in the development of a computer program that calculates upper and lower bounds for bending frequencies of missiles. The program uses the bending stiffness and mass per unit length as input data. Since the program uses stiffness and mass that are piecewise constant, fifty discontinuities in each quantity can be independently prescribed, thus enabling one to estimate the missile data closely with piecewise constant data.

DISCUSSION

The quadratic forms J_A and J_B for the problem of bending vibrations of a missile of unit length are given by

$$J_A(u) = \int_{-\frac{1}{2}}^{\frac{1}{2}} h(x) \, [u''(x)]^2 \, dx \, ,$$

and

$$J_B(u) = \int_{-\frac{1}{2}}^{\frac{1}{2}} B(x) \, [u(x)]^2 \, dx \, ,$$

where the mass per unit length $B(x)$ and the bending stiffness $h(x)$ are assumed to be piecewise constant and bounded by constants h°, H, m, and M as follows:

$$0 \le m < B(x) < M \, ,$$

$$0 < h^\circ < h(x) \le H \, .$$

In order to apply the lower bound method, we decompose the quadratic form J_A into the sum of two quadratic forms,

$$J_A(u) = J_{A^\circ}(u) + J_{A'}(u) \, ,$$

where J_{A° is the resolvable quadratic form given by

$$J_{A^\circ}(u) = \int_{-\frac{1}{2}}^{\frac{1}{2}} h^\circ \, [u''(x)]^2 \, dx \, ,$$

and $J_{A'}$ is the positive semidefinite quadratic form given by

$$J_{A'}(u) = \int_{-\frac{1}{2}}^{\frac{1}{2}} [h(x) - h^\circ] \, [u''(x)]^2 \, dx \, .$$

The quadratic form J_B is decomposed into the difference of two quadratic forms

$$J_B(u) = J_{B^\circ}(u) - J_{B'}(u) \, ,$$

where J_{B° is the resolvable quadratic form given by

$$J_{B^\circ}(u) = \int_{-\frac{1}{2}}^{\frac{1}{2}} M[u(x)]^2 \, dx \, ,$$

and $J_{B'}$ is the quadratic form given by

$$J_{B'}(u) = \int_{-\frac{1}{2}}^{\frac{1}{2}} [M - B(x)] \, [u(x)]^2 \, dx \, .$$

The base problem used in the procedure is the eigenvalue problem corresponding to the variation $\delta \, [J_{A^\circ}/J_{B^\circ}]$. This base problem is given by

$$A^\circ u - \lambda \, B^\circ u = 0 \, ,$$

$$u'' \, (-\tfrac{1}{2}) = u'' \, (\tfrac{1}{2}) = u'''(-\tfrac{1}{2}) = u'''(\tfrac{1}{2}) = 0 \, ,$$

where $A^\circ u = h^\circ u''''$ and $B^\circ u = M \, u$. This problem can be solved explicitly since it is the eigenvalue problem associated with the bending vibration of a shaft with uniform stiffness h° and uniform mass per unit length M. The eigenvalues and normalized eigenvectors of the base problem are given by

$$\lambda_\nu^\circ = \frac{h^\circ}{M} \, \alpha_\nu^4 \, , \quad \text{for } \nu = 1, 2, \ldots \, ,$$

and

$$u_\nu^\circ(x) = \begin{cases} \dfrac{\sqrt{2}}{\sqrt{M(\cosh^2 \frac{\alpha_\nu}{2} + \cos^2 \frac{\alpha_\nu}{2})}} \, [\cosh \frac{\alpha_\nu}{2} \cos \alpha_\nu x \\ \qquad + \cos \frac{\alpha_\nu}{2} \cosh \alpha_\nu x], \text{ for } \nu = 1, 3, 5, \ldots, \\[2em] \dfrac{\sqrt{2}}{\sqrt{M(\sinh^2 \frac{\alpha_\nu}{2} - \sin^2 \frac{\alpha_\nu}{2})}} \, [\sinh \frac{\alpha_\nu}{2} \sin \alpha_\nu x \\ \qquad + \sin \frac{\alpha_\nu}{2} \sinh \alpha_\nu x], \text{ for } \nu = 2, 4, 6, \ldots, \end{cases}$$

where the α_ν's are the roots of the transcendental equations

$$\tan \frac{\alpha_\nu}{2} + \tanh \frac{\alpha_\nu}{2} = 0, \text{ for } \nu = 1, 3, 5, \ldots,$$

and

$$\tan \frac{\alpha_\nu}{2} - \tanh \frac{\alpha_\nu}{2} = 0, \text{ for } \nu = 2, 4, 6, \ldots,$$

The method of special choice uses these eigenvalues and eigenvectors in conjunction with some auxiliary vectors to generate a finite matrix whose eigenvalues yield the desired lower bounds. The upper bounds were obtained using the Rayleigh-Ritz procedure with the u_ν°'s as trial vectors.

REFERENCES

1. J. T. Stadter, "Vibration Studies," Section III/6, Research and Development Programs Quarterly Report, July-September 1966, APL/JHU U-RQR/66-3.
2. N. W. Bazley and D. W. Fox, "Methods for Lower Bounds to Frequencies of Continuous Elastic Systems," Zeits. angew. Math. u. Phys., Vol. 17, 1966 (also reported in APL/JHU TG-609, October 1964).
3. N. Rubinstein, "Vibration Studies," Section III/7, Research and Development Programs Quarterly Report, April-June 1966, APL/JHU U-RQR/66-2 (also reported in AQR/66-2).

N67-33371

TRANSPIRATION COOLING INVESTIGATIONS

Gas transpiration cooling offers a means of protecting critical areas on high-speed flight vehicles. Theoretical methods of coupling external transpiration cooling calculations to flight-body temperature calculations are being developed. Compact duct transpiration cooling systems are needed in such areas as the leading edge, but published data cover only noncompact plenum systems. Tests of flow and heat transfer in transpiring ducts are therefore needed as adjuncts to computer program development.

SUMMARY

In gas flow through the porous walled passage of a transpiration system the pressure drop between the inner and outer surfaces of the tube wall affects the mass loss through the wall, which in turn affects the pressure drop of the main flow along the passage. Experimental measurements of mass flow variation and pressure distribution in porous tubes are needed before an analytical method can be completed for predicting these quantities. Previously a test apparatus was developed to measure the mass discharge rate and the internal static pressures along the axis of a 1/4-inch OD, 2-micron porous tube, as reported in Ref. 1. This apparatus has been modified by the substitution of a cylindrical mass discharge sampling device (Fig. 1) for the straight rubber hose previously in use. The cylindrical device gives a mass discharge rate that is an average circumferential value. It also keeps a nearly constant sampling area, even when moved to different locations on the tube. The improved device can measure mass discharge rates to an accuracy of ±2% over the range of 0.6×10^{-4} to 2.5×10^{-4} lb/sec per inch of porous tube length.

Using the apparatus shown in Fig. 1, new mass flow measurements were made along the 0.25-inch-diameter porous tube. The results were of the same type as presented in Ref. 1; namely, a highly nonuniform discharge distribution presumably caused by extremely irregular tube porosity. Because of this nonuniformity the tube was discarded, and two new tubes having a finer pore size and a thicker wall were purchased. These new stainless steel tubes have a 0.4-inch OD and a 0.16-inch ID and a porosity of one micron; their lengths are 8.25 and 9.5 inches.

Mass flow measurements were made along the lengths of each of these tubes, and, as would be expected, the decreased pore size and increased wall thickness caused a considerable increase in flow resistance. Thus, the internal static pressure level had to be raised (a factor of approximately 100) to obtain mass discharge rates comparable to those of previous tests on the 2-micron tubes. The overall results for the 1-micron tubes showed a linear variation of mass flow rate with pressure, in
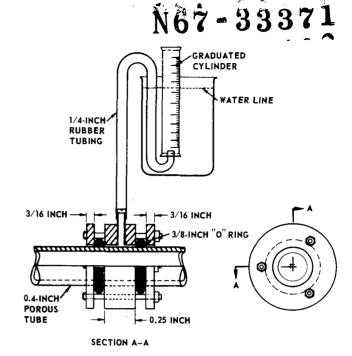

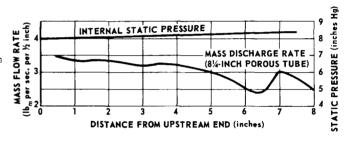Fig. 1   Sampling Device. (90666)

Fig. 2   Static Pressure and Mass Flow Rate versus Distance from the Upstream End for a Porous Tube of 1-Micron Porosity. (90667)
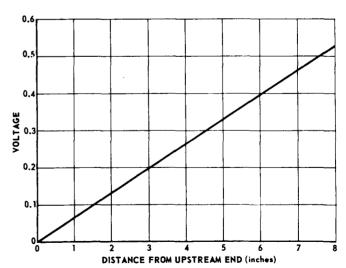

Fig. 3   Voltage versus Distance along a Stainless Steel 1-Micron Porous Tube. (90668)

agreement with Darcy's law for incompressible, isothermal flow. The internal pressure variation in the axial direction was small compared to the internal static pressure level. This variation and the associated mass discharge rate for the 8.25-inch tube are shown in Fig. 2. As with the earlier 2-micron tube, the results show the tube to be of nonuniform porosity; however, the first 5 inches of the tube vary nearly linearly which should be sufficient for heat transfer measurements.

In preparation for the heat transfer tests, measurements were made of the electrical resistance per unit length of the tubes (Fig. 3). This was accomplished by passing a current through the tube and measuring voltage drop at 1-inch intervals. The straight-line variation indicated in Fig. 3 shows that the electrical resistance is uniform along the tube, indicating a uniform metallic flow path in the axial direction. Detailed voltage surveys near the 7-inch station did not indicate a metallic flow path variation comparable to the variation suggested by the swing in the local mass discharge curve of Fig. 3.

A computer program has been prepared to aid in the computation of the tubes' friction factor with suction. For each incremental length of tubing, the program computes the mass flow rate, Reynolds number, stream velocity, suction rate (radial velocity at the inner wall/average stream velocity), total internal static pressure drop, pressure drops owing to momentum and friction, and the friction factor. The equations and general solution that were programmed are the same as given in Ref. 1.

FUTURE PLANS

Work will continue on making experimental determinations of friction coefficient and heat transfer coefficient of porous tubes. The 8.25-inch tube will be shortened to minimize flow resistance variation along the tube. Work on developing a method of attaching fittings to the ends of the porous tube without influencing the flow will also continue. The present method of silver soldering the fittings must be further evaluated, since tests to date indicate a change in flow resistance in the tube wall when the silver solder is used.

Additional work on the theoretical method for predicting heat transfer to a compact transpiring surface will be done. Following this work, a transpiration computer program to facilitate using this method will be constructed.

BACKGROUND

Considerable work was done toward developing a mathematical method for predicting heat transfer to a transpiration cooled surface. Because no experimental information existed concerning the flow characteristics and heat transfer data for porous wall tubes, an experimental program was organized for obtaining such information. A porous tube (annular flow) apparatus has been under development to determine basic friction-factor and heat transfer data. The friction factor is deduced

from pressure-drop measurements. Pressures are obtained from a static-pressure survey tube located on the axis of the porous tube.

DISCUSSION

The present cold flow test data reduction procedure is based on the one-dimensional flow equation cited in Ref. 1 as:

$$dp = - [\rho d(u^2) + 2 \; \frac{f\rho u^2}{D} \; dx] \, ,$$

where $[\rho d(u^2)]$ is the momentum decrease and

$[2 \frac{f\rho u^2}{D} \; dx]$ is the friction. Pressure measurements provide a finite difference value for dp, and the flow metering system plus the sampling device provide data for evaluating the finite difference value of $\rho d(u^2)$. From this information the friction factor, f, in the third term can be evaluated. In the wrapped-tube tests $f = f_o$ is determined with the momentum term eliminated. In the unwrapped tube tests the primary mass flow decreases in the flow direction, with the result that far downstream measurement of the small finite difference values requires extremely sensitive detectors and flow that is quite steady.

After obtaining the two new 1-micron tubes, measurement of the friction factors without suction were first made. This was accomplished by wrapping the tube with friction tape to block radial flow. The friction factors were then obtained for several Reynolds numbers by measuring internal static pressures along the tubes. These data were quite consistent and indicated a tube roughness slightly higher than Moody's smooth tube (Ref. 2). A roughness factor of approximately 500 was indicated.

In addition to the above work, a method was decided upon for attaching end fittings to the porous tube. By silver soldering a brass fitting to the downstream end of the 9.5-inch tube, a good electrical contact was achieved. Measurements of the porous tube flow resistance before and after soldering disclosed that the flow resistance had increased nearly 50% over a portion of the tube remote to the solder connection. The cause for this change has not been determined, but condensation of solder flux on the inner porous wall or a pore change caused by heating are two possibilities under consideration. Presently this problem is being investigated. A dependable fitting attachment method is needed.

REFERENCES

1. R. W. Allen, R. W. Newman, and L. B. Weckesser, "Transpiration Cooling Investigation," Section III/9, Research and Development Programs Quarterly Report, October-December 1966 (U) (Confidential), APL/JHU RQR/66-4 (also in AQR/66-4).
2. L. F. Moody, "Friction Factors for Pipe Flow," ASME Trans., Vol. 66, No. 8, November 1964.

N67-33372

HIGH-TEMPERATURE STRUCTURES AND MATERIALS

Structural problems of hypersonic airframes are strongly influenced by limitations of materials at high temperatures. In this project, structural concepts are evaluated, and appropriate materials are tested in order to establish a sound approach to the design of such vehicles.

SUMMARY AND CONCLUSIONS

A series of tests of the creep strength of an 87.5% tantalum-10% tungsten-2.5% hafnium alloy at 2400° - 3000°F were completed during this quarter. This alloy, designated as T-222 by the producer (Westinghouse Electric Corp.), is among the strongest refractory alloys available for service at temperatures above 2400°F. Relatively few data are available on alloy strength during very short-time loadings as are anticipated for typical hypersonic vehicles. The present tests were carried out to obtain such information.

Test specimens consisted of 1/2-inch-wide strips that were either 10 or 4 inches long. These strips were cut from an experimental sheet of 0.040-inch-thick material obtained as a product of the Bureau of Naval Weapons Refractory Metals Sheet Rolling Program (Ref. 1). The specimens were coated with tantalum disilicide for oxidation resistance by the Solar Aircraft Company, using a proprietary process in which the specimens are heated to elevated temperature in the presence of vapor-containing compounds that decompose to deposit silicon metal on the alloy. The silicon then reacts to form a silicide of the base metal. The coating provides protection for several hours at 2800°F and is useful for shorter periods at 3000°F.

The present creep tests were done in a dead-weight loading apparatus (Ref. 2) in which the specimens were resistively heated to the test temperature. Temperatures were controlled and recorded by means of optical pyrometers. True temperatures were obtained from emissivity measurements made in the course of this work. Most of the specimens were 10 inches long; on these the strain was measured on a 2-inch gage length by means of a "bent beam" extensometer (Ref. 3). On the 4-inch-long specimens the strain was measured optically by means of a cathetometer sighting on slivers of pyrolytic boron nitride as markers. The latter technique was used in some runs at slow strain rates associated with relatively low temperatures and stresses and was used to supplement data gathered from the 10-inch specimens.

The results are partially summarized on Fig. 1, which shows the time to 1% creep as a function of stress at the different temperatures. Detailed data and similar figures for the smaller and larger strains have been presented elsewhere (Ref. 4). Broad shaded areas on the
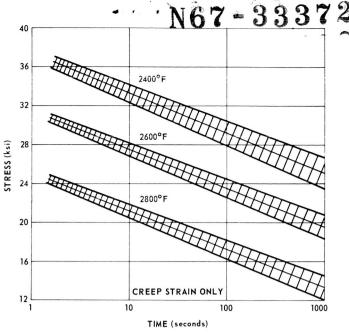

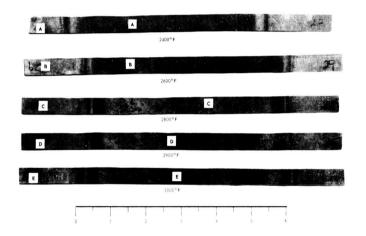Fig. 1 T222 Alloy–Stress versus Time to 1% Creep Elongation. (90737)

Fig. 2 Appearance of Disilicide Coated T222 Creep Specimens Tested at Various Temperatures. (90739)

figure show the degree of scatter in the data, which was somewhat larger than can be attributed to experimental errors in measurement. Metallographic examination of the starting material, coated material, and tested material revealed that (a) the raw material was stress-relieved but not fully annealed, (b) recrystallization or further annealing occurred during coating, and (c) variations in grain size resulted from the above circumstances. The observed variation in grain size would be expected to cause variations in creep strength as indicated by the scatter in the data.

The typical conditions of the coating after tests at temperatures up to 3000°F are shown in Fig. 2. None of these are catastrophic failures, but rather consist of small bubbles that ruptured and resealed. The 3000°F specimen was heated for 210 seconds; those below this
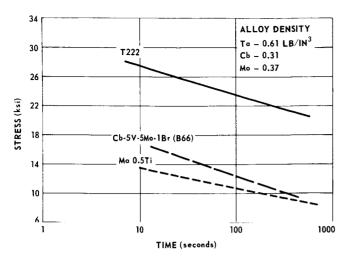
Fig. 3 Time for 1% Creep Elongation of Three Coated Refractory Alloys at 2600°F. (90738)

were heated for longer periods. It is likely that catastrophic failure at 3000°F would result in less than five minutes.

FUTURE PLANS

In previous work several refractory materials were examined and proven suitable to withstand heating conditions that would exist on stagnation regions of sharp leading edges. Problems of structural and chemical compatibility between these materials and the presently investigated silicide coatings must be investigated to insure satisfactory performance of load-bearing assemblies. An alternate coating system, based on slurry deposits of silicides, which may be used as a high temperature brazing alloy, will also be investigated.

BACKGROUND

Previous work has shown that an oxidation resistant alloy of 80% hafnium-20% tantalum is perhaps one of the best materials available for small-radius leading edges on inlets, wings and control surfaces of hypersonic vehicles (Ref. 5). This material is useful at temperatures near 4000°F and is resistant to erosion and and thermal shock and is both machinable and weldable. However, it is very expensive, and this makes it desirable to consider it for use only in critical stagnation regions and to search for lower-cost materials for the main structures. In addition to its high cost, the hafnium alloy is not as strong as many of the more commonly available refractory alloys of columbium, tantalum, and molybdenum. However, alloys in the latter classes oxidize very rapidly at temperatures as low as 2000°F and must be protected by coatings if their strength properties are to be used effectively.

A variety of coatings have been developed for such alloys, most of which are based on formation of thin films of silicide compounds on the surface. Typically, these coatings are useful only at temperatures up to about 3000°F. This capability will be adequate for most portions of hypersonic surfaces at positions away from stagnation points; further, because of the improved

strength, the relatively lower cost and wider experience with these alloys (compared to the hafnium-tantalum alloy), they are considered the best candidates for uninsulated airframe components.

The T-222 alloy tested here is not as strong as some available tungsten alloys but is nearly comparable at temperatures up to about 3500°F. It is considered superior to tungsten alloys in the present program because it is ductile, machinable, and weldable. Considerable difficulty is encountered in these areas with tungsten base alloys. In Fig. 3, some of the present results are shown in comparison to previous tests performed on molybdenum-0.5% titanium alloy and one of the stronger columbium alloys, B66 (Ref. 6). As seen here, at 2600°F the T-222 alloy is approximately twice as strong as the other two alloys. This factor will be important in volume-limited structures, such as leading edges, which may have geometric restrictions in the thickness of materials that can be employed. On a strength to weight basis, the columbium alloys are superior when temperatures below 2600°F and relatively short loading cycles are to be encountered. Typically, however, at 2800°F and above, the T-222 alloy appears superior even when density is taken into consideration.

Most all available coatings for such alloys consist of a surface film whose success hinges on the formation of an adherent, insoluble oxide film as compared to a spalling oxide or gaseous oxide phase of the base material. In the case of silicide coatings, silica (SiO_2) is formed. At temperatures above 2800°F, this is a viscous, glassy material that becomes more and more fluid as temperature is increased. In the case of the 80Hf-20Ta alloy, an oxide layer of hafnium that is stabilized by small amounts of tantalum oxide is formed. Two problems can be anticipated in performance of structures in which these two materials are to be joined. First, there may be minor fluxing reactions between the silica and hafnia, resulting in high fluidity of the oxide in regions near joints. Second, considerable volume expansion occurs during oxidation of the 80Hf-20Ta alloy, and this growth may introduce complicated mechanical loads in riveted joints or welded regions. Investigation of these and other fabrication problems is planned.

REFERENCES

1. R. L. Ammon, A. M. Filippi, and D. L. Harrod, Pilot Production and Evaluation of Tantalum Alloy Sheet, Westinghouse Astronuclear Labs. WANL PR-MO14, October 1965.
2. J. M. Akridge, Short-time Creep Strength of Molybdenum 0.5% Titanium Alloy at Elevated Temperatures, APL/JHU TG-737, November 1965.
3. M. L. Hill and J. M. Akridge, "High Temperature Materials," Section V/19, Aeronautics Division Quarterly Review, January 1964 (U) (Confidential), APL/JHU SR 7-4.
4. R. O. Weiss, "Short-time Creep Strength of T-222 Alloys," APL/JHU BFR 67-1, March 1967.
5. M. L. Hill, "Materials for Small Radius Leading Edges for Hypersonic Vehicles," AIAA 8th Annual Conference on Structures and Materials, Palm Springs, California, 30-31 March 1967.
6. W. C. Caywood, D. L. Coble, and M. L. Hill, Properties of B-33 and B-66 Columbium Alloys at Elevated Temperature, APL/JHU TG-671, March 1965.

RESEARCH AND EXPLORATORY DEVELOPMENT III/11a
Limitations of Current Radomes A33BBE
Support: ORD-035
W. C. Caywood
January–March 1967

MECHANICAL PROPERTY TESTS ON Al₂O₃ AND SiO₂

In the APL radome limitation program the performance limits of several materials and types of construction are being evaluated for use in high-speed radomes. Two of the materials under consideration are alumina (Al_2O_3) and fused silica (SiO_2). Monolithic as well as sandwich-walled constructions are being studied. For the prediction of thermal stresses and strength of such structures, data were required on modulus of elasticity (E), modulus of rupture (MOR), and thermal expansion ($\alpha \Delta T$). Experimental tests were run to determine these data for dense SiO_2 and porous Al_2O_3.

SUMMARY

Alumina (Al_2O_3) sandwich construction consisting of thin, dense face sheets and porous, homogeneous cores as well as monolithic-walled, fused silica (SiO_2) are currently being evaluated as part of the APL radome limitation program. In support of this effort, experimental tests were run at APL on three fused-silica and four alumina specimens to determine the room temperature modulus of elasticity and modulus of rupture. Measurements of the thermal expansions of these materials were made for APL by General Electric/Baltimore.

Values of E and MOR derived from the APL tests are summarized in Table I. The thermal expansion data obtained from the GE tests are presented in Figs. 1 and 2.

Based upon the limited amount of test data, some gross observations have been made.

1. The porous Al_2O_3 had a modulus of elasticity about six-and-one-half times greater and a modulus of rupture about one-and-one-half times greater than those reported in Ref. 1 for a three-point loaded specimen. The thermal expansion values are similar to those reported in Refs. 1 and 2 for nonporous Al_2O_3.

2. The SiO_2 modulus of elasticity and modulus of rupture values are less than half those reported in Ref. 2, and the thermal expansion is about 25 to 30% greater than the values reported in Ref. 2 for nonporous fused silica.

The results of this testing (reported in Ref. 3) have been used in the APL studies relating to the comparison of theoretical thermal stresses with experimentally determined thermal stresses.
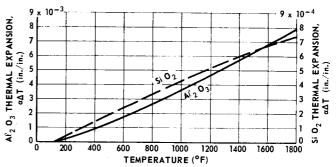
Fig. 1   Thermal Expansion of 10% Porous Fused Silica and 70% Porous Alumina. (90676)
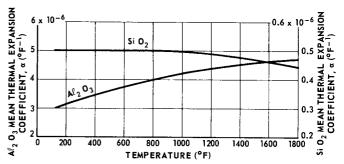

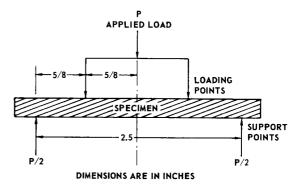Fig. 2   Mean Thermal Coefficient of Expansion (from 122° to 1800°F.) (90677)

Fig. 3   Schematic Illustrating Loading on Test Specimen. (90678)

FUTURE PLANS

Two Al_2O_3 sandwich cylinders have been ordered and will be subjected to experimental thermal stress

Table I

Summary of Leading Edge Materials Tests

Specimen	Density (gm/cc)	Width (in.)	Thickness (in.)	E (10^6psi)	MOR (psi)
Al_2O_3 No. 2	1.25	0.501	0.255	--	1290
Al_2O_3 No. 3	1.20	0.505	0.245	1.90	1015
Al_2O_3 No. 4	1.20	0.503	0.250	1.86	1295
Al_2O_3 No. 5	1.26	0.504	0.256	1.99	1500
SiO_2 No. 1	1.93	0.480	0.250	3.50	3500
SiO_2 No. 2	1.98	0.458	0.245	3.69	3480
SiO_2 No. 3	1.96	0.485	0.255	--	2540

evaluation. It is anticipated that after these cylinders have been tested specimens will be cut from the core material and mechanical property tests will be conducted.

BACKGROUND

Theories for analyzing thermal stresses in ceramic sandwich structures have been developed (Refs. 4 and 5), and experimental thermal strain data have been obtained on an alumina sandwich frustum of finite length (Ref. 6). A correlation between the theoretical and experimentally determined thermal stresses has been made, using the material property reported herein; the findings of the correlation study are reported in Ref. 7.

DISCUSSION

The MOR and $\alpha\Delta T$ data were obtained by conventional testing techniques. For the E determination, deflection measurements were taken during the MOR tests, and E was derived from these data. Sonic testing is the more conventional method for determining E for brittle materials. To gain assurance that the instrumentation and procedure used for obtaining E in the APL tests was satisfactory, a metal bar of known E was tested and the results obtained were exceptionally good. In the MOR tests a conventional four point loading fixture was used. A schematic illustrating the loading on the test specimens is shown in Fig. 3.

For the Al_2O_3 tests the loading was applied by means of the dead weight system. Loading was in increments of 1 pound, and the average failing load was about 20 pounds. Since the SiO_2 material required higher breaking loads, the loading for these tests was applied in increments of about 10 pounds by a Baldwin hydraulic testing machine. The average breaking load was about 50 pounds. Deflections of the specimen were taken at the specimen mid-span and at the specimen support points; the difference between the readings was used in the computation of E. The MOR value was computed from the load required for failure.

For a beam supported and loaded as illustrated, the modulus of elasticity, E, can be expressed by

$$E = \frac{2.68}{bt^3 \frac{\delta}{p}},$$

where

b = width of specimen (inches)
t = thickness of specimen (inches)
δ = mid-span deflection (inches)
p = applied load (pounds)

From a plot of the test data the slope (δ/p) of the mid-span deflection-load curve was determined for use in the computation of E.

The MOR strength is readily derived for a beam of the geometry tested and can be expressed by

$$MOR = 1.875 \frac{p_{max}}{bt^2},$$

where p_{max} = total applied load at failure, including tare in pounds. Values of E and MOR derived from the test data have been presented in Table I.

The thermal expansion tests were conducted on specimens 0.25 by 0.25 by 2.56 inches long. One specimen of SiO_2 and one of Al_2O_3 were tested by GE/Baltimore using a standard technique of recording the change in length of a specimen bar with a mechanical displacement amplifier and a pen recorder. The data from these tests have been presented in Figs. 1 and 2.

The slip-cast fused-silica specimens were cut from material supplied from Georgia Institute of Technology and had an average density of 1.96 grams/cc (about 10% porous). The alumina specimens were cut from the porous core of a sandwich frustum supplied by the Brunswick Corporation, Marion, Virginia and had an average density of 1.23 grams/cc (about 70% porous).

REFERENCES

1. Ltr from R. L. VanAken, Brunswick Corporation, to L. B. Weckesser, APL/JHU, 21 January 1966.
2. L. K. Eliason and G. C. Zellner, A Survey of High Temperature Ceramic Materials for Radomes, Air Force Materials Laboratory, WPAFB, ML-TDR-64-296, September 1964.
3. W. C. Caywood, "Experimentally Determined Modulus of Elasticity, Modulus of Rupture, and Thermal Expansion for Slip Cast Fused Silica (SiO_2) and Porous Alumina (Al_2O_3)," APL/JHU BBE-EM-4083, 4 January 1967.
4. R. M. Rivello, Thermal Stress Analysis of Sandwich Cylinders, APL/JHU TG-721, August 1965.
5. R. M. Rivello, Thermal Stresses in Finite Length Sandwich Cylinders, TG report to be published.
6. R. K. Frazer, "Thermal Stress Experiments with an Alumina Sandwich Conical Shell," APL/JHU EM-4064, 21 February 1967.
7. J. F. George, "Discussion of Recent Sandwich Shell Thermal Stress Studies," APL/JHU EM-4095, 10 March 1967.

N67-33374

THERMAL STRESSES IN SANDWICH SHELLS

As part of the missile radome limitations study, the use of sandwich-constructed ceramic shells is being investigated. Sandwich shells have an obvious advantage over monolithic construction with respect to weight; however, it is suspected that the reduced thermal conductivity of the porous core may create large radial temperature gradients, resulting in high thermal stresses. Analytical formulation of these stresses has been completed, and this theory will be used to study the environmental limits of sandwich constructed missile radomes and to select the most appropriate dimensions of the sandwich layers in order to satisfy the electrical and thermal requirements of a particular flight mission.

SUMMARY

The experimental results of the thermal stress tests on the alumina sandwich cone (Ref. 1) have been used to develop theoretical values of the internal temperature distribution and thermal stress. Some of the details of the test specimen, which failed because of a local hot spot causing thermal shock, are shown in Fig. 1. Shown on the specimen are a number of the strain gages and thermocouples that were used to measure strains on the inside surface and temperatures on both surfaces.

Using the measured external temperature history (Ref. 1) as a forcer, theoretical predictions were made of temperature distributions through the specimen wall (Ref. 2). Since thermal conductivity of the core material (k_c) was an unknown, a parametric study was performed where k_c was assumed to be proportional to the thermal conductivity of the skin (k_s). The inside surface temperature histories compared with the experimental results are shown in Fig. 2. Even though these results did not agree exactly with experiment, the temperatures obtained for the case of $k_c = 3.48\, k_s$ were considered adequate for the stress analyses.

Using the temperature distributions through the wall as input, thermal stresses were determined by available computer programs. The infinite-length concentric thick-walled cylinder theory of Ref. 3 was used with the thermal analysis program to compute stress histories on the inside surface. Peak stresses (shown in Table I) occurred at 12 seconds (which agreed with experiment) so the temperature distribution at this time was chosen to be used in more accurate analyses.

Both the AVCO shell program and the finite-length, sandwich cylinder program of Ref. 4 were used. The AVCO shell program accounts for the conical shape of the test specimen and the longitudinal variations in
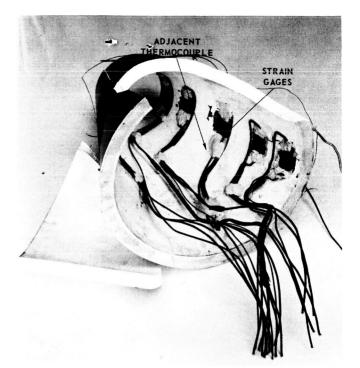

Fig. 1 Failure of Alumina Sandwich Shell Caused by Thermal Shock. (90679)

Table I

Summary of Experimental and Analytical Stress Results

Inside Surface Stress	Experimental	Infinite Length Cylinder Theory	AVCO Shell Theory	Finite Length Cylinder Theory
σ_θ	+8200 psi (*)	+13,500	+14,800	+13,700
σ_ϕ	+8000	+15,000	+14,600	+14,700

where σ_θ = circumferential (hoop) stress and

         σ_ϕ = meridional (longitudinal) stress.

(*)Positive sign indicates tensile stress

temperature, but does not include the effects of transverse shear and radial compliance of the core. The finite length, sandwich cylinder program accounts for transverse shearing and radial core compliance, but does not include the effects of the small longitudinal variations in temperature, and in this case simplifies the geometry by assuming that the mid-station stresses of the cone are similar to those of a cylinder of equal radius. The maximum, inside surface stresses at the mid-station are shown in Table I. It may be seen that the analytical predictions are some 70 to 80% greater than the experimental values.

The experimental procedures were verified, and test specimens were cut from the failed cone to measure the material properties of the core (Ref. 5). Several possible explanations for the difference between theory and experiment were advanced in Ref. 6. Basically, they assume that either the material is behaving in a manner which is not accounted for in the instantaneous-elastic theories, or the experimental sensors are providing incorrect or insufficient data. The most
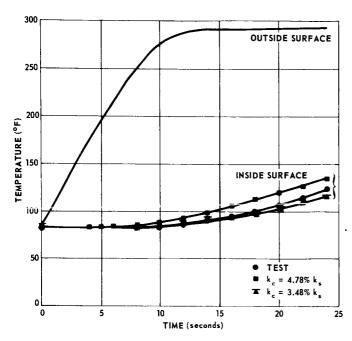
Fig. 2   Temperature versus Time for Alumina A-Sandwich Test Specimen. (90680)

values. Thus, further refinement of the conductivity was not justified. The temperature for $k_c = 3.48\%\ k_s$ at 12 seconds was used in computing stresses by the AVCO shell and the finite cylinder theories.

Neither of the analytical formulations that were used to compute stresses is exactly correct for the problem; however, each has been tested against problems whose exact solutions are known, and excellent agreement has been obtained. Since the results of both the shell and concentric thick-walled cylinder theory agree with each other within 10%, it is felt that either is appropriate for use with the alumina shell problem provided that the material behaves as assumed.

Reference 6 explores the possibility of the material deforming in an inelastic manner (i. e., crushing, slipping, and yielding). The conclusion is that this type of behavior would not explain such large differences as shown in Table I for the level of stresses involved, but it may well be an important factor in tests to higher stress levels. Also considered was the possibility of a time lag in the material response to temperature changes. This would have the desirable effect of reducing thermal stresses. However, a much more detailed experimental program would be required to verify the existence of such behavior.

In previous work with strain gages used to measure thermal strains of radomes in wind-tunnel tests, there has been a problem of heating the gage element by convection. To avoid this, the alumina shell was packed inside with fiberglas insulation, and the ends were closed with a transite sheet. As there was no pressurized air flow involved, it was felt that internal heating would not occur during the short test times. There are some indications, however, that the gage elements may have been hotter than the surface material. The difference, estimated by a rather indirect method, is approximately 10°F. When this temperature increment is used in the biaxial thermal strain equations (Ref. 1), the level of stresses increases approximately 40%. Therefore the experimentally determined stresses are very sensitive to temperature, and every effort, will be made to eliminate these differences in future tests. Also any small difference that may exist will be measured more carefully.

promising explanation assumes that the temperature of the inside surface strain gage element was hotter than the adjacent thermocouple indicated. There are indications that a difference of about 10°F may have existed, and this would have the effect of raising the experimental stresses by 40%.

FUTURE PLANS

An attempt to resolve the noted difference between experimental measurements and analytical predictions will be made by conducting an additional thermal stress test using an alumina sandwich cylinder. The procedure will be planned to minimize the areas of uncertainty in the temperature and strain sensors. After the differences between theory and experiment are understood, the radome limitations program will proceed with the optimization of the dimensions of sandwich radomes.

DISCUSSION

Thermal calculations were made to predict temperatures across the wall of the alumina A-sandwich specimen shown in Fig. 1. The experimental measurements made at the mid point along the wall were used for comparison. On Fig. 2 is shown the external surface temperature history assumed for the analysis. With this temperature as an input, transient temperature distributions through the sandwich wall were computed using the assumptions listed in Ref. 2. The thermal conductivity of the core was unknown so it was used as a parameter, and temperatures were calculated for k_cs of 100, 15, 6.74, 4.78, and 3.48% k_s. As may be seen in Fig. 2, the inside temperatures computed for $k_c = 4.78$ and 3.48% k_s lie on opposite sides of the experimental

REFERENCES

1. R. K. Frazer, "Thermal Stress Experiments with an Alumina Sandwich Conical Shell," APL/JHU EM-4064, 27 February 1967, and R. A. Frazer, et al., "Stresses in Sandwich Shells," Section III/5b, Research and Development Programs Quarterly Report, July-September 1966, APL/JHU U-RQR/66-3 (also in AQR/66-3).

2. L. B. Weckesser, "Temperature and Thermal Stress Predictions of an Alumina A-Sandwich Test Model," APL/JHU EM-4092, 10 February 1967.

3. R. M. Rivello, Thermal Stress Analysis of Sandwich Cylinders, APL/JHU TG-721, August 1965.

4. R. M. Rivello, Thermal Stress Analysis of Sandwich Cylinders of Finite Length, APL/JHU TG (to be published).

5. W. C. Caywood, "Experimentally Determined Modulus of Elasticity, Modulus of Rupture, and Thermal Expansion for Slip Cast Fused Silica (SiO_2) and Porous Alumina (Al_2O_3)," APL/JHU EM-4083, 14 January 1967.

6. J. F. George, "Discussion of Recent Sandwich Shell Thermal Stress Studies," APL/JHU EM-4095, 27 February 1967.

RESEARCH AND EXPLORATORY DEVELOPMENT III/12
Thermal Protection Systems A33BFR
Support: ORD-035
M. L. Hill
January–March 1967

HYPERSONIC LEADING EDGE STRUCTURES AND MATERIALS

The need for sharp leading edges to operate at high temperatures is one of the more critical problems in the development of hypersonic vehicles for steady cruise in the atmosphere. In this project, the environmental factors of aerodynamic heating are being defined and materials and structures are being evaluated for service in the environment.

DISCUSSION AND CONCLUSIONS

Solely on the basis of strength and oxidation characteristics of available refractory materials, it appears reasonable to expect that sharp leading edges can be made for service up to about 4000°F (Refs. 1 and 2). However, a variety of aerodynamic environmental factors influence the actual feasibility of such performance. Some of these factors are summarized on Fig. 1 along with a sketch of the hypothetical wedge-shaped leading edge to which they apply.

The upper curve of the figure shows a velocity limit curve that is imposed by an analytical restriction that the stagnation point will not be permitted to exceed 3900°F. The remaining curves show aerodynamic and structural variables that will exist in flight on this velocity limit curve. Considered in order of importance (from the point of view of material capabilities), these factors are as follows:

1. Recovery pressure behind the bow shock reaches 860 psi at sea level. This represents a severe oxidation environment for which little or no data are available on candidate materials.
2. Aerodynamic shear forces of up to 60 psi will occur on wedges aft of the cylindrical tip. Shear forces up to five times larger than this would be expected on the tip. This factor will represent a severe erosion problem to materials that achieve oxidation resistance through the formation of adherent oxide films on the surface.
3. Bending stresses within the material due to non-symmetrical loads resulting from an angle of attack of 3° reach 7200 psi at sea level. Creep deformation of the wedge could occur at this stress and temperature; this would be expected to influence the permissible maneuverability of a vehicle.
4. Cold wall heat fluxes of about 7000 Btu/ft^2 sec will exist at sea level. In a simplified sense, this extreme value can be taken as a sure indication that the stagnation point will quickly rise to temperature values very close to recovery temperature. Emissivity, heat capacity, and thermal conductivity of materials are therefore only of secondary concern.
5. Thermal gradients will exist as a function of distance from the stagnation point because of decreased heat transfer. This factor has not yet been analyzed and is not described on this figure. It may present

Fig. 1 Aerodynamic Environment Accompanying Flight at Velocities That Would Produce Leading Edge Temperatures of 3900°F. (90755)
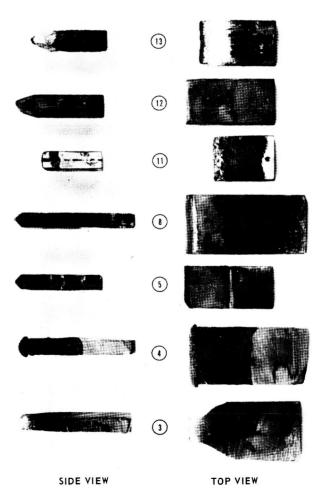

SIDE VIEW   TOP VIEW

Fig. 2 Wedge Model after Test. (90757)

Table I

Summary of Leading Edge Materials Tests

Model	Material	Wedge Angle (deg)	Radius (in)	Arc Enthalpy (Btu/lb)	Arc Press. (psi)	Model Position (in)	Local Mach No.	P_2 (psia)	Max. Temp. (°F)	Duration (sec)	Approx. Simulation on Stagnation Point		Results
											Alt. (1000 ft)	Vel. (ft/sec)	
1	65% Hafnium Carbide 20% Tantalum Carbide 15% Graphite	90	0	1650	405	2.1	4.1	30.2	3450	13	80	7500	One corner broke off at 2 seconds. No blunting occurred on remaining section of wedge.
2	70% Hafnium Carbide 30% Graphite	90	0	1500	397	2.1	4.1	29.6	3440	14	79	7480	Specimen broke vertically at the insulated mount after 12 seconds. No blunting of leading edge occurred.
3	85% Hafnium Carbide 15% Graphite	90	0	1525	394	2.1	4.1	29.4	3100	6	78	6900	Both corners broke off at about 3 seconds. Short central section was not blunted.
4	Fused Silica with 7-1/2% Cr_2O_3	90	0	1525	394	1.5	3.4	61.1	3500	3	-	-	Tip melted and ablated to a final radius of about 1/8 inch.
5	Fused Silica with 20% Tungsten	90	0	1800	378	1.5	3.4	58.5	3900	13	72	7900	No severe damage. Edge blunted to about 0.02 inch radius and small corner section broke off at 1/2 second.
6	Fused Silica with 20% Tungsten	90	0	1790	368	1.0	2.6	115	3740	4	53	7600	Model broke at mount and was lost. Films show no blunting at time of fracture.
7	78% Hf, 20% Ta, 2% Mo, Solid Slab	90	0	1500	394	2.1	4.1	29.4	3300	11	81	7200	No observable damage.
8	78% Hf, 20% Ta, 2% Mo, Solid Slab	90	0	1800	382	1.375	3.3	69.0	3910	13	65	7900	No severe damage. Tip eroded to about 0.02-inch radius.
9	90 Ta - 10 W with Sylvania Coating	30	0.03	1510	398	2.1	4.1	29.6	3400	14	80	7400	No observable damage.
10	90 Ta - 10 W with Sylvania Coating	30	0.03	1920	382	1.375	3.3	69.0	>4100*	13	66	8100	Coating melted at 7 seconds. Tantalum ignited and burned back to mount.
11	90 Ta - 10 W with Sylvania Coating	15	0.03	1900	375	2.0	4.0	30.0	>4100*	13	72	8150	Coating melted at 5.8 seconds. Model ignited and burned to mount.
12	Graphic with Sylvania Coating	45	0.06	1750	368	2.5	4.5	18.3	3540	5	92	7400	No observable damage. White adherent oxide formed on surfaces.
13	Graphite with Sylvania Coating	30	0.06	1900	383	1.375	3.3	69.1	>4100*	13	66	8100	Coating melted on tip and blew away at 6 seconds. Graphite eroded back about 1/8 inch.
14	HDB Boron Nitride	90	0	1900	382	1.5	3.4	59.2	>4100*	13	73	7450	Corner broke at 1/2 second owing to thermal shock. Tip blunted to 1/16 inch.
15	HDA Boron Nitride	90	0	1760	367	2.5	4.5	18.3	3850	13	96	7600	1/32 inch surface layer spalled during first 2 seconds. Remainder survived with little blunting.

*Pyrometers went off scale.

problems in the use of some of the more oxidation-resistant materials because of their brittleness.

A family of wedge models was tested in the PRL arc heater in a sonic orifice free jet, and a preliminary report (Ref. 3) described several materials which performed well. Subsequently, the flow field in the jet and temperature data taken on the models have been examined (Ref. 2). The aerodynamic simulations achieved in the tests have been determined and are reported in Table I. Also, each of the materials tested is described briefly and its performance is documented. High-speed and standard-speed motion pictures were taken during each test, and the large amount of film footage has been edited into an 8-minute, 16-mm color film which describes the behavior of the various materials.

Figure 2 shows some of the models after test; this is useful in describing the materials properties that are important in withstanding the environment. Numbers on the figure are those of the model descriptions on Table I.

Model 3 was a brittle material, a hafnium carbide-graphite composite, that has good oxidation and erosion resistance but failed owing to thermal stress.

Model 4 was made of fused silica having a small amount of chromium oxide added to increase its emissivity. Plastic flow of the tip caused by the pressure and shear forces in the stagnation point is clearly evident.

Model 5 was fused silica with 20% by volume of tungsten powder added to increase the viscosity over that of ordinary silica at elevated temperatures.

Model 8 was made from a solid slab of 77.5% hafnium-20% tantalum-2.5% molybdenum alloy. This model was essentially undamaged after three consecutive runs at temperatures ranging from 3300° to 4000°F.

Model 11 was made of tantalum 10% tungsten alloy coated with 80% hafnium-20% tantalum alloy. This photo

shows that excessive temperature caused melting of the coating. Models of this type performed well at temperatures up to 3900°F but failed catastrophically at about 4000°F.

Models 12 and 13 were both made of ATJ graphite with a coating of 80% hafnium-20% tantalum alloy. Model 12 shows essentially no damage after test at 3500°F while model 13 shows the result of melting of the coating when the tip exceeded 4000°F.

A more detailed discussion of the work is available in Ref. 2.

FUTURE PLANS

Work on an analytical program aimed at defining the temperatures and thermal gradients in wedges as a function of altitude, velocity, wedge angle, leading edge radius, and angle of attack has been started. The results of this will be used in defining the structures and material problems in composite design of leading edges. An investigation is also being made of test methods and facility modifications that might be used to produce suitable flow fields for testing composite wedge structures, rather than just the stagnation region as was the case in the present tests.

REFERENCES

1. M. L. Hill, "Materials for Structural Use above 3000°F," APL Technical Digest, Vol. 3, No. 4, March-April 1964.

2. M. L. Hill, "Materials for Small Radius Leading Edges for Hypersonic Vehicles," 8th Structures and Materials Conference, AIAA-ASME-Palm Springs, California, March 1967.

3. M. L. Hill, "High-Temperature Structures and Materials," Section III/10a, Research and Development Programs Quarterly Report, April-June 1966, APL/JHU U-RQR/66-2 (also in AQR/66-2).
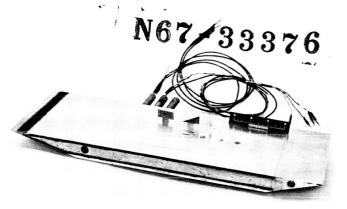
Fig. 1   3 Vane-Turbulators to be Mounted (Individually)
on Plate with Moving Element Skin-Friction
Gage (Large Circle). (90707)

MIXING DEVICES FOR DELAYING SEPARATION

Separated flows often occur despite the most careful efforts of a designer to prevent detachment of the flow from a wall, such as may take place ahead of a deflected control surface, on the ramp of a diffuser inlet, ahead of a flared-skirt stabilizer, or even in an over-expanded nozzle. It has been found possible, in many subsonic separated-flow situations, to restore full efficacy of the aerodynamic component affected by the flow separation by the expedient of installing turbulators (or flow-mixers, of one sort or another) in order to even out the energy levels of the various strata of air that are impinging on the aerodynamic component in question. Since practically no information is available at supersonic speeds concerning the effectiveness of mixing devices in bringing about improvement in the debilitated air that otherwise would be the consequence of flow separation, the gathering together of practical design data on such devices is likely to pay off in very profitable ways, inasmuch as an already completed basic design that is giving substandard performance can be salvaged, in many instances, merely by the addition of such turbulator fixes.

SUMMARY

The University of Texas is investigating in the 6-by 7-inch high-speed wind tunnel, at Mach 5, several facets of separation phenomena and ways to combat the deterioration in aerodynamic performance resulting from such unwanted flow detachments.

Initial tests have been carried out on vane-type mixing devices to determine their drag. These units have been installed, individually, on the moving-element patch of the commonly used skin-friction gage, the surface of which is aligned with the surface of a flat plate in which the assembly is mounted. The tunnel setup is shown in Fig. 1; three typical turbulator vanes are set out for display, but only one at a time is fastened to the circular disk, which is the moving element of the skin-friction gage. The summary of drag data versus aspect ratio, obtained with 24 configurations, all at 5° angle of attack, is presented in Figs. 2 (for rectangular models) and 3 (for delta-wing shapes); the raked-tip type of vane also has been tested. It should be noted that the boundary layer is 1/4-inch thick at the test location, while the vanes protrude out from the plate by 1/4 inch or 1/2 inch; thus, opportunity is afforded through vortex action for the high-energy outboard flow to be entrained into the inner, boundary-layer air with the result that the energy profile becomes more equalized, even close to the wall.

Although these models constitute familiar wing planforms, no pertinent data (theoretical or experimental) are available concerning such shapes operating within the boundary layer (or almost wholly within it), as in the present case. The surprising anomaly is made evident by these plots that the vanes that extend
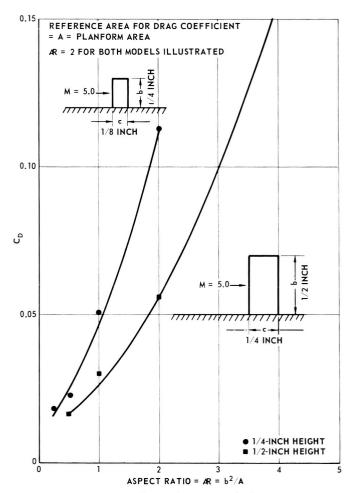
Fig. 2   Drag Coefficient for Rectangular Vane-
Turbulators versus Aspect Ratio (Angle of
Attack = 5°). (90708)

out farther into the non-debilitated flow have smaller drag coefficients, for a fixed aspect ratio. When two vanes with fixed chord are compared, however, the longer span model has a slightly higher drag coefficient. If the leading edge drag is the overwhelming contributor to the total drag, these trends become understandable.

FUTURE PLANS

The next scheduled tests will repeat the previous runs, with increase in the angle of attack to 10° and
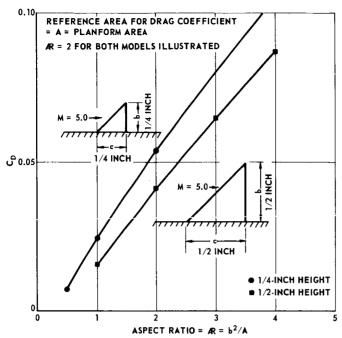
Fig. 3 Drag Coefficient for Delta-Planform Vane-Turbulators versus Aspect Ratio (Angle of Attack = 5°). (90709)

15°. Then the effectiveness of these turbulators as energy equalizers will be assessed by measuring the energy produced at a downstream location. This characteristic of turbulators may be evaluated by using another moving-element skin-friction gage installed downstream of the turbulator. If the down-steam skin friction is increased substantially over the amount occurring when the turbulator is not present, the indication would be strong that this particular turbulator is effective in bringing high-energy strata of air in close to the constraining wall. Eventually those designs that have both good equalizer action on the boundary-layer energy profile, and which at the same time do not produce prohibitively high drag, will be tested in a design situation; i.e., in front of a ramp that would normally cause separation to take place, if it were not for the presence of the turbulator (or patterned rows of them).

BACKGROUND AND DISCUSSION

In subsonic flows it has been found advantageous to place turbulators ahead of potential trouble spots in order to prevent separation from taking place in front of convexly sloping surfaces, as are prescribed, for instance, as integral features of nose inlet ramps, deflected aerodynamic flap-controls, stabilizing flared skirts, side airscoops, etc. Such devices, however, have received practically no attention for use at supersonic speeds. The reluctance to make use of such mixing devices at supersonic speeds for improvement in energy equalization and flow-separation suppression perhaps stems from the possible deleteriously high associated drag. It appears to be well worthwhile, then, to find out precisely what may be the penalty that will have to be paid for reaping the benefits that could be realized when such mixers are installed at strategic locations ahead of affected aerodynamic appendages. The

University of Texas has begun a theoretical and experimental program aimed at finding out what the relative cost (in terms of drag) will be to prevent flow separation by use of effective mixing devices (the effectiveness of the flow-energizers also has to be assessed). In previous work it was learned how to produce separation, of a controlled degree, ahead of a compression corner (see Ref. 1).

The program has progressed now to the state where turbulators in the form of miniature vanes are mounted on a flat plate for measurement of their drag in the presence of a sizeable boundary layer. Since the thickness of the boundary layer is about 1/4-inch at the test station (at the Mach 5 speed of the selected wind tunnel nozzle) the heights of the mixing devices being tried are taken to be of comparable extend (i. e., 1/4 inch to 1/2 inch). The height needs to be slightly greater than the boundary layer, it is reasoned, because it is envisioned that most of the desirable mixing action comes about through vortex shedding from the outer edges of the models. These trailing vortices, shed from the tips of the vanes under examination, are expected to act in such a way as to entrain high-energy external-stream air, directing it inward towards the wall, so as to even out the energy profile in an area close to the wall, which would otherwise be a debilitated region of boundary layer.

The first models of mixing devices being tested for drag are of the miniature airplane-wing type, because similar shapes were used successfully at subsonic speeds. The shapes fall into three categories: rectangular panels, delta vanes, and raked-tip wing planforms. The pertinent drag-coefficient versus aspect-ratio results are presented in Figs. 2 and 3.

An analytic effort is being carried along with the experimental work in order to try to organize and to derive better understanding from the observed results. The theory is based on an idealization to a single, concentrated vortex, trailing back from the outboard tip of the vane. Ordinary wing-theory is not applicable, of course, because the miniature wings are imbedded in a varying energy profile of boundary-layer air.

It is anticipated that mixing devices other than flat-plate vanes will be tested later on, although in the next immediate scheduled part of the testing program it is planned merely to obtain more drag measurements of the same wing-shapes, but at higher angles of attack (up to 15°). Following completion of the drag tests it is expected that tests will be made to determine the mixing effectiveness of each configuration. One way of measuring mixing effectiveness, roughly, is to install another moving-element skin-friction gage downstream of the turbulator, and to determine how much the skin-friction is increased over what would have been true without the forward-placed turbulator in operation. A more accurate measurement of effectiveness in energy equalization would be provided by a detailed wake survey, made throughout the flow downstream of the turbulator. Such a survey, however, requires painstaking care and a large expenditure of tunnel running time. Thus, such elaborate techniques will be avoided if the simpler skin-friction measurements turn out to serve adequately to distinguish levels of turbulator effectiveness.

The final proof of optimum configurations will depend on actual installations of promising candidate turbulators ahead of a compression corner, to prove under design conditions that separation is prevented, to all intents and purposes, at a not-too-great cost in extra drag.

REFERENCE

1. W. B. Gillette, Separation Measurements of Supersonic Turbulent Boundary Layers over Compression Corners, University of Texas, Defense Research Laboratory, Report DRL-543. Approved and reissued as APL/JHU CR-26, 21 July 1966.

SPHERICAL FOCUSED BLAST DEVICE

Focused blast is a promising concept for future antiaircraft missile warheads. It provides a means of concentrating the explosive energy in a beam that, by some means, can be aimed at a target. A sphere of explosive would be an ideal geometry if, by proper initiation, it could be made to focus its explosion products. Because of its symmetry, the blast could be aimed by electronically selecting the initiation points. Thus, the difficult task of mechanically aiming the warhead would be eliminated.

SUMMARY

Work was started this quarter to build and fire a small (2-inch-diameter) sphere of Composition C-4 to prove the concept. The sphere was initiated at 12 points (arranged as shown in Fig. 1) by lengths of Detacord cut to produce the proper delays. Several tests were performed to develop a suitable initiation system, viz., one that could reproduce the desired delays at all points with accuracy greater than 0.10 μsec. This was accomplished, and one sphere was fired. Fastex pictures of the test indicated that focusing was achieved.

FUTURE PLANS

More 2-inch spheres will be fired. For these tests pressure measurements will be made both on and off axis, and Fastex pictures will be taken of the products expanding freely for at least 5 feet from the sphere (for the one completed test the products could expand only 1.5 feet before striking the walls of the confinement box). Also, the Beckman and Whitley 189 framing camera will be used to study the initial expansion and to measure its velocity.

An initiating system using electrical detonators is being considered, and preliminary tests are being planned. This system will be for larger (7.0-inch-diameter) spheres.
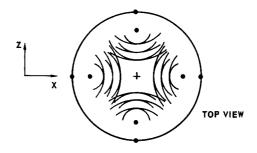
BACKGROUND

Focused blast is the term applied to explosions that, by method of initiation, shape of explosive charge, or method of confinement, are directed in a beam along some axis or are uniformly distributed in a plane around the explosive device.

Falcon Research, under subcontract to APL, measured the blast parameters around peripherally initiated charges of various geometries and compared the results with centrally initiated spheres of the same explosive. It was found that devices producing focused beams along an axis were more effective than those producing axisymmetric focused blast in a plane. Both were more effective than centrally initiated spheres
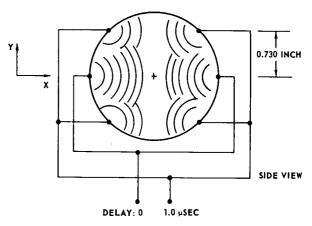

Fig. 1   Arrangement of Initiators in 2-inch-Diameter Sphere. (90631)

(Ref. 1). The focused beam type, if applied in a missile warhead, must be aimed at the target. Studies have shown that mechanical aiming is impractical because of inertial effects; therefore, aiming by electronically selecting initiating points is desirable. A spherical charge with several initiation points on its surface, chosen electronically and fired in the proper sequence, is an obvious choice for this type of warhead because of its symmetry.

PROGRESS FOR REPORTING PERIOD

Tests were undertaken to determine the effectiveness of selective multi-point initiation of a sphere of explosive in producing focused blast. The 2-inch-diameter sphere of Composition C-4 was initiated at 12 points by lengths of 0.190-inch-diameter Detacord cut to produce the proper delays. Figure 1 illustrates the arrangement of initiation points with respect to a fixed coordinate system. The four points lying in the equatorial plane, i.e., the x-z plane, were initiated at t = 0, and the eight points

lying in the two parallel planes at y = ±0.730-inch were initiated at t = 1.0 μsec. It was expected that the collapsing detonation waves would focus the explosion products in the y direction.

Before the sphere could be built and fired, it was necessary to determine if Detacord was suitable to reliably initiate the C-4 with sufficient accuracy. Several experiments using witness block techniques and ultrahigh-speed photography were performed (Ref. 2). They showed that the initiation times could be controlled with accuracy greater than 0.10 μsec, which was sufficient.

One sphere was built and fired. Fastex photographs of the test showed that focusing was achieved.

REFERENCES

1. D. K. Parks, "Investigation of Characteristics around Focused Blast Charges," APL/JHU BFM-043 (in preparation).
2. R. L. McCally, "Multipoint Initiation of High Explosives with Preselected Time Delays," APL/JHU BFM-045, 28 February 1967.

UNCLASSIFIED

RESEARCH AND EXPLORATORY DEVELOPMENT I I I/14c
Advanced Warhead Research A42 BFM
Support: ORD-0622
M. H. Friedman
January-March 1967

THERMAL EXPLOSION ANALYSES

Many aspects of the behavior of explosives during initiation and propagation can be analyzed by means of thermal explosion theory. In most cases the application of this theory leads to one or more nonlinear partial differential equations that can be solved only by numerical integration. The objective of the present work is to develop and apply an algorithm that can be used to obtain approximate explicit solutions to thermal explosion problems.

SUMMARY AND CONCLUSIONS

The solution for critical slab hot-spot size is shown to exist throughout the range of practical interest. By making suitable approximations to this solution, an approximate explicit equation for critical size is de-

rived. For five selected values of nondimensional hot-spot and ambient temperatures, the approximate solution predicts critical hot-spot sizes within 7% of the values obtained by exact numerical solutions of the defining nonlinear partial differential equation (Table I). This agreement suggests the applicability of the analysis technique to more complex thermal explosion problems.

FUTURE PLANS

The thermal explosion criterion will next be used to predict the time delay when an explosive is initiated by an imbedded electrically-heated wire. Both direct and time-varying current forms will be investigated.

BACKGROUND

This work was begun to further the application of thermal explosion theory to problems in explosives initiation. The proposed thermal explosion criteria upon which the analysis is based have been presented (Ref. 1) and used (Ref. 2) to find the critical half-widths of slab hot spots. Good agreement with the numerical solutions (Ref. 3) for hot-spot half-width was demonstrated for selected values of the nondimensional hot-spot and ambient temperatures.
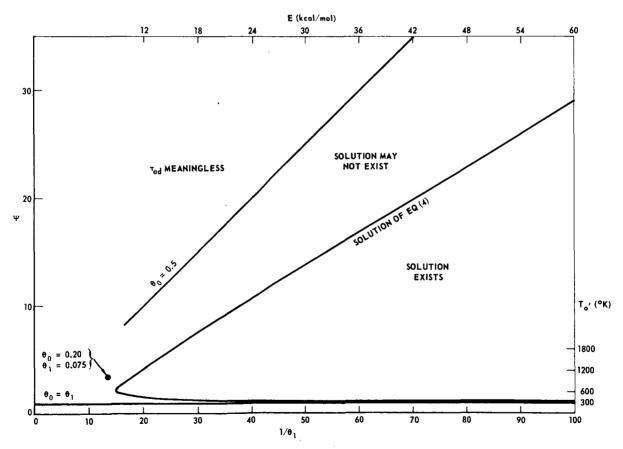

Fig. 1   Limits of Utility of the Solution for Critical Hot Spot Size. (90612)

THE JOHNS HOPKINS UNIVERSITY • APPLIED PHYSICS LABORATORY

UNCLASSIFIED

REVIEW OF STUDIES

The solution for critical hot-spot half-width is given by

$$\alpha_{cr}^2 = \theta^{\circ 2} \exp(1/\theta^\circ)/\tau^\circ, \qquad (1)$$

where θ° and τ° are the solutions of Eqs. (2) and (3):

$$(\theta_0 - \theta_1) \, \text{erf} \, \frac{1}{2\sqrt{\tau^\circ}} + \theta_1 = \theta^\circ \qquad (2)$$

$$-\frac{(\theta_0 - \theta_1)}{2\sqrt{\pi}} \exp\left(-\frac{1}{4\tau^\circ}\right) \tau^{\circ -\frac{1}{2}} = \frac{\theta^{\circ 2}}{2\theta^\circ - 1} \qquad (3)$$

where $\alpha = d(RQZ\rho/Ek)^{\frac{1}{2}}$, $\theta = RT/E$, $\tau = kt/(C\rho d^2)$, d is hot-spot half-width, R is the gas constant, Q is exothermicity, Z is frequency factor, ρ is density, E is activation energy, k is thermal conductivity, T is temperature, t is time, C is heat capacity; and the subscripts cr, 0, and 1 denote the critical, hot-spot, and ambient states, respectively.

In Ref. 2 a sufficient condition for the existence of a solution $(\tau^\circ, \theta^\circ)$ to Eqs. (2) and (3) was noted. Carrying out the required substitutions, this condition is met within the envelope:

$$\psi^2(3.29\theta_1) + \psi(1.06\theta_1 - 1) + (1 - 0.22\theta_1) = 0, \qquad (4)$$

where $\psi = \theta_0/\theta_1$. As T_1 is normally taken to be room temperature, ψ gives the hot-spot temperature directly, independent of E. Figure 1 is a plot of Eq. (4). When $T_1 = 300°K$, the coordinates in Fig. 1 can be replaced by T_0 and E, and these physical values are also presented. As the condition for the existence of a solution is only sufficient, solutions may exist outside the indicated envelope; a case in point is $\theta_0 = 0.20$, $\theta_1 = 0.075$, for which a solution was given in Ref. 2.

It is clear that solutions of Eqs. (2) and (3) can be found everywhere in the range of practical interest.

Although Eqs. (2) and (3) reduce the hot-spot problem to an algebraic one, the computation of the critical parameters must yet be carried out iteratively. However, the algebraic equations can be approximated to permit the derivation of a considerably more instructive explicit equation for critical hot-spot size.

First, approximate the error function in Eq. (2) by

$$\text{erf} \, \frac{1}{2\tau^{\frac{1}{2}}} \cong 1 - 2\tau^{\frac{1}{2}} \exp\left(-\frac{1}{4\tau}\right)/\pi^{\frac{1}{2}}, \qquad (5)$$

good for small τ. Then Eq. (3) and that obtained by substituting (5) into (2) both depend on τ through terms of the form $\tau^n \exp(-1/4\tau)$. Over the τ-range of interest the major part of the variation of these terms with τ is due to the exponential; replace these terms by $\bar{\tau}^n \times \exp(-1/4\tau)$, where $\bar{\tau}$ is an average value of τ near τ°. Then Eqs. (2) and (5) yield

$$\exp\left(-\frac{1}{4\tau^\circ}\right) = \frac{\pi^{\frac{1}{2}}(\theta_0 - \theta^\circ)\bar{\tau}^{-\frac{1}{2}}}{2(\theta_0 - \theta_1)}. \qquad (6)$$

Substituting into Eq. (3),

$$2\theta^{\circ 2}(1 - 2\bar{\tau}) - \theta^\circ(2\theta_0 + 1) + \theta_0 = 0. \qquad (7)$$

Equations (7), (6), and (1) can be combined to give an explicit expression for $\alpha(\theta_0, \theta_1; \bar{\tau})$. A simpler solution is found by linearizing the square root of the discriminant of Eq. (7), to give the approximate solution

$$\theta^\circ = \theta_0 - \frac{\theta_0^2}{2 - 4\bar{\tau}}. \qquad (8)$$

Equations (6) and (1) give

$$\alpha_{cr}^2 = 4\theta^{\circ 2} \exp\left(\frac{1}{\theta^\circ}\right) \ln\left[\left(\frac{\theta_0 - \theta_1}{\theta_0 - \theta^\circ}\right)\left(\frac{4\bar{\tau}}{\pi}\right)^{\frac{1}{2}}\right]. \qquad (9)$$

From Eq. (8), to first order, $\theta^\circ = \theta_0$. Therefore, substitute $\theta^\circ = \theta_0$ everywhere in Eq. (9), except in the denominator of the argument of the logarithm, where Eq. (8) must be used. From the exact solutions in Table I, Ref. 2, a typical value of $\bar{\tau}$ when θ_0 and θ_1 are within the envelope of Fig. 1, is 0.14. Then Eq. (9) becomes

$$\alpha_{cr}^2 = 4\theta_0^2 \exp(1/\theta_0) \ln\left[0.608(\theta_0 - \theta_1)/\theta_0^2\right]. \qquad (10)$$

The values of $\log \alpha_{cr}$ given by Eq. (10) are presented in Table I for comparison with the numerical integration solution (Ref. 3) and the simultaneous solutions of Eqs. (1) through (3). Agreement with the numerical solution is good.

Table I

Computed Critical Hot Spot Sizes

θ_0	0.03	0.04	0.06	0.08	0.10
θ_1	0.02	0.03	0.03	0.03	0.01
$\log \alpha_{cr}$					
Numerical Integration	6.18	4.39	2.82	2.04	1.62
Eqs. (1)-(3)	6.27	4.52	2.92	2.11	1.68
Eq. (10)	6.16	4.39	2.82	2.02	1.59

REFERENCES

1. M. H. Friedman, "Thermal Explosion Analyses," Section III/16b, Research and Development Programs Quarterly Report, July-September 1966, APL/JHU U-RQR/66-3.
2. M. H. Friedman, "Thermal Explosion Analyses," Section III/12b, Research and Development Programs Quarterly Report, October-December 1966, APL/JHU U-RQR/66-4.
3. M. H. Friedman, Ninth Symposium (International) on Combustion, Academic Press, New York, 1963, p. 294.

N67-33379

EXPLOSIVE PROJECTION OF METAL

The purposes of the research program in the explosive projection of metal are: (a) to investigate the effects of geometrical variations in the shape of an explosive device on the direction of projection of the parts of the metal casing, and (b) to study the explosive acceleration of metal and the effect of interposed inert layers between the explosive and the metal. The results will be directly applicable to the solution of problems occurring during the development of guided missile warheads.

In order to investigate the effects of geometrical variations, it is necessary first to develop a system of precise projection. The effort to date has been on this problem.

SUMMARY AND CONCLUSIONS

Two tests were performed at the NOL/WO test facility at Stump Neck, Maryland. In the first, the test device consisted of a 60° pie-shaped sector of explosive Composition C-4 with a line of thirty 1/4-inch steel cubes along the circular face and the remaining sides enclosed in 1/2-inch-thick steel plates. The radius of the sector was 7-3/8 inches. Initiation was at the apex by an Engineers Special Detonating Cap. The target was a 0.050-inch-thick aluminum plate in a circular arc 10 feet from the test device. The target was backed by stacks of Celotex sheets within which the cubes were recovered.

The cube velocity was recorded as 5300 ft/sec. This is less than was expected, probably because of lack of adequate confinement of the explosive charge. The strike pattern on the target was quite regular, indicating high precision of projection. Two-thirds of the steel cubes were recovered. Deformation by the explosive was relatively minor. Deformation caused by target plate impact was large. Impact also caused some spalling.

In the second test the test device consisted of a 60° sector of explosive Composition C-4 with a cylindrical face radius of 3-11/16 inches. A mat of 20 steel rods 1/8-inch square by 4 inches long was placed in an 1/8-inch-thick steel plate curved to conform to the cylindrical face of the explosive. The other sides of the sector of explosive were confined with steel blocks 4 inches thick. A Dupont Detasheet line wave generator was used to provide line initiation of the explosive along the apex of the sector. The target layout was essentially the same as in the previous test except that the plate consisted merely of aluminum foil.

Records of time of flight indicated a rod velocity of 9000 ft/sec. The fragile aluminum foil target sheet was destroyed. However, the Fastax film record indicated that there was a regular strike pattern, although the flashes for each rod were not all straight and continuous. Recovered rod fragments indicated severe breakup. Whether this occurred before impact or in the Celotex is not certain, but it is believed that at least a major fraction occurred in the Celotex.

The recovered rods showed no evidence of spalling. Compressive deformation caused by the explosive was minor. Deformation caused by the Celotex was greater.

It is concluded that the confinement provided in the second test was sufficient to approximate a complete cylindrical warhead. The hand loading of the plastic explosive is a difficult task. Therefore, the homogeneity of the charge may have been poor. This may account for any rod breakup that occurred before impact on the target.

FUTURE PLANS

Arrangements will be made to obtain a cast or pressed charge of suitable explosive. Better instrumentation will be necessary to record the attitude of the rods in flight and rod breakup if any.

DISCUSSION

The problem remains of obtaining an explosive grain of high energy and of very good homogeneity. Pressed or cast charges seem to be the only immediate solution to the problem. The problem of spalling apparently does not occur when adequate confinement of the explosive charge is provided.

RESEARCH AND EXPLORATORY DEVELOPMENT III/20
Adaptive Computing A62CLM
Support: ORD-0621
A. G. Carlton and L. M. Spetner
January–March 1967

N67-33380

ADAPTIVE STABILIZATION COMPUTER

The Adaptive Stabilization Computer program is one of research directed toward development of a computer for predicting ship motion. The prediction will be optimal in the sense that it will tend to minimize the variance of the error and will be based upon measurements of the ship orientation with respect to a stable platform. The computer is intended to automatically adjust its own parameters in order to maintain a prediction at an optimal level under a wide variety of external conditions.

SUMMARY AND CONCLUSIONS

A preliminary analysis of the ship-motion data from David Taylor Model Basin (DTMB) shows that the autocorrelation function of both the roll and the pitch motion can be represented by an exponential cosine. For a random process as simple as this it is possible to estimate the γ's and the η's from estimates of the correlation coefficients of the process. Good estimates of these parameters will allow a flexible prediction capability.

FUTURE PLANS

The 24 sets of ship-motion data from DTMB are currently being fitted to an exponential cosine autocorrelation function. If this simple form is adequate to describe ship motion generally, then greater prediction capability can be achieved than if more general random processes had to be provided for.

An optimal or near optimal technique is being investigated for the sequential estimate of the correlation coefficients of ship-motion random processes. These estimates are viewed as prerequisite to the estimation of γ and η parameters.

DISCUSSION

If the correlation coefficient of a discrete random process is of the form

$$C_n = 3^{-\alpha n}\cos\beta n, \quad n = 0, 1, 2, \ldots,$$

then the process can be described as a simple depth-2 process $\{\xi_n\}$ of the form

$$\xi_n = \gamma_1\xi_{n-1} + \gamma_2\xi_{n-2} + \eta_1\omega_{n-1} + \eta_2\omega_{n-2},$$

where

$$\gamma_1 = 2C_1,$$

$$\gamma_2 = C_2 - 2C_1^2$$

and η_1 and η_2 are found from

$$\eta_1^2 + \eta_2^2 = 1 - \gamma_2^2,$$

$$\eta_1\eta_2 = -\tfrac{1}{2}\gamma_1(1+\gamma_2).$$

Hence from estimates of C_1 and C_2, one can estimate the parameters of the process. These parameters can then be used for prediction.

THE JOHNS HOPKINS UNIVERSITY • APPLIED PHYSICS LABORATORY

N67-33381

WIDEBAND ARRAY ANTENNA SYSTEM

Shipborne antenna systems have been studied with the view of integrating them into a single wideband unit with electronic beam steering. This would save space, weight, and cost without sacrificing the overall system functions in an unfriendly environment.

A phase shifter has been developed for a phased-array antenna system at C-band. This phase shifter, which is of the digital latching type, has a bandwidth well in excess of an octave. A proper disposition of such phase shifters can therefore lead to very wideband phased-array antennas.

SUMMARY AND CONCLUSIONS

A 96-element phased array was previously constructed and evaluated, demonstrating wideband beam steering from 4 to 12 kMc/s. The distortion of the radiation pattern at some frequencies, believed to be caused by the impedance mismatch, was investigated using a matching dielectric sheet at each face of the phase-shifter matrix. In the frequency band where this dielectric sheet presented a reasonable match, the radiation patterns were improved.

Phase shifters assembled in the last report period, using material with a lower magnetic saturation (Trans Tech TT1-1000), were tested. Using this material, the low frequency response was improved by approximately 500 Mc/s, permitting operation from 3 to 12 kMc/s. Figure 1 illustrates the broadband differential phase and insertion loss characteristics of this device. The length of the 4-bit phase shifter will have to be increased by approximately 12 percent to compensate for the reduced differential phase shift caused by lowering the magnetic saturation.

Using the waveguide simulators constructed in the previous report period, the impedance of a simulated infinite array of triangularly spaced elements was measured for the boresight condition over the entire frequency band (3 to 12 kMc/s). An attempt at a wideband impedance match using a double-step dielectric impedance transformer was initiated. Encouraging results (VSWR less than 2 to 1) were obtained over one octave of the frequency band of interest, using an impedance transformer with dielectric constants $\epsilon = 12$ and $\epsilon = 2$, spaced approximately 0.035 inch from the simulated aperture face.

These results are shown in Fig. 2. Methods of optimizing the double-step transformer to cover the
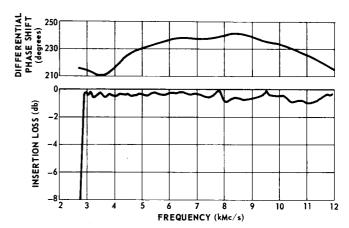

Fig. 1   Wide Band Phase Shifter
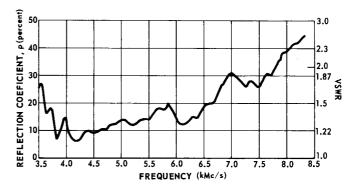TT 1-1000 Ferrite D = 3.20 Inches,
L = 4.850 Inches. (90645)

Fig. 2   Reflection Coefficient (VSWR) of Double
Step Dielectric Transformer ($\epsilon = 2$, $\epsilon = 12$)
in Triangular Array Simulator. (90646)

full-frequency band are presently being explored, and other matching schemes are being investigated. Much work in this area still remains, including the investigation of the impedance variation with scan employing the various impedance matching techniques.

N67-33382

DIRECT SYNTHESIS OF OPTIMAL LINEAR FILTER FROM CONDITIONAL PROBABILITY CONCEPTS

The problem that has been investigated is that of estimating the state of a randomly excited dynamical system from noisy measurements having finite duration. Starting with the Wiener-Hopf equation, Kalman and Bucy (Ref. 1) obtained the optimal filter in the form of a feedback system consisting of a model of the dynamical system in conjunction with a time-varying gain matrix. The gain matrix is obtained from the solution of a matrix Riccati variance equation.

The study described here has resulted in the optimal filter being derived by an entirely different method.

SUMMARY

The conditional probability $p(x/z)$ of a particular state x being present when a measurement sequence z of duration T has been made is maximized with respect to the final state x(T) in order to get the mean that yields the minimum-variance unbiased estimate or best estimate $\hat{x}(T)$. This is termed the Bayes estimate. Expressing it in closed loop form gives the optimal filter.

As a consequence of this approach, the variance equations do not arise, and an explicit expression is obtained for the gain matrix. It is possible to treat random inputs with nonzero means that might not be convenient by the method of Ref. 1. The mean vector enters in a natural manner into the model of the dynamical system in the filter.

The types of problems treated fall naturally into two classes: (1) random inputs to dynamical system, and (2) nonrandom inputs to dynamical system.

Class 1 gives rise to a two-point boundary problem in the calculus of variations. This does not need to be solved explicitly since main interest lies in the end points. The resulting Euler-Lagrange equations are linear and follow simply from the expression for the conditional probability. The gain matrix is a function of the transition matrix of this system of equations.

For Class 2, the maximization can be treated by ordinary calculus and results in a gain matrix expressed in terms of the transition matrix of the original system.

Finally, the same method is applied to obtaining the maximum-likelihood estimate. This estimate is defined as the mean of the conditional probability $p(z/x)$.

The part of the study dealing with Class 2 and the maximum likelihood estimate was completed earlier. It has been discussed briefly in the Quarterly Report, Ref. 2.

The whole study is described in more detail in Ref. 3.
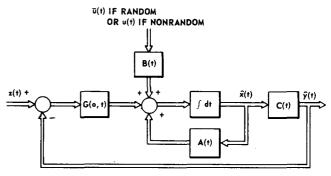
Fig. 1   Optimal Filter.   (90606)

DISCUSSION AND SUMMARY OF RESULTS

Given the nth order linear dynamical system

$$\frac{dx}{dt} = A(t)\, x(t) + B(t)\, u(t), \tag{1}$$

and the measurement

$$z(t) = C(t)\, x(t) + n(t) \tag{2}$$

observed during the interval [o, T], the problem is to design a filter to give the minimum variance unbiased estimate of the state x(T). Denote this estimate as $\hat{x}(T)$.

Class 1: Input u Random, with Mean $\bar{u}$ and Spectral Density Q.

The equation of the optimal filter is:

$$\frac{d\hat{x}}{dt} = A(t)\, \hat{x}(t) + G(o, t)\, [z(t) - C(t)\, \hat{x}(t)] + B(t)\, u(t), \tag{3}$$

where

$$G(o, t) = \{\Theta_{21}(o, t) + \Theta_{22}(o, t)\, A(t) - K_o\, [\Theta_{11}(o, t)$$

$$+ \Theta_{12}(o, t)\, A(t)]\}^{-1}\, [K_o\, \Theta_{12}(o, t)$$

$$- \Theta_{22}(o, t)]\, M(t)\, C'(t)\, N^{-1}(t), \tag{4}$$

and

$$K_o = M_o\, P_o^{-1} + A_o, \qquad M = B\, Q\, B';$$

$(\ )^{-1}$ denotes the inverse, and $(\ )'$ is the transpose.

N is the noise spectral density; P_o is the variance matrix of the initial state x_o

$$\begin{bmatrix} \Theta_{11} & \Theta_{12} \\ \Theta_{21} & \Theta_{22} \end{bmatrix} - \Theta \ ,$$

where Θ is the transition matrix of the $2n^{th}$ order system

$$\ddot{x} - (A - M\dot{M}^{-1} - MA'M^{-1})\dot{x} - (\dot{A} + M\dot{M}^{-1}A + MC'N^{-1}C$$

$$+ MA'M^{-1}A)x + MC'N^{-1}z$$

$$- (\dot{B} + M\dot{M}^{-1}B + MA'M^{-1}B)\bar{u} - B\dot{\bar{u}} = 0 . \qquad (5)$$

Class 2. Input u Deterministic

The equation of the optimal filter is:

$$\frac{d\hat{x}}{dt} = A(t)\hat{x}(t) + G(o,t)[z(t) - C(t)\hat{x}(t)] + B(t)u(t), \qquad (6)$$

where

$$G(o,t) = [\psi'(o,t)P_o^{-1}\psi(o,t)$$

$$+ \int_o^t \psi'(\tau,t)C'(\tau)N^{-1}(\tau)C(\tau)\psi(\tau,t)d\tau]^{-1}C'(t)N^{-1}(t), \qquad (7)$$

or equivalently,

$$G(t,o) = \psi(t,o)[P_o^{-1}$$

$$+ \int_o^t \psi'(\tau,o)C'(\tau)N^{-1}(\tau)C(\tau)\psi(\tau,o)d\tau]^{-1}$$

$$\psi'(t,o)C'(t)N^{-1}(t). \qquad (8)$$

The optimal filter is shown in Fig. 1.

Maximum Likelihood Estimate--The equation of the maximum likelihood filter is:

$$\frac{d\hat{x}}{dt} = A(t)\hat{x}(t) + G(o,t)[z(t) - C(t)\hat{x}(t)] + B(t)u(t) , \qquad (9)$$

where

$$G(o,t) = [\int_o^t \psi'(\tau,t)C'(\tau)N^{-1}(\tau)C(\tau)\psi(\tau,t)d\tau]^{-1}$$

$$C'(t)N^{-1}(t) , \qquad (10)$$

and u is either the deterministic input or equal to the mean $\bar{u}$ if the input is random. In Eq. (9), $\hat{x}(T)$ denotes the maximum likelihood estimate. The maximum likelihood filter also has the form shown in Fig. 1.

FUTURE PLANS

Since the objectives of this study have been attained, no further work is planned at this time.

BACKGROUND

By presenting a different viewpoint on the subject, this study may assist in further development and application of the basic theory. This fits into the objective of the present series of studies, which is the possible application of modern control theory to practical problems.

REFERENCES

1. R. E. Kalman, and R. S. Bucy, "New Results in Linear Filtering and Prediction Theory," Trans. ASME, J. Basic Eng., Vol. 83D, March 1961, pp. 95-108.
2. E. P. Cunningham, "Direct Synthesis of Optimum Filter from Conditional Probability Concepts," Section III/25, Research and Development Programs Quarterly Report, April-June 1966, APL/JHU U-RQR/66-2.
3. E. P. Cunningham, "Direct Design of Optimal Linear Filter from Bayes Estimate," APL/JHU BBD-1538, 31 March 1967.

UNCLASSIFIED

RESEARCH AND EXPLORATORY DEVELOPMENT III/23b
Theoretical Studies Y1MBBD
Support: Task Y/NOw 62-0604-c
E. P. Cunningham
January-March 1967

N67-33383

TRAJECTORY OPTIMIZATION BY STEEPEST ASCENT METHOD

This report deals with the application of the steepest ascent method to two problems in trajectory optimization. It is a continuation of the study described in Ref. 1.

SUMMARY

It is desirable to optimize the fuel-flow rate so that, using a fixed amount of fuel, a missile will attain a given altitude, either (a) in minimum time or (b) with maximum velocity.

The two problems are complementary, and the results should be similar. In both, the best fuel-flow rate decreases from an initial maximum. However, while the final flow rate is almost zero for the minimum time case, it reaches a constant nonzero level for the maximum velocity problem. These results are shown in Fig. 1. The corresponding thrust histories and trajectories are given in Figs. 2 and 3, respectively.

The objective of each program is partly attained by the other; i.e., the minimum time is obtained by increasing the velocity, and maximizing velocity comes from decreasing the time. An undesirable feature of the minimum-time case is that the final thrust goes to zero. For this reason the maximum-velocity program would be a better choice in both cases.

When compared with the constant-flow-rate nominal trajectory, it will be noted that the optimal flow rate in both problems results in a time decrease of 40 to 50%.

Reference 2 gives further details of this study.

FUTURE PLANS

The steepest-ascent method will be compared with other methods for trajectory optimization.

DISCUSSION

The missile equations of motion in two dimensions are

$$\dot{V} = \frac{T-D_o}{m} \cos \alpha - \frac{N}{m} \sin \alpha - g \sin \gamma, \tag{1}$$

$$\dot{\gamma} = \frac{T-D_o}{mV} \sin \alpha + \frac{N}{mV} \cos \alpha - \frac{g}{V} \cos \gamma, \tag{2}$$

$$\dot{h} = V \sin \gamma, \tag{3}$$

$$\dot{x} = V \cos \gamma, \tag{4}$$

$$\dot{m} = -\frac{\dot{w}_p}{g}, \tag{5}$$
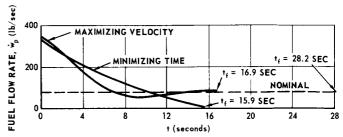
Fig. 1   Fuel Flow Rate for Optimal Trajectories. (90607)
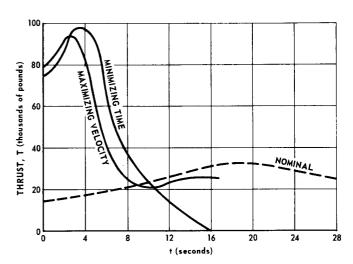
Fig. 2   Thrust History. (90608)

where

thrust $T = \{C + A(h) [-(M - \overline{M}(h))^2 / 2\sigma^2(h)]\} \dot{w}_p - p_a(h) A_{exit}.$

The other symbols are defined in Ref. 1.

The angle of attack α is maintained constant at 4° throughout. The fixed amount of available fuel is taken into account in the form of a constraint on the final missile mass, m.

From arbitrary initial conditions (V = 1500 ft/sec, γ = 30°, h = 2000 feet, x = o, m = 186 slug), a nominal trajectory is generated by integrating the system equations numerically with constant fuel-flow rate ($\dot{w}_p$ = 80 lb/sec). The stopping point (t = t_f) occurs at a certain altitude (h_f = 50,000 feet).

THE JOHNS HOPKINS UNIVERSITY • APPLIED PHYSICS LABORATORY

UNCLASSIFIED

Fig. 3 Optimal Trajectories. (90609)

The adjoint equations are obtained by taking partial derivatives of Eqs. (1) through (5) with respect to V, γ, h, x, and m. The coefficien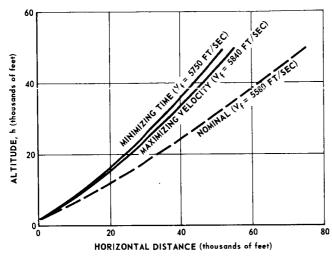ts of the adjoint equations are stored during the forward integration. From known final conditions, these equations are integrated backwards from $t = t_f$ to $t = 0$. The solutions are used to compute the change in fuel flow rate that will bring the final value of missile mass closer to the required final value. Using this new flow rate program,

$$\dot{w}_p = \dot{w}_{p_{NOM}} + \delta \dot{w}_p ,$$

a second forward trajectory is generated. The process is repeated until the terminal constraint is satisfied, and no significant improvement in final time or, alternatively, in final velocity is obtained between successive trajectories.

The motivation for using a fixed amount of fuel rather than as little fuel as possible is that there might be a weight penalty involved in carrying along unburnt fuel to the next stage.

Figure 2 shows that the optimal trajectories are steeper than the nominal and end with a flight path angle of slightly more than 45°. If the next stage were ballistic, the combination of increased velocity and 45° angle would give a marked increase in range as compared with the nominal.

REFERENCES

1. E. P. Cunningham, "Trajectory Optimization by Steepest Ascent Method," Section III/22, Research and Development Programs Quarterly Report, October-December 1966, APL/JHU U-RQR/66-4.

2. E. P. Cunningham, "Optimizing Fuel Flow Rate Program by Steepest Ascent Method," APL/JHU BBD-1540, 10 April 1967.

3. A. E. Bryson and W. F. Denham, "A Steepest Ascent Method for Solving Optimum Programming Problems," J. Appl. Mech., June 1962, pp. 247-257.

RESEARCH AND EXPLORATORY DEVELOPMENT I I I /24b
Research on Supersonic Combustion Z11BHP
Support: NASA (RAP)
F. S. Billig
January–March 1967

SUPERSONIC COMBUSTION (ANALYSIS)

Analytical techniques are being developed to deter-
mine the expected performance of a supersonic com-
bustion ramjet, and to assist in the general understand-
ing of the supersonic combustion process. In this work
the performance characteristics of two types of flow
models, both using the combustion process to assist in
the engine compression, are compared. Both methods
are shown to partially relieve the geometric con-
straints of a fixed-geometry engine required to operate
at different flight Mach numbers.

SUMMARY AND CONCLUSIONS

The two models used in this analysis are shown in
Fig. 1. The two-stream, staged-combustion model
(Fig. 1a) is identical to the model for small secondary
flow discussed in detail in Ref. 1. The "primary" air
in streamtube I is compressed from free-stream condi-
tions, o, to conditions at the end of the inlet d; heat is
added in region d to 4, and the stream is expanded from
4 to 6. In streamtube II (secondary) the compression
from o' to d' is accomplished via the combustion in
streamtube I; combustion in region d' to 4' of stream-
tube II is followed by expansion from 4' to 6'. In the
combustion-shock model (Fig. 1b), air is compressed
in the inlet from o to d; fuel injected at d creates an
oblique compression, which is maintained by the injec-
tion separation and subsequent heat release. Combus-
tion proceeds at either constant or decaying pressure
and is followed by expansion in region 4 to 6. In both
models the kinetic energy efficiency of the compression
process decreases with increasing diffusion.

Typical results at an M_o of 5.0 and a dynamic pres-
sure q_o of 5000 lb/ft^2 are shown in Fig. 2. The curve
for the two-steam model is for the optimum ratio of
the mass flow in streamtube I to that in streamtube II,
which varies from 22 to 36 percent for the range of
contraction ratios shown. The curve for the combustor-
shock model likewise is the result of an optimization.
Each point represents the optimum-strength shock in
combination with the best combustion process. The two
curves are compared with the one-stream case with
shock in the combustor but an optimized one-dimensional
heat-addition process. All curves are terminated at a
total compression static-pressure ratio of ~ 100 [M_d =
1.4]. With this realistic constraint the two-stream
model is better than the combustor-shock model at con-
traction ratios greater than 0.15.

Results for M_o = 10, q_o = 5000 lb/ft^2 are shown in
Fig. 3. Sets of curves (solid) for equilibrium and
(dashed) for frozen nozzle expansions are shown. Dif-
ferences between the combustor-shock model (B, B')
and two-stream model (C, C') are less because it is
necessary to have a less optimized heat addition process
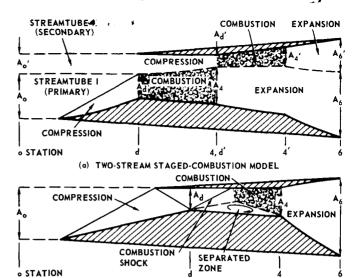
Fig. 1   Models for Thermal Compression Analysis, (90619)
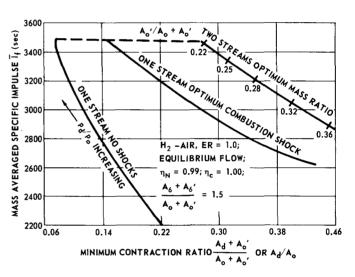
Fig. 2   Comparison of Thermal Compression Models on
Scramjet Performance at Mach 5. (90620)

in the latter case. These sets of curves should be com-
pared with the optimum one-stream, no-thermal-com-
pression case (A, A'). Curve A is a constant-area
process; curve A' is constant-area for A_d/A_o > 0.042
and is close to constant-pressure at lower A_d/A_o.

Starting considerations for a typical ramjet might
limit the minimum A_d/A_o to 0.12. For equilibrium flow
at M_o = 10, the combustor-shock model results in a
gain of 10.5 percent in $\bar{I}_f$, and the two-stream model
in a gain of 10.7 percent compared to one stream with
no thermal compression.

FUTURE PLANS

Similar calculations will be made at different flight
conditions and equivalence ratios (ER) and for various
component efficiencies to test the sensitivity of the re-
sults to these effects. Available experimental data will

Fig. 3 Comparison of Thermal Compression Models on Scramjet Performance at Mach 10. (90621)

$$\eta_{ke}\% = 100 - \Delta u - 0.2\Delta u^2, \qquad (1)$$

where $\Delta u = (u_o - u_d)$ is the inlet velocity decrement in thousands of ft/sec, or

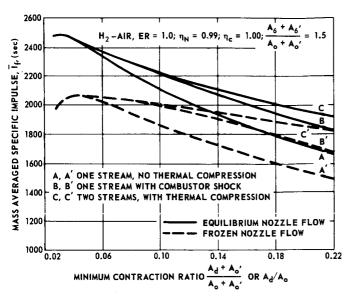$$\eta_{ke}\% = 100 - 20\left(1 - \frac{M_d}{M_o}\right)^5 . \qquad (2)$$

The two expressions give nearly identical η_{ke} values for all reasonable compression ratios. Equation (2) was used in this analysis. In the one-stream combustor shock model, the additional shock loss was taken into account.

For the combustion process the general family of one-dimensional heat addition processes following the relationship $pA^{\epsilon/\epsilon-1}$ = constant (Ref. 4) was used. For each case, values of ϵ were selected that maximized $\overline{I}_f$ with the constraint that $A_4 \geq A_d$ for all models. For the combustor-shock model the optimization is somewhat more subtle; for a given A_d/A_o, increasing the shock strength increases the shock loss but at the same time lowers the average Mach number in the combustion process, thus reducing the combustion loss.

The effect of the change on the η_{ke} assumption from the results of Ref. 1 is not too significant. This is a consequence of the fact that for a given A_d/A_o, increasing η_{ke} increases M_d so that inlet improvement is mitigated by increased combustor loss. At an M_o of 5, the losses balance; at an M_o of 10, the inlet loss is relatively more important, so for values of $M_d > 3.2$, $(A_d/A_o = 0.029, \eta_{ke} = 0.97$ (from Eq. 1)), the $\overline{I}_f$ values are higher than in Ref. 1. With this plausible variation in η_{ke}, the optimum contraction ratio at Mach 10 represents less than the maximum possible contraction. For equilibrium flow, the maximum occurs at $M_d = 3.2$ and for frozen flow at $M_d = 4.2$.

Both thermal compression models lead to improvement in $\overline{I}_f$. The two-stream case is somewhat better, but the difference between the two is significant only at large values of A_d/A_o, which would be associated with an engine design compromised to operate at low M_o. However, the combustor-shock model has the added virtue of being directly considered as a dual mode subsonic-supersonic combustion engine simply by increasing the shock strength to a normal shock.

be examined to ascertain whether, and to what extent, the beneficial effects of thermal compression have been realized.

BACKGROUND

Previous analysis (e.g., Ref. 2) of the expected performance of the supersonic combustion cycle have shown the desirability of decreasing the ratio of combustor inlet area to engine inlet area as M_o increases, and at the same time decreasing the combustor exit to combustor inlet area ratio as M_o increases and/or ER decreases. If variable geometry hardware cannot be used, then it becomes of interest to investigate fluid mechanical techniques for obtaining effective variable area processes. In Ref. 1 the two-stream model was introduced, and results were obtained for a constant-inlet kinetic energy efficiency, η_{ke}, of 0.97. The shock in the combustor model, again based on a constant η_{ke}, was discussed Ref. 3. The intent in this study was to compare the two methods on an equivalent basis and use a more realistic assumption on inlet efficiency.

DISCUSSION

The total pressure recovery of a typical hypersonic-supersonic inlet will decrease with increasing Mach number and amount of compression. The previously used assumption of a constant η_{ke} gives a reasonable M_o dependence, but it does not account for the degree of compression. To obtain a more realistic assumption on η_{ke}, inlet calculations were made for the M_o range of 4 to 14 and altitude range of 0 to 150,000 feet, based on the assumption that the compression was attained via an optimized set of four oblique waves. The results could be very adequately collapsed by either of the following expressions:

REFERENCES

1. F. S. Billig, "Supersonic Combustion Analysis," Section III/23, Research and Development Programs Quarterly Report, October-December 1966, APL/JHU U-RQR/66-4 (also reported in AQR/66-4).
2. Z. H. Landau and W. A. Yeneriz, Parametric Supersonic Combustion Ramjet Engine Optimization, Douglas Missile and Space Systems Division Paper No. 3262, July 1965.
3. F. S. Billig and S. E. Grenleski, Combustor Development for a Liquid-Fueled Supersonic Combustion Ramjet Missile (U) (Confidential), APL/JHU TG-697, June 1965
4. A Martellucci, E. Rush, and J. Johnson, "Inlet Design and Development for Low Speed Range Scramjet Engines" (U) (Confidential), AIAA Second Propulsion Joint Specialists Conference, June 1966 (to be published by U. S. Air Force).

TURBULENT MIXING (ANALYSIS)

The objectives of this study are the determination of a suitable model for the eddy viscosity and the development of accurate approximate methods of solution for the differential equations of motion so that simple, reliable predictions of free turbulent mixing processes can be obtained. This work is important in the design of a scramjet engine as it will aid in the determination of the required length and the optimum shape of the combustor.

SUMMARY AND CONCLUSIONS

A new analytical treatment of free mixing problems is proposed and developed. The principal difference between past work (see classical models, Fig. 1) and this work is the relaxation of the restrictive assumption of flow similarity. A typical actual flow field, showing velocity defect regions owing to boundary layers and finite splitter plate thickness, is depicted in Fig. 2. The present analysis of the real situation does not assume similarity of flow profiles.

The theoretical prediction is compared with some experimental data in Fig. 3 for two options in the theory (see DISCUSSION). The dashed curve shows the best agreement in the near field ($0 \le x \le 100a$), but the far-field trend is at some variance with the data. The dash-dot curve is to be preferred as it is in good agreement throughout. Also shown on the figure is the classical similarity theory of Abramovich (Ref. 1); it can be seen that the new approach is more accurate.
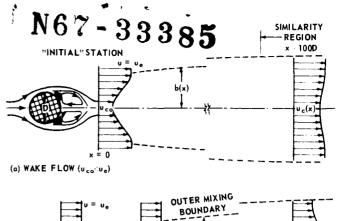
FUTURE PLANS

Comparisons of theoretical predictions and experimental data for axisymmetric, compressible, and foreign gas injection problems will be made and assessed.

BACKGROUND

The classical treatment (Refs. 1 and 2) of free mixing problems is based on a view of the flow field shown schematically in either Fig. 1a or 1b for "wake" or "jet" mixing problems respectively. There are, in general, two main regions of the flow, the transitional or developing region, and the similarity region, where suitably scaled profiles are self-preserving with axial distance. In the jet case an initial region containing the potential core precedes the transitional region. The mixing in the initial region is normally taken as that for the well-known half-jet problem (two unbounded parallel streams of different velocity initially separated by an infinitesimally thin plate). When the inner boundary of this mixing region intersects the axis of the jet, the initial region is deemed ended and the next stage in the calculation must begin. At this point, however, a

N67-33385

(a) WAKE FLOW ($u_{co} < u_e$)

(b) JET FLOW ($u_j > u_e$)
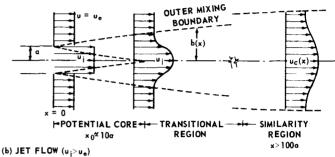
Fig. 1 Schematic of Flow Field for Classical Mixing Theories. (90616)
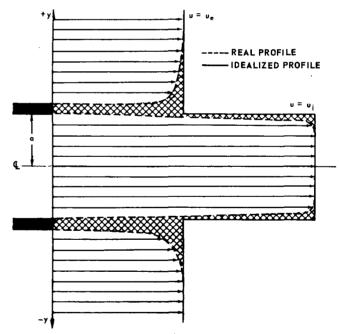
Fig. 2 Typical Actual Initial Profile for Two-Dimensional Jet Mixing under Laboratory Conditions from Ref. 3. (90617)

very crude assumption is made. Namely, the transitional region is neglected and the similarity region is assumed to begin immediately. For wake problems, of course, one does not normally treat an initial region (the near wake) directly, but the same assumption of neglecting the transitional region and taking similar profiles immediately, now at the "initial" station, is commonly made.

Fig. 3 Comparison of Theory and Experiment for Low Speed, Planar Jet Mixing, $u_j/u_e = 2.0$. (90618)

This general procedure is open to severe criticism on two counts. First, the flow in the initial region is not well represented by the idealized half-jet problem since real initial profiles are far from ideal. Figure 2 shows the initial profile obtained in a careful laboratory jet mixing experiment (Ref. 3). Shown also for comparison is an idealized profile as well as the defect between the ideal and actual profiles indicated as a cross-hatched area. A defect of this size caused by external boundary layers and finite splitter plate thickness has a dramatic effect on the near mixing field, as shown in Ref. 4; this manifests itself in the generally poor prediction of the length of the initial region by the classical theories (Ref. 2). Second, it is well known that the similarity region does not begin near the end of the initial region. Townsend (Ref. 5) indicates, for example, that the wake behind a circular cylinder does not become similar until at an axial distance greater than ≈ 100 diameters. These two criticisms are not merely academic; the result of the crude assumptions made in the classical treatments is rather poor agreement between theory and experiment. A typical comparison is given in Fig. 3, using some data from Ref. 3 and theory from Ref. 2.
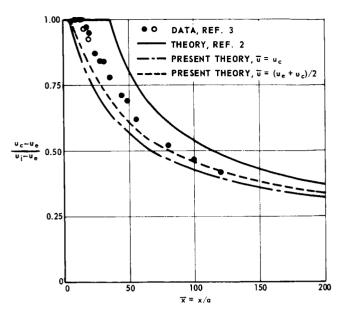
DISCUSSION

In view of the situation above, it appears advantageous to attempt to develop simple, approximate analyses that do not assume flow similarity in the near field.

Most technological applications of jet problems (e.g. fuel mixing) are mainly concerned with the development of the mixing region over long distances so that the details of the initial region are of secondary importance. Add to this the fact that the details of the initial profile (boundary layer and splitter plate thickness) must be

treated to provide a reasonable description of the initial region, and it appears that a simplification in this region is in order. Therefore, the eddy viscosity ϵ in this region has been taken as related to the gross profile rather than the thin mixing region emanating from the splitter plate. This assumption is not necessary for wake problems.

The major feature of the present work is that similarity of profiles is not assumed. The full nonsimilar problem is treated directly by using a linearization in the von Mises plane (the x, ψ plane, where x is axial distance and ψ is the stream function); i. e., the boundary layer momentum equation,

$$\frac{\partial g}{\partial x} = \epsilon u \frac{\partial^2 g}{\partial \psi^2} , \qquad (1)$$

is approximated as:

$$\frac{\partial g}{\partial x} = \epsilon(x) u(x) \frac{\partial^2 g}{\partial \psi^2} , \qquad (2)$$

where $g(x, \psi) \equiv P(x) + \rho u^2/2$, ρ is density and u is velocity. (See Ref. 6 for a detailed description of the linearization.) Two choices for the linearizing velocity, $\bar{u}(x)$, have been used: (a) $\bar{u}(x) = u_c(x)$, and (b) $\bar{u}(x) = (u_e + u_c(x))/2$, where subscripts e and c designate free-stream and centerline conditions, respectively.

With the assumption on the eddy viscosity in the initial region described above, a single form for the eddy viscosity model can be applied throughout the flow. Here we have used

$$\epsilon(x) = 0.018 u_e \bar{\delta}^* , \qquad (3)$$

where

$$\bar{\delta}^* \equiv \int_{-\infty}^{\infty} (1 - \frac{u}{u_e}) dy . \qquad (4)$$

This has been shown (Ref. 7) to be equivalent to the classical Prandtl model and is an obvious extension of Clauser's boundary layer model.

REFERENCES

1. G. N. Abramovich, The Theory of Turbulent Jets, The MIT Press, Cambridge, Mass., Part I, 1963.
2. H. Schlicting, Boundary Layer Theory, McGraw-Hill Book Co., New York, Fourth Edition, Chapter XXIII, 1962.
3. A. S. Weinstein, J. F. Osterle, and W. Forstall, "Momentum Diffusion from A Slot Jet into a Moving Secondary," J. Appl. Mech., September 1956, pp. 437-443.
4. J. A. Schetz and S. Favin, "The Ignition of Slot Injected Gaseous Hydrogen in a Supersonic Air Stream," AIAA Propulsion Meeting, Colorado Springs, Colorado, Paper No. 66-644, June 1966.
5. A. A. Townsend, The Structure of Turbulent Shear Flow, Cambridge University Press, Ch. 7, 1956.
6. J. A. Schetz and J. Jannone, "A Study of Linearized Approximations to the Boundary Layer Equations," J. Appl. Mech., December 1965.
7. J. A. Schetz and J. Jannone, "Planar Free Turbulent Mixing with a Axial Pressure Gradient," ASME Fluids Energy Conference, Chicago, Ill., May 1967.

RESEARCH AND EXPLORATORY DEVELOPMENT I I I/24d
Research on Supersonic Combustion Z11BHP
Support: NASA Headquarters (RAP)
C. L. Yates, M. Lasky, and J. A. Schetz
January–March 1967

TWO-DIMENSIONAL MIXING STUDIES

Among the possibilities for fuel injection into the supersonic combustors of Scramjet engines is that of injecting the fuel downstream and adjacent to the combustor wall. Downstream injection is of particular interest at high flight speeds because the added momentum of the fuel increases engine thrust (satisfactory mixing and combustion is still required). Experimental and theoretical studies of the turbulent mixing process (with and without combustion) are being undertaken to deduce scaling laws pertaining to mixing, heat transfer, and skin friction that can be used in combustor design.

SUMMARY

Further progress has been made in the development of the wall-slot injection problem (Fig. 1) based on a two-layer model of the velocity field. It was previously demonstrated (Ref. 1) that the use of this model, together with a linearized treatment of the boundary layer momentum equation solved by a similarity technique, leads to an accurate description of the incompressible, turbulent, flat-plate boundary layer. Before attacking the wall injection problem, it is necessary to develop a technique for streamwise integration of the boundary layer equations starting with arbitrary, nonuniform, initial velocity distributions. This initial-value procedure has now been defined and programmed for machine computation. Application was first made to the flat-plate boundary layer to permit comparison with previous calculations (Ref. 1). Figure 2 shows the calculated axial development of displacement thickness Reynolds number, R_δ^*, and skin friction coefficient, C_f, compared with previous results that were obtained independently of the streamwise coordinate origin. Numerical stability considerations (see Discussion) required an expanding step-size in the integration procedure, and the effects of changing the initial step-size are shown in these results. The results are given in terms of a normalized, transformed axial coordinate, $\tilde{\xi}$; and, for a thousand-fold increase in $\tilde{\xi}$, the maximum differences between the two sets of calculations are ~ 3% in R_δ^* and ~ 1% in C_f. Furthermore, the skin friction law, C_f versus R_δ^*, is almost identical in both cases. Assuming ambient air at 500 ft/sec on a plate, these results cover the region of 0.25 to 10 feet. Thus, good agreement has been obtained over a significant axial distance.

Several checkout runs were made with the experimental model, and the equipment and instrumentation performed satisfactorily except for minor difficulties to be described. Figure 3 is a schlieren photograph of the model flow field that also shows pitot and cone-static pressures probes mounted in the stream. The two points of interest in Fig. 3 are: the weak shock generated within the nozzle, caused by a local fault in the nozzle contour; and the strong shock ahead of the probes caused by flow choking between the probes that are mounted with centerlines 1-inch apart. (The shock originating at the injector lip is caused by a mismatch of static pressures at that point, a condition that is eliminated
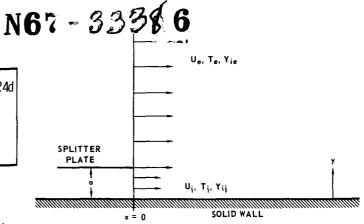
Fig. 1   Schematic Representation of Wall Slot Injection Flow Field. (90767)
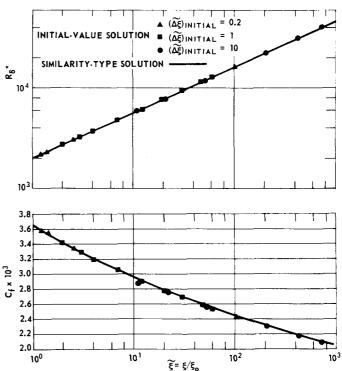
Fig. 2   Effect of Solution Technique on Computed Boundary Layer Characteristics, (a) Comparison of Reynolds Number Distribution, (b) Comparison of Skin Friction Coefficient Distribution. (90768)
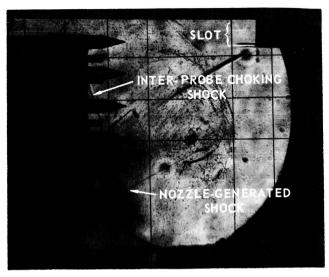
during normal testing.) These two features of the flow field will be corrected before testing is resumed.

FUTURE PLANS

The correct formulation of the "law of the wall" shear distributions (Ref. 1) will be included in the analysis, which will then be applied to incompressible, wall-slot injection and the results compared with existing experimental data. Having completed this, the analysis will be modified to handle compressible flows. Necessary modifications to the experimental model and instrumentation will be made and testing resumed.

BACKGROUND

The analytical method being developed to determine the velocity field for the wall-slot injection problem (Fig. 1) is based on a two-layer model. The inner layer is assumed to be described by the "law of the wall," which has been shown to be valid for a variety of flow situations; e. g., channel, pipe, and boundary layer

Fig. 3   Schlieren Photograph of Mixing Model Flow Field. (90769)

flows, with and without pressure gradient. In the outer layer the eddy viscosity is assumed to vary only in the axial direction, an assumption frequently used in "wake" and "free" jet-flow solutions. Hence, the outer layer can be treated as a laminar-like flow, with a finite, "wall-slip" velocity. This model was shown by Clauser (Ref. 2) to describe adequately the incompressible, turbulent, flat-plate boundary layer. Clauser determined the outer velocity profile by using the exact, nonlinear, partial differential momentum equation of the boundary layer, which, by a similarity-type of transformation, was reduced to an ordinary differential equation.

To use this model in the wall-slot injection case requires a definition of the outer profile at desired downstream positions for an arbitrary, nonuniform, initial velocity distribution. The similarity technique is no longer useful since the solution at any point now depends on all previous upstream development. Furthermore, solution of this mixed, initial-value-boundary-value problem using the exact, nonlinear, boundary-layer momentum equation is possible only with numerical techniques. For simplicity, a linearized version of the equation is being explored.

DISCUSSION

Reference 1 shows the results of applying a linearized treatment of the two-layer flow model to the incompressible, turbulent, flat-plate boundary layer. It was possible in that case to express the outer velocity as

$$\widetilde{u} = \widetilde{u}_o + (1-\widetilde{u}_o)\ \mathrm{erf}\ (\eta)\ , \qquad (1)$$

where: $\widetilde{u}$ = nondimensional velocity referenced to free-stream velocity

$\widetilde{u}_o$ = nondimensional, wall-slip velocity

$\eta \equiv \frac{1}{2}\ \dfrac{y}{\xi^{\frac{1}{2}}}$, the similarity variable

ξ = transformed axial coordinate.

The important point is that the outer profile in the similarity type of plane can be immediately defined for any arbitrary value of $\widetilde{u}_o$, thus permitting a relatively simple application of the required two-layer matching procedure.

It is possible to assign arbitrarily an axial coordinate to the results obtained with Eq. (1) by setting the ratio of free-stream velocity to kinematic viscosity, u_e/ν, which in turn sets the corresponding value of ξ. This flow problem can then be formulated as an initial-value problem since an initial profile (Eq. 1) and other required initial conditions can be established at some point, ξ_o. When this is done, the solution of the outer profile is obtained as

$$\widetilde{u}\ (\xi', y) = \widetilde{u}_{oo}\ \mathrm{erf}\ \left[\frac{y}{(4\xi')^{\frac{1}{2}}}\right] + (1-\widetilde{u}_{oo})\ \mathrm{erf}\ \left\{\frac{y}{[4(\xi_o+\xi')]^{\frac{1}{2}}}\right\}$$
$$+ \frac{y}{(4\pi)^{\frac{1}{2}}}\ \int_o^{\xi'} \frac{\widetilde{u}_o(\lambda)\ e^{\frac{-y^2}{4(\xi'-\lambda)}}}{(\xi'-\lambda)^{\frac{3}{2}}}\ d\lambda\ , \qquad (2)$$

where: $\widetilde{u}_{oo} = \widetilde{u}_o$ evaluated at ξ_o

$\xi' = \xi - \xi_o.$

The important feature of this equation is contained in the integral term, which shows that the solution at a downstream position depends upon the complete previous history of $\widetilde{u}_o$, an unknown parameter. Computation with Eq. (2) requires step-wise integration, which is difficult to perform, even conceptually, by numerical techniques because of the behavior of the integrand weighting function. The weighting function, under some conditions, is sharply peaked at a value of ξ' between tabular points, which can lead to error in the evaluation of the integral. This difficulty was avoided by assuming a linear variation of $\widetilde{u}_o(\lambda)$ between steps and evaluating the integral analytically.

A numerical stability problem was encountered in the matching computations when the change in match quantities from step to step became small compared with the (machine-limited) tolerance required to match these quantities at a given step. This problem was solved by using an expanding step size in such a way that significant variation from step to step is assured. The results of these computations are shown in Fig. 2, where a few computed points, the first, second, and last points included, for three initial step sizes are compared with results obtained by similarity solution. The figure shows the tendency of the first two computed points, especially for the larger initial-$\Delta\widetilde{\xi}$ case, to oscillate about an average curve defined by succeeding points. This oscillation is apparently due to the $\widetilde{u}_o$ approximation, which became more valid in the downstream direction since the rate of change of u_o with ξ' decreased. Accordingly, calculations with the smaller initial step size more nearly reproduce the similarity solution at small ξ'. As the solution proceeds downstream, results obtained with various initial $\Delta\widetilde{\xi}$'s tend to approach one another as expected since the steps are expanding to nearly equal size, and the outer velocity profile is only mildly affected by solutions far upstream. Consequently, average curves can be drawn which, neglecting the first two points in a series, closely approximate all points. These encouraging results justify further development of the linearized treatment of the assumed model.

REFERENCES

1.   C. L. Yates, M. Lasky and J. A. Schetz, "Two Dimensional Mixing Studies," Section III/26b, Research and Development Programs Quarterly Report, July-September 1966, APL/JHU U-RQR/ 66-3 (also in AQR/66-3).

2.   F. H. Clauser, "The Turbulent Boundary Layer," Advances in Applied Mechanics, Vol. IV, Academic Press, New York, 1956, pp. 2-51.

Section V

FUNDAMENTAL RESEARCH

APL Analyses

APL is conducting a research program to determine the effectiveness of radar for detecting clear-air turbulence. Experiments and analysis this quarter were concerned with an attempt to confirm that birds were the source of some of the dot angles and to determine whether the radar return from known, single birds in flight contained any recognizable radar signature by which they could be identified (V/1).

Plasma Dynamics

In the work on beam-plasma interactions work has been carried out in two areas. The first involves an improvement in the dispersion relation describing the waves in the actual experiment; the second is that of nonlinear effects in the beam-plasma experiment. Measurements have been made of harmonic generation, the behavior of the harmonics in space, and the frequency spectrum of the waves (V/2a).

The flow of ionized gas and its interaction with magnetic fields are basic areas of plasma research. In the research program specifically concerned with the behavior of a plasma in a magnetic transfer field, two particular magnetic geometries are being evaluated; one is a solenoid field and the other is a multipole field that forms a magnetic channel (V/2b).

Experiments are being conducted in the excitation of instabilities in semiconductor plasmas, and the associated microwave radiation is being studied. Work has continued on the excitation of instabilities and microwave emission from high purity n-type indium antimonide. The emission spectrum has also been studied, using specimens mounted axially in cylindrical waveguide in both transverse and longitudinal magnetic fields (V/2c).

UNCLASSIFIED

FUNDAMENTAL RESEARCH V/1
APL Analyses W01BPD
Support: Air Force Cambridge Research
          Laboratory/NASA
T. G. Konrad, J. J. Hicks, and E. B. Dobson
January-March 1967

RADAR CHARACTERISTICS OF KNOWN, SINGLE BIRDS IN FLIGHT

The Applied Physics Laboratory is conducting a re-
search program to determine the effectiveness of radar
for detecting clear-air turbulence. In this connection
identification of the source of radar returns is of prime
importance so that returns from other than clear-air
targets, e.g. birds, insects, clouds, etc., may be dis-
tinguished from returns that are caused by truly clear-
air phenomena. The identification of the so-called "dot
angels," i.e., radar returns from unknown point targets,
has been, and continues to be, a subject of much study
and conjecture. There is no doubt that radar returns
from birds and insects account for many of the observed
dot angel returns. If the character of the radar returns
from various classes of targets had characteristically
different and recognizable radar signatures, then the
radar operator could identify, in real-time, the source
of the return and concentrate on those from clear-air
structures, our principal interest.

The primary purpose of the experiments and analy-
sis reported herein was not to study birds as such, but
to confirm that birds were the source of some of the dot
angels and to determine whether the radar return from
known, single birds in flight contained any recognizable
radar signature by which they could be identified.

SUMMARY AND CONCLUSIONS

A series of experiments was performed at the Joint
Air Force - NASA (JAFNA) radar facility at Wallops
Island, Virginia, wherein known species of birds were
ejected individually from an aircraft and the returned
radar signal from the bird and its position were re-
corded. Three species of birds were used in the experi-
ments; the Boat-tailed Grackle (Carsidix mexicanus),
the House or English Sparrow (Passer domesticus) and
the Homing Pigeon (Columbia livia).

A bird in flight is a complex target and produces a
highly fluctuating radar return. As such the radar
cross section should be described in terms of its sta-
tistical properties. There was no recognizable wave-
length dependence to the radar cross sections since, in
general, the birds fall in the "Mie" or resonant region.

The radar return does, however, contain a radar
signature that provides a basis for identifying an un-
known point target as a bird. This signature is com-
posed of the radar cross-section, the probability dis-
tribution of the cross-section, and the content of the
fluctuation or energy spectrum. The radar cross-
section (or power received) of a single bird in flight is
log-normally distributed. The characterizing parame-
ter is the mean-to-median ratio of cross-section, which
represents a measure of the amount of fluctuation in the
returned signal. This ratio, in turn, is a function of
the size of the bird relative to the radar wavelength.

THE JOHNS HOPKINS UNIVERSITY • APPLIED PHYSICS LABORATORY

UNCLASSIFIED

Fig. 1 Cumulative Probability Distribution of Radar
Cross Section at S-Band. (90687)

The approximate size of the bird may, therefore, be
estimated by examining the fluctuation characteristics,
that is, the mean-to-median ratio.

Another facet of the radar signature of birds is the
shape of the fluctuation or energy spectrum. The
spectrum contains peaks that indicate periodic, rela-
tive motion within the target, i. e. the bird's wingbeat.

Thus, the radar return from single birds in flight
is characteristically different from other possible
sources of point or dot target returns such as aircraft,
swarms of insects, several birds together, small clouds,
or meteorological structures.

FUTURE PLANS

No further work in connection with radar returns
from birds is planned. The objectives of the experi-
ments and analysis have been fully met.

DISCUSSION

Briefly, the JAFNA, Wallops Island radar complex
consists of three radars, X-band (3.2 cm), S-band
(10.2 cm), and UHF (71.5 cm). The S-band radar is a
monopulse tracking radar with the X-band and UHF an-
tenna slaved to the S-band.

The birds were placed in individual containers and
taken by airplane to a drop altitude. The radars tracked
the aircraft to the drop zone and at the moment of bird
ejection, the track was stopped and the beam fixed on
the drop zone. The separation of bird and aircraft was
easily detected; when the two targets had separated suf-
ficiently, the radars were set to track the bird auto-
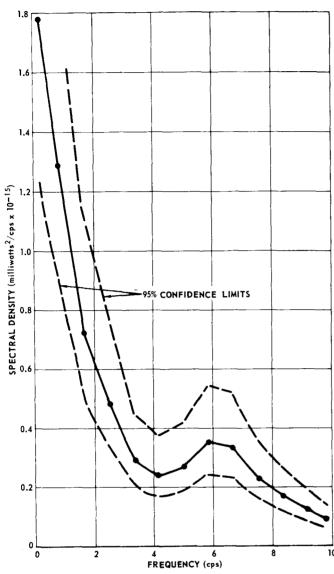matically.

Fig. 2 Power Spectrum of Young Male Grackle Test 631-1, X-Band. (90688)

Table I

Bird Cross-Sections at Three Radar Wavelengths

Bird	Radar	Cross-Section	
		Mean (cm^2)	Median (cm^2)
Grackle	X	15	7
	S	25	11
	U	0.6	0.4
Sparrow	X	1.5	0.8
	S	13	11
	U	0.02	0.02
Pigeon	X	15	6
	S	80	32
	U	11	8

The received radar signal fluctuated considerably, at times over two orders of magnitude. The mean radar cross-section is generally related to the bird size and shape. These are constant for a given bird. The fluctuations in the cross section (or radar signal intensity) are a result of changes in the orientation of the body, wing motion, head motion, etc. during the flight. The radar cross-section, therefore, cannot be described by a single value but must be represented in statistical terms, that is in terms of the mean, the median, the probability distribution, and the fluctuation or energy spectrum of the cross section.

The mean and median cross sections for each bird target at each of the three radar wavelengths was calculated, using data recorded at one point per second throughout each flight. These are shown in Table I.

The mean and median cross sections for a given sized bird do not exhibit a recognizable wavelength dependence since the dimensions of the birds fall in the "Mie" region in which the scattering cross section of a target of given size oscillates about some mean value with changes in wavelength.

The cumulative probability distribution of the radar cross section was also calculated. The distributions were then compared with known distributions such as the gaussian, Rayleigh, and exponential. Typically the calculated distributions were characterized by large dynamic ranges and variances and appear to follow a log-normal distribution. The cumulative probability distributions for all bird targets at S-band are shown in Fig. 1. The analysis of Ref. 1 shows that the slope of the curve, expressed in terms of the mean-to-median cross section ratio, is a function of the size of the bird relative to the radar wavelength. The approximate physical size of the bird may, therefore, be estimated by examining the fluctuation characteristics, that is, the mean-to-median ratio of the radar cross section.

A typical example of the fluctuation or energy spectrum of a bird in flight is shown in Fig. 2. The spectrum for targets made up of many independent scatterers in motion is broad and has a single peak at zero frequency. Targets that have periodic, relative motion, such as a wingbeat in the case of a bird or rotor motion in the case of a helicopter, will produce spectra that contain peaks at higher frequencies. This presumes that the wavelength is small relative to that part of the target that is producing the periodic, relative motion so that the radar return contains fluctuations caused by such motion. In general, the spectra at X- and S-band exhibit peaks at the higher frequencies that are related to the wingbeat.

REFERENCE

1. T. G. Konrad, J. J. Hicks, and E. B. Dobson, "Radar Characteristics of Known, Single Birds in Flight," APL/JHU BPD67U-5.

BEAM-PLASMA INTERACTIONS

A stream of charged particles flowing through a plasma may excite coherent, growing waves in the plasma under proper conditions of density, stream velocity, and magnetic field strength. Experiments and theoretical work have been conducted that illustrate the dependence of the wavelength, frequency, and growth rates of the waves upon the parameters given above. These measurements have been confined to the regions wherein the linear theory was considered valid, i. e., where simple exponential growth of the wave was observed (Ref. 1).

SUMMARY

Work during the present two quarters has been carried on in two areas. The first involves an improvement in the dispersion relation describing the waves in the actual experiment, and uses a computer program devised by Simpson (Ref. 2) for finding the complex eigenvalues of the dispersion equation. The second area is that of nonlinear effects in the beam-plasma experiment. Measurements have been made of harmonic generation, the behavior of the harmonics in space, and the frequency spectrum of the waves. The latter resembles the spectrum predicted by plasma turbulence theory (Ref. 3). In addition, the saturation of the spatially growing waves has been investigated as a function of beam voltage.

FUTURE PLANS

Parametric measurements of the nonlinear effects will be continued in an effort to trace the evolution of wave energy from the form of discrete, coherent oscillations into a highly turbulent, noncoherent spectrum. Attempts will be made to determine the kinetic energy flow from electrons to ions through spectroscopic observations of the optical emission.

DISCUSSION

Two improvements were made in the instrumentation used during this period. First, a resonant cavity for measuring electron density was installed immediately in front of the electron gun so as to give the density in the interaction region directly. In general, the density is lower by 20 to 30% than that measured upstream by the original cavity (Ref. 1).

The second improvement was the installation of a phase-coherent synchronous detector and an X-Y plotter to record the pulsed, microsecond UHF signals in a DC fashion. This greatly increases the data rate and ease of operation, especially at very low signal levels.

Fig. 1   Harmonic Structure of Spatially Growing Waves. (90664)
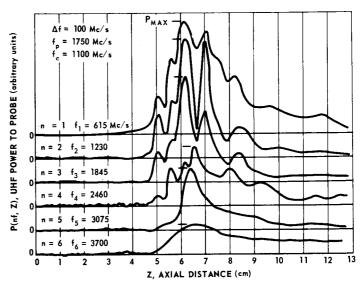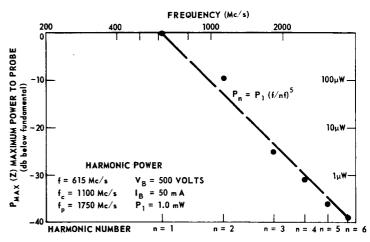

Fig. 2   Maximum Power Level, P_{max}. (90665)

Using this last technique, the harmonic structure of the spatially growing waves was found and is illustrated in Fig. 1. These are plots of UHF power (in arbitrary units) to a traveling probe as a function of axial distance (the electron gun is at z = 0). The power is that observed in a 100 Mc /s band centered at the

frequencies f_1, f_2..., f_6; the origins have been displaced for clarity. A clear standing wave structure is seen, and all of the harmonics have maxima in the same region of space.

Figure 2 is a plot of the maximum power level, P_{max}, for each harmonic, from Fig. 1 as a function of frequency, or harmonic number n. The detected power level of the fundamental is $P_1 \simeq 1$ mw, and the spectrum goes as

$$P_n = P_1 n^{-5}.$$

From the theory of weak plasma turbulence (Ref. 3), one expects the electric field spectrum as a function of wave number k to behave as

$$E_k = Ak^{-5/2}.$$

Since the waves at the peak power point are apparently mildly turbulent, and since they all have a common phase velocity ω_k/k approximately equal to the beam velocity v_b, the power spectrum of these waves may be expected to behave as

$$P(\omega_k) = B\left|E_k\right|^2 = D\omega_k^{-5}.$$

This is the behavior observed, since for this discrete spectrum,

$$\omega_k = 2\pi nf = kv_b.$$

REFERENCES

1. J. R. Apel, Studies of Beam-Plasma Interactions in a Magnetic Field, APL/JHU TG-821, June 1966.
2. J. E. Simpson and D. A. Dunn, J.A.P. Vol. 37, 1966, p. 4201.
3. R. Z. Sagdeev and A. A. Galeev, "Lectures on the Non-Linear Theory of Plasma," Vol. 34, International Atomic Energy Agency, 1c/66/64, Trieste, 1966.

N67-33389

PLASMA FLOW IN A MAGNETIC FIELD

The flow of ionized gas (plasma) and its interaction with magnetic fields are basic areas of plasma research. Applications of knowledge gained include control of the plasma geometry, its thermodynamic properties, its flow velocity, and its purity. Economically useful thermonuclear fusion must await better understanding and control of these plasma properties.

This research program is specifically concerned with the behavior of a plasma in a magnetic transfer field. Two particular magnetic geometries are being evaluated: one is a solenoid field, the other is a multipole field that forms a magnetic channel. The problems associated with the introduction of the plasma into these guide fields and its behavior during an encounter with a magnetic constriction in a guide field are also being studied.

SUMMARY

New facilities for spectroscopic analysis of plasmas have been acquired and developed. A photographic survey of the visible region of the spectrum indicates the presence of carbon, oxygen, and possibly silicon impurities in the plasma. A special housing has been constructed that allows the photographic plate of the spectrograph to be replaced by several photoelectric detectors.

This permits the temporal development of several spectral intensities to be measured simultaneously for the same plasma. A special instrument has been designed and built that permits the intensity of light in 14 adjacent strips to be measured. This instrument will be used in conjunction with a monochromator to measure the width of broad spectral lines in order to infer the density of the plasma. This instrument can also be used to measure the size and intensity distribution across a plasma column. Figure 1 shows this 14-channel line splitter with its cover removed.

FUTURE PLANS

The temperature and density structure of the plasma puff and its evolution in the magnetic guide will be investigated in order to measure the efficiency of the transfer fields and to establish the nature of the loss mechanisms. Some additional improvement of the diagnostic facilities will be required for this study. An electronic data sampling and storage system for use with the 14-channel line splitter is being perfected in order to permit display of line profiles with a single oscilloscope.

Facilities for creating a magnetic constriction at the end of the guide field are being developed. We expect that a small reduction of the magnetic channel cross section will act like a nozzle for the plasma flow.
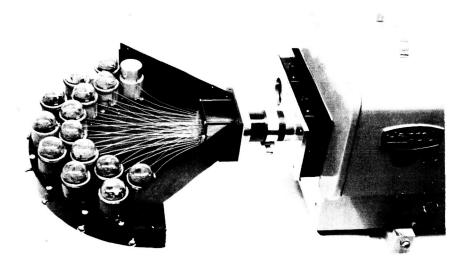
Fig. 1   Fourteen-Channel Line Splitter with Cover Removed. (90700)

A large reduction should reflect much of the plasma puff. The nature of the interaction occurring as the "head" of the plasma puff is folded back into the "tail" is of considerable interest and will be studied.

DISCUSSION

The presence of impurities in the plasma was not unexpected. The emphasis in this experiment is on plasma dynamics in a magnetic field. The carbon undoubtedly comes from diffusion pump vapors. The other impurities may enter the plasma when it is formed or may be produced during the decay of the plasma as it strikes the glass walls of the vacuum vessel At present only photographic measurements have been made, hence it is not possible to state when the impurities are released. We will use photoelectric measurements by means of the new detector housing to learn when the plasma strikes the walls.

FUNDAMENTAL RESEARCH V/2c
Plasma Dynamics X82CPR
Support: Task X/NOw 62-0604-c
T. O. Poehler
October 1966-March 1967

RESONANCE AND WAVE PHENOMENA IN SEMICONDUCTORS

The charge carriers and fixed ions in solids constitute a plasma similar to that which exists in ionized gases. Plasmas in semiconductors provide a means of measuring some of the basic parameters of these materials. Also, the existence of high-frequency instabilities and emission from these solids offers the possibility of interesting new emission sources. Experiments are being conducted in the excitation of instabilities in semiconductor plasmas, and the associated microwave radiation is being studied. Further work will be undertaken in microwave resonance and absorption measurements in these same materials, together with experiments on electron beam-wave interactions.

SUMMARY

Work has continued on the excitation of instabilities and microwave emission from high purity n-type indium antimonide. The study of the emission spectrum of n-type InSb mounted as inductive posts in waveguide has been extended to over 100 Gc/s. This emission spectrum, as shown in Fig. 1, did not decrease at high frequencies as sharply as reported by other authors (Refs. 1 and 2).

The emission spectrum has also been studied, using specimens mounted axially in cylindrical waveguide in both transverse and longitudinal magnetic fields. The radiation spectrum observed is similar to that for the specimen mounted as inductive posts. The emission from the axial configuration in a longitudinal magnetic field was unique in that part of the radiation occurred after the electric field pulse had concluded (Ref. 3), as shown in Fig. 2.

FUTURE PLANS

More detailed measurements in the higher frequency regime will be conducted, extending through the cyclotron and plasma frequencies of the specimens. Investigation of the temperature-dependence of these effects extending from 4° to 300°F will be attempted. Materials with different carrier concentrations and mobilities will be investigated over the entire range of frequencies and temperature.

DISCUSSION

Using techniques described in previous reports, the microwave emission spectrum of n-type InSb single crystals with an electron concentration of 1×10^{14}/cc and an electron mobility of 6.7×10^5 cm^2/volt-sec have been studied. The emission was excited by an electric field pulse from a specially constructed pulse
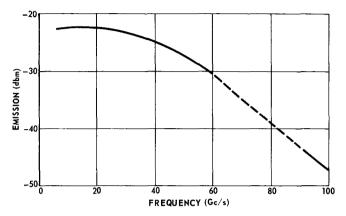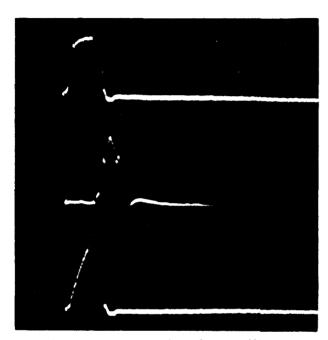
Fig. 1   Microwave Emission Spectrum of n–Type InSb; Electric Field Strength 200 Volts/cm; Transverse Magnetic Field 5.6 kG. (90701)

Fig. 2   Delayed Microwave Emission at 10.2 Gc/s; Upper Trace, Voltage Pulse (100 Volts/cm); Lower Trace, Microwave Signal (5 Volts/cm); and Time Scale, 0.5 μ sec/cm. (90702)

unit able to provide fast, high-current, high-voltage pulses (Ref. 4). The measurements have been performed on specimens mounted as inductive posts and also axially mounted in several waveguide configurations. The spectral response has been found to be similar for either mounting arrangement with somewhat higher output powers from the axial specimen, which can be attributed to a better coupling of microwave power out of the specimen. The spectral characteris-

Fig. 3   Microwave Emission during Current and Voltage Oscillations, Longitudinal Sample, Longitudinal Magnetic Field, 4 kG; Top Trace, Voltage Pulse (200 Volts/cm); Center Trace, Microwave Signal (50 Volts/cm); Bottom Trace, Current Pulse (20 Amps/cm; Time Scale, 1 μsec/cm. (90703)

tics were much more uniform than those reported by Larrabee and Suzuki, who saw a 1/f-type dependence. This difference can be explained by a more uniform detection sensitivity in the several superheterodyne systems used in the work reported here.

While the emission spectrum observed from the axial configuration in a longitudinal magnetic field was similar to that in a transverse field, it showed a different behavior in the time domain. The emission observed for electric field pulses just above the threshold value occurred with a time delay after the field pulse was applied. In all previous experiments in this laboratory and in those reported elsewhere, emission was observed to be coincident with the electric field pulse. At higher values of electric field, emission coincident with the electric field pulse was observed to increase in magnitude. At fields of 300 volts/cm, emission was observed for time periods considerably greater than the electric field pulse duration.

Large oscillations were observed in the current and voltage pulses at high field strengths when axial samples were in large magnetic fields. These oscillations reached an appreciable portion of the total field pulse amplitudes, as shown in Fig. 3. The emission observed during such oscillations increased by 10 to 20 db over that observed when the oscillations were not present.

REFERENCES

1. R. D. Larrabee and W. A. Hicenbothem, Proc. of Symp. of Plasma Effects in Solids, France 1964, Academic Press, pp. 181-187.
2. K. Suzuki, J. Appl. Phys. (Japan), Vol. 4, January 1965, pp. 42-52.
3. T. O. Poehler, J. R. Apel, and A. K. Hockberg, Appl. Phys. Ltrs., 1 May 1967.
4. T. W. Pearce, A. K. Hochberg, and T. O. Poehler, Rev. Sci. Inst. (to be published).

DOD RESEARCH PROJECTS X/2
Phased Array Antenna System QO8MRT
Support: ARPA
J. Frank
January–March 1967

PHASED-ARRAY ANTENNA SYSTEM

The Advanced Research Projects Agency (ARPA) had asked APL to design, fabricate, and test a C-band array of eight subarrays. The subarrays were built and tested and are being used to evaluate antenna parameters. Each subarray consists of a 1:48 reactive power divider, 48 ferrite phase shifters, and a radiating structure. The subarrays are designed to be assembled in several configurations, and may therefore be used to measure the effects of mutual coupling in both of the principal planes of scan. These mutual coupling effects result in increased reflections as the array is scanned from boresight. A matching surface, designed at APL, provides some compensation for these reflections.

SUMMARY

Extensive measurements were taken, with the subarrays arranged in three different geometries (Fig. 1). Some of the more interesting results are summarized below:

1. The gain of a uniformly illuminated array of eight subarrays was measured at boresight and found to be 30.1 db. This compares with a maximum theoretical gain ($4\pi A/\lambda^2$) of 31.4 db for a lossless antenna. The loss of 1.3 db indicates an overall efficiency of 74 percent at boresight.

2. The VSWR of a subarray immersed in an array of radiating subarrays was measured at scan angles up to 60° for the three-array configurations. The peak value of VSWR measured was 2.1. Correcting for losses in the subarray, this value corresponds to a VSWR of 2.6. Under most conditions of operation, the VSWR was significantly less.

3. The maximum absolute pointing error of the array was measured to be 1/50 beamwidth ($\approx$ 1 milliradian). The rms pointing error was 1/100 beamwidth. Figure 2 shows the absolute beam-pointing error as the array is scanned. The pointing errors were too small to permit an accounting for the source of the errors.

4. A large number of antenna patterns were taken. These patterns indicate good predictable performance in all modes of operation. No evidence of "lost beams" (a surface wave phenomenon) was ever encountered. Figure 3 shows the near-theoretical boresight pattern for subarrays aligned in the H-plane, with the sin x/x theoretical envelope superimposed.

The array is presently being used to investigate the effects of different phase-computation techniques to suppress grating lobes. These lobes are a consequence of the digital nature of the phase shifter. Breaking up the periodic phasing across the array by only a small amount has resulted in a marked improvement in grating lobe level at the expense of a slight increase in rms sidelobe level.
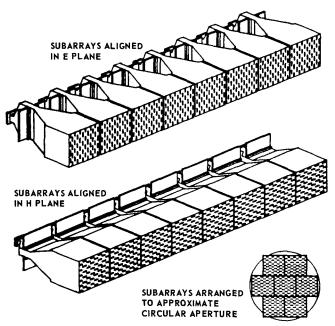
Fig. 1   Array Configurations. (90647)
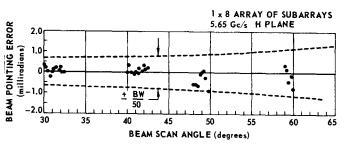
Fig. 2   Absolute Pointing Accuracy versus Beam Scan Angle. (90648)

BACKGROUND

A 48-element C-band subarray, built and tested at APL, consists of a reactive power divider in the form of four parallel E-plane lens-corrected horns, each with 12 ferrite phase shifters matched at the aperture. In this way an approximate constant amplitude distribution is obtained. The ferrite phase shifters are of the latching digital type, designed to operate with a low saturation current provided by inexpensive

THE JOHNS HOPKINS UNIVERSITY • APPLIED PHYSICS LABORATORY

Fig. 3 Boresight Pattern Compared with Theoretical $\frac{\sin x}{x}$ Envelope. (90649)

transistor drivers. Matching on boresight has been achieved with a thin dielectric sheet, which compensates for some of the mismatches that occur on scanning. High aperture efficiency was obtained.

DOCUMENT CONTROL DATA – R&D

(Security classification of title, body of abstract and indexing annotation must be entered when the overall report is classified)

1. ORIGINATING ACTIVITY *(Corporate author)*	2a. REPORT SECURITY CLASSIFICATION
The Johns Hopkins University, Applied Physics Laboratory 8621 Georgia Avenue Silver Spring, Maryland	UNCLASSIFIED
	2b. GROUP

3. REPORT TITLE

Research and Development Programs

4. DESCRIPTIVE NOTES *(Type of report and inclusive dates)*

Quarterly Progress Report for January 1 through March 31, 1967

5. AUTHOR(S) *(Last name, first name, initial)*

Multiple Authorship (see individual sections)

6. REPORT DATE	7a. TOTAL NO. OF PAGES	7b. NO. OF REFS
January - March 1967	62	77

8a. CONTRACT OR GRANT NO.	9a. ORIGINATOR'S REPORT NUMBER(S)
NOw 62-0604-c	
b. PROJECT NO.	U-RQR/67-1
c.	9b. OTHER REPORT NO(S) *(Any other numbers that may be assigned this report)*
d.	

10. AVAILABILITY/LIMITATION NOTICES

Each transmittal of this document outside the agencies of the U.S. Government must have prior approval of Naval Ordnance Systems Command.

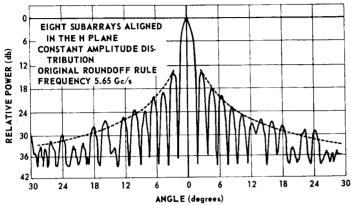| 11. SUPPLEMENTARY NOTES	12. SPONSORING MILITARY ACTIVITY
	Naval Air and Ordnance Systems Commands, ARPA, National Aeronautics and Space Administration, and Air Force Cambridge Research Laboratory

13. ABSTRACT

A record of the activities of the Applied Physics Laboratory in the field of Research and Development is issued in two volumes. The first volume contains a record of the classified work (C-RQR); the second contains a record of the unclassified work (U-RQR). In this volume the results are reported on work in the following categories: thin-film technology development; microelectronic packaging; semiconductor diffusion technology; maser research; radar scattering from the sea; simulation experiments for jet interaction; a study to determine the practicability of designing a volume-limited missile configuration that has good maneuverability at high altitude; radome thermal stress investigations; vibration studies; transpiration cooling investigations; studies of the effects of high temperatures on structures and materials; mechanical property tests on Al_2O_3 and SiO_2; thermal stresses in sandwich shells; hypersonic leading edge structures and materials; mixing devices for delaying wind-tunnel flow separation; a spherical focused blast device; thermal explosion analyses; explosive projection of metal; adaptive stabilization computer; a wideband-array antenna system; a direct synthesis of an optimal linear filter from conditional probability concepts; trajectory optimization by the steepest ascent method; analysis of supersonic combustion; analysis of turbulent mixing; two-dimensional mixing studies; studies of clear-air turbulence; beam plasma interactions; plasma flow in a magnetic field; resonance and wave phenomena in semiconductors; and a phased-array antenna system (U).

DD FORM 1473 (1 JAN 64)

14.	KEY WORDS	J-RQR

Adaptive computing
Adaptive stabilization computer
Aerodynamic heating, leading edges
Aerodynamics, supersonic
Advanced warhead research
Airframe structures
Alumina sandwich construction
Antenna, phased-array
Beam-plasma interactions
Boundary layer phenomena
Clear air turbulence
Columbium alloy
Combustion, ramjet
Digital computer simulation
End-game simulation
Explosive metal projection
Gas transpiration cooling
Guided missile aerodynamics
Jets, two-dimensional interaction
Leading edges, thermal protection
Maser research
Metal alloys, creep
Microelectronic packaging
Microelectronics
Michigan, University of
Microwave reflection, sea
Optimal filter
Plasma dynamics
Plasma flow, magnetic field
Radar antennas
Radar propagation studies
Radar turbulence studies
Radome limitations
Radomes, thermal stress
Ramjet combustion
Semiconductor plasmas
Ship-motion prediction
Steepest ascent method
Structural elastic studies
Supersonic combustion
Tantalum disilicide
Thermal expansion
Thermal explosion analysis
Thermal stress in radomes
Thermal studies
Thin-film technology
Trajectory optimization
Transpiration cooling
Turbulent mixing
Two-dimensional mixing
Warheads
Wind-tunnel separation phenomena
Zero-field maser

INITIAL DISTRIBUTION EXTERNAL TO THE APPLIED PHYSICS LABORATORY*

The work reported in U-RQR/67-1 was done under Contract NOw 62-0604-c with the Department of the Navy.

APL Task	Supporting Agency	APL Task	Supporting Agency	APL Task	Supporting Agency
A11	NAVORDSYSCOM (0625)	A33	NAVORDSYSCOM(035) NAVAIRSYSCOM (320)	WO1	Air Force Cambridge Research Lab NASA
A12	NAVAIRSYSCOM (5202) TASK X/NOw 62-0604-c	A37	NAVAIRSYSCOM (320)		
		A42	NAVORDSYSCOM (0622)	X82	TASK X/NOw 62-0604-c
A13	NAVORDSYSCOM (034)	A62	NAVORDSYSCOM (0621)	Y1	TASK Y/NOw 62-0604-c
A14	NAVAIRSYSCOM (310)	A63	NAVORDSYSCOM (0621)	Z11	NASA Hq. (RAP)
A31	NAVORDSYSCOM (033) (035)	Q08	ARPA		

ORGANIZATION	LOCATION	ATTENTION	No. of Copies
DEPARTMENT OF DEFENSE			
Dir., Defense Research/Engineering	Washington, D. C. 20301	Technical Library	1
Dir., WSEG	Washington, D. C. 20301		1
Dir., ARPA	Washington, D. C. 20301		1
		Capt. Julio Torres	1
DDC	Alexandria, Va. 22314		20
DCASO, AL	Daingerfield, Texas		1
Department of the Navy			
Department Offices			
CNO	Washington, D. C. 20350	OP-07T15	1
CNM	Washington, D. C.	PM-301	3
		PM-321	1
NAVORDSYSCOM	Washington, D. C.	00	
		0024	
		03	
		0321	1
		033	
		034	1
		035	1
		06F	3
		062	1
		0621	1
		0622	1
		0624	1
		0625	1
		08	1
		083	1
		09	1
		09132	2
		093	1
Special Projects Office	Washington, D. C.	SP-001	1
		SP-20	1
		SP-24	1
		SP-27	1
NAVAIRSYSCOM		00	1
		03	1

Requests for copies of this report from DoD activities and contractors should be directed to DDC, Cameron Station, Alexandria, Virginia 22314 using DDC Form 1 and, if necessary, DDC Form 55.

*Initial distribution of this document within the Applied Physics Laboratory has been made in accordance with a list on file in the APL Technical Reports Group.

INITIAL DISTRIBUTION EXTERNAL TO THE APPLIED PHYSICS LABORATORY

U-RQR/67-1

Page 2

ORGANIZATION	LOCATION	ATTENTION	No. of Copies
Department of the Navy (Cont'd)			
NAVAIRSYSCOM (Cont'd)	Washington, D. C.	03B	1
		03C	1
		03D	1
		320	1
		5108	1
		520A	1
		5202	1
		5203	1
		531	1
		535	1
		604	2
NavPlantRepO	Silver Spring, Md.		1
NavPlantRepO	Mishawaka, Ind.		1
NavPlantRepO	Minneapolis, Minn.		1
Laboratories			
NOL	White Oak, Md. 20910	Library	1
NRL	Washington, D. C. 20390	2027	1
		463	1
NWL	Dahlgren, Va. 22448	Library	1
NEL	San Diego, Cal. 92152	Library	1
NOL	Corona, Cal. 91720	Doc. Library	3
Facilities			
NOTS	China Lake, Cal. 93556	Tech. Library 753	3
NSMSES	Port Hueneme, Cal. 93041		5
NPP	Indian Head, Md. 20640	TEL	1
NEODF	Indian Head, Md. 20640		1
DTMB	Washington, D. C.	Aerodyn. Lab. Lib.	1
Schools			
U. S. Naval Academy	Annapolis, Md. 21402	Weapons Dept.	1
Naval Postgraduate Sch.	Monterey, Cal. 93940		1
Naval Guided Missile School	Dam Neck, Va. 23461	Library	1
Pac. Flt. Training Command	San Diego, Cal. 92132	MISTRAUPAC	1
Mare Is. Nav. Schs. Command	Vallejo, Cal. 94592	Guided Missile Sch.	1
Centers			
NMC	Pt. Mugu, Calif.	Tech. Library (No. 3??)	1
Department of the Air Force			
Chief of Staff	Washington, D. C. 20330	AFRST-AS	1
Deputy Chief of Staff, R&D	Washington, D. C.	AFRST	1
AFSC/STLO	Washington, D. C. 20331	RTD (RTSAW)	1
Headquarters, RTD (AFSC)	Bolling AFB	RTD (RTTP)	1
Laboratories			
Aero Propulsion Laboratory	WPAFB/Dayton, O.	APRC	1
AF Cambridge Research Laboratory	Hanscom Field, Bedford, Mass.	01731	1
Avionics Laboratory	WPAFB, Dayton, O.	AVPT	1
Air Force Armament Laboratory	Eglin AFB, Valparaiso, Fla.	(PGBPS-4)	1
AFWL (WLIL)	Kirtland AFB, N. M.		1
Air Force Rocket & Prop.	Edwards AFB, Cal.	RTMMM	1
Project Rand	Santa Monica, Cal.		1

ORGANIZATION	LOCATION	ATTENTION	No. of Copies
Department of the Air Force (Cont'd)			
Centers			
Aeronaut. Chart Info. Ctr.	St. Louis, Mo. 63118	ACOC	1
Commands			
Air Force Systems Command	Andrews AFB, Washington, D. C.	SCTR	1
Foreign Technology Division	WPAFB, Dayton, O.	TD-Bla Library	1
Systems Engineering Group (RTD)	WPAFB, Dayton, O. 45433	SEPIR	1
Air Univ. Library	Maxwell AFB, Mont. Ala. 36112		1
Continental Air Defense Com.	Ent AFB, Colo. Spgs., Colo. 80912	Directorate of Syst. Dev.	1
Department of the Army			
Offices			
Assistant Secretary/R&D	Washington, D. C. 20310		1
Assist. Chief of Staff/Intell.	Washington, D. C. 20310	R & D Branch	1
Laboratories			
Harry Diamond Laboratory	Washington, D. C. 20438	AMXDO-TIB	1
Engineering R & D Labs.	Ft. Belvoir, Va. 22060	Tech. Docs. Ctr.	1
Electronics R & D Activity	WSMR, N. M. 88002	SELWS-W	1
Facilities			
Aberdeen Proving Ground	Aberdeen, Md. 21005	Library	1
Redstone Scientific Info. Ctr.	Huntsville, Ala. 35809	Chief, Docs. Section	5
Electronic Proving Ground	Ft. Huachuca, Ariz. 85613	Technical Library	1
Arsenals			
Picatinny Arsenal	Dover, N. J. 07801	Tech. Info. Agency	1
Rock Island Arsenal	Rock Island, Ill. 61201	SWERI-RDI, Doc. Sect.	1
Schools			
Army War College	Carlisle, Pa. 17013	Library	1
Agencies			
Materials Research Agency	Watertown, Mass. 02172	Tech. Info. Ctr.	1
Signal Air Def. Eng. Agency	Ft. Meade, Md. 20755		1
Armor Combat. Devel. Agency	Ft. Knox, Ky. 40121		1
Artill. Combat Devel. Agency	Ft. Sill, Okla. 73503		1
Air Defense Combat Dev. Agency	Ft. Bliss, Tex. 79916		1
U. S. GOVERNMENT AGENCIES			
Security Agencies			
Central Intell. Agency	Washington, D. C. 20505	OCR-Stand. Dist.	4
National Security Agency	Ft. Meade, Md. 20755	C3/TDL	1
National Aero. and Space Admin.			
Headquarters	Washington, D. C. 20546	M. J. Aucremanne	4
Office of Space Sciences	Washington, D. C. 20546	Res. Grants/Contracts	25

ORGANIZATION	LOCATION	ATTENTION	No. of Copies
U. S. GOVERNMENT AGENCIES (Cont'd)			
Atomic Energy Commission			
Headquarters Library	Washington, D. C. 20545		1
Tech. Inf. Extension	Oak Ridge, Tenn. 37830		1
Mgr. AEC Albuquerque Operations	Albuquerque, N. M. 87115		1
DASA Test Command/Sandia	Albuquerque, N. M. 87115	TCSB-T	1